MCCXXII

UNIVERSITÀ DEGLI STUDI DI PADOVA

Dipartimento di Fisica e Astronomia “Galileo Galilei”

Master Degree in Physics of Data

Final Dissertation

Structure-function relation in a stochastic whole-brain model at criticality

Thesis supervisor
Prof. Samir Suweis

Candidate
Giacomo Barzon

Academic Year 2020/2021

Abstract

Understanding the relation between brain architecture and function is one of the central issues in neuroscience nowadays. In the last few years, important efforts have been devoted to map the large-scale structure of the human cortex, the so-called "connectome". An example is the neuroanatomical connectivity matrix of the entire human brain obtained through MR diffusion tractography. Recent studies proposed a stochastic model built on top of this connectivity matrix that displays a phase-transition and is able to reproduce several aspects of brain functioning when tuned to its critical point. This master thesis is aimed to review recent results on this subject and to get a deeper insight into the model by studying the distribution of the avalanches, the dynamical range and to investigate how the use of simulated connectivity matrices affects the dynamics. Furthermore, a theoretical description of the dynamics is proposed by introducing a master equation in order to understand the nature of the phase transition and the role of stochasticity.

Contents

Introduction **1**

1 Network Neuroscience **5**
- 1.1 Structural Networks . . . 5
- 1.2 Functional Networks . . . 7
- 1.3 Structure-Function relationship . . . 10

2 Emergent patterns and Criticality in the Brain **13**
- 2.1 Neuronal avalanches . . . 14
- 2.2 Long-range temporal correlations . . . 17
- 2.3 Signatures of criticality in Resting State Networks . . . 18
- 2.4 Importance of being critical . . . 19
- 2.5 How to build a critical brain . . . 20

3 A stochastic whole-brain model of the human connectome **23**
- 3.1 HTC model . . . 24
  - 3.1.1 Dynamics and phase transition of the model . . . 25
  - 3.1.2 Numerical versus empirical results . . . 28
- 3.2 Homeostatic plasticity . . . 30
- 3.3 Avalanches . . . 32
  - 3.3.1 Causal avalanches . . . 34
- 3.4 New evidence of criticality . . . 36
  - 3.4.1 Fisher information . . . 36
  - 3.4.2 Dynamic range . . . 37

4 Structure-function relation in a stochastic whole-brain model at criticality **39**
- 4.1 Scaling of the critical point in the mean-field approximation . . . 39
  - 4.1.1 Adding random noise . . . 41
- 4.2 HTC model with synthetic connectomes: the effect of connectivity . . . 43
  - 4.2.1 Dynamical regimes . . . 43
  - 4.2.2 Effect of homeostatic plasticity . . . 44
  - 4.2.3 Constant weights . . . 48
  - 4.2.4 Finite size scaling . . . 49

5 Conclusions and future perspectives **55**

A A Hint of Network theory **57**

A.1 Adjacency matrix . . . 57
A.2 Degree and connectance . . . 58
A.3 Components . . . 58
A.4 Measures and metrics . . . 59
A.4.1 Centrality and hubs . . . 59
A.4.2 Clustering . . . 60
A.4.3 Assortativity . . . 60
A.4.4 Community structure . . . 61
A.5 Models of network structure . . . 61
A.5.1 Random graphs . . . 61
A.5.2 Small-world graphs . . . 62
A.5.3 Scale-free graphs . . . 63

B Mean-field approximation 65
B.1 Derivation of the master equation . . . 65
B.2 Thermodynamic limit . . . 67
B.2.1 Super-critical phase . . . 68
B.2.2 Sub-critical phase . . . 69
B.2.3 Diagram of equilibria . . . 70

Bibliography 73

Introduction

Today's era is characterized by the rise of big data. This term was coined to describe the exponential increase and availability of data far beyond the human scale. In the early 2000s, industry analyst Doug Laney [1] articulated the now-mainstream definition of big data as being characterize by the three Vs: the extreme volume, the velocity at which the data must be processed, and the wide variety of data types. The Big Data analytics is indeed a revolution in the industry because it leads to cost savings and time reductions and has benefited society in many ways, making our lives healthier, safer, greener and more efficient. The scientific world has certainly not been immune from this radical change, thanks to the technological developments that have enabled the design of increasingly precise and in-depth experiments. Just think of the petabytes of data produced by particle collisions every year at LHC.

In recent years, big data has arrived in the neuroscientific scene. New empirical methodologies provide an increasing amount of data, spanning an astonishing range of scale of both time and space. These range from the recordings of single cells thanks to patch-clamp [2], to neural tissue analysis with optogenetics [3] and calcium imaging [2] to the dynamic evolution of whole-brain activity with fMRI [4]. However, these large data reservoirs are just a worthless raw material without the right tools and techniques to manipulate them. As data sets grow and become more complex, they become more difficult to analyze and to extract some useful evidence. Statistics and machine learning help to automatize this process by projecting the high dimensional space of data features to a lower dimensional and hopefully more tractable description, sometimes with unsupervised techniques. The design of this statistical analysis is a critical factor in insuring that the dataset is usable by other researchers. In fact, it is argued that there needs to be a cultural transition from many isolated studies to a common, distributed effort among all laboratories to boost the research in such an important, but still largely unexplored area [5]. A possible remedy could be the standardization of dataset collected with a single methodology and the integration of cross-technical data from multiple domains of brain and behaviour and across species. Some examples of this research infrastructures are the Brain Initiative [6], the Human Brain Project [7] and the Human Connectome project [8].

A relevant effort of this technological challenge is devoted to map the intricate labyrinth of interconnections in the human brain. These connections can be studied at different scales, from synaptic links between couples of neurons to axonal pathways in microcircuits to fiber bundles between larger systems like cortical areas, delivering a comprehensive description of the structural connectivity, defined as *human connectome*. However, the brain is also characterize by the collective dynamics of neurons that leads to a macroscopic neurophysiological activity and governs all the functioning of our body: vital tasks, movements, emotions, thoughts. This functional connectivity even appears in spatially

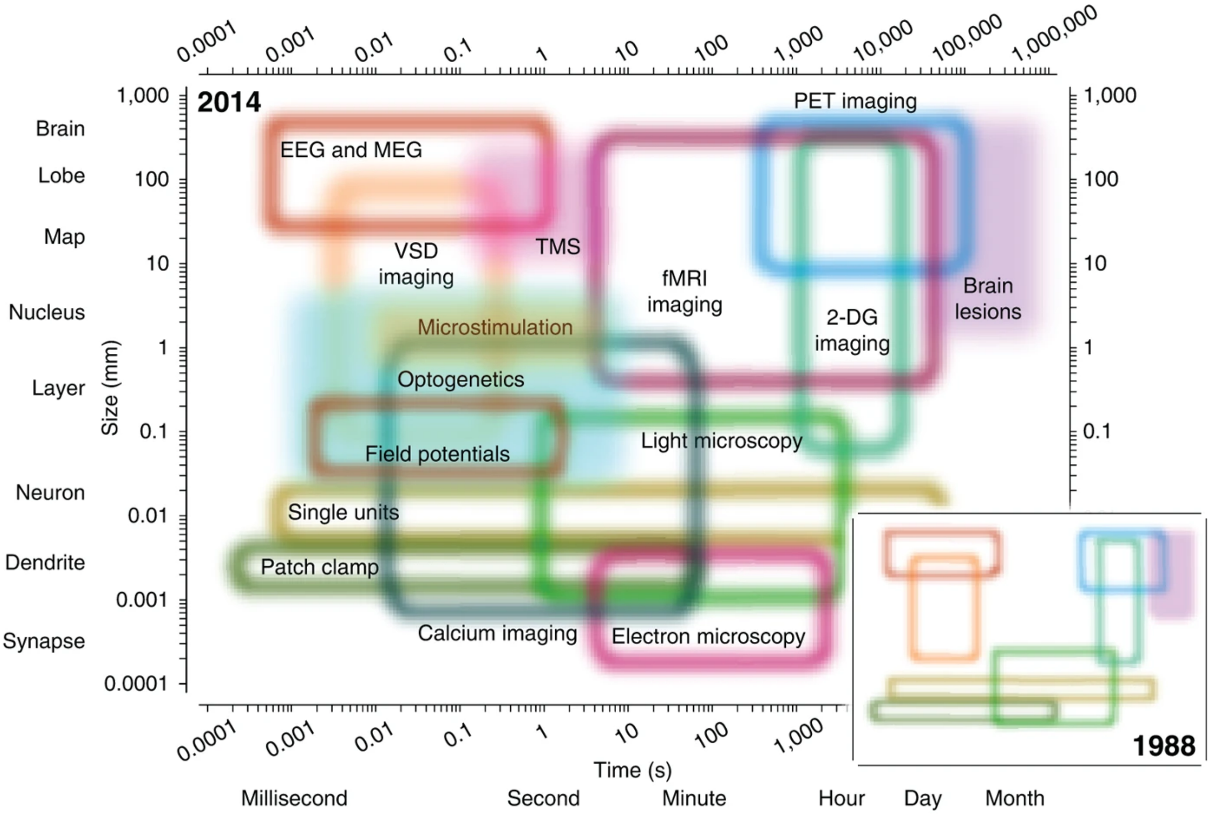

Figure 1: The spatiotemporal domain of neuroscience and of the main methods available for the study of the nervous system in 2014. Each colored region represents the useful domain of spatial and temporal resolution for one method available for the study of the brain. *Open regions* represent measurement techniques; *filled regions*, perturbation techniques. *Inset*, a cartoon rendition of the methods available in 1988, notable for the large gaps where no useful method existed. From [5].

segregated areas and can be statistically extrapolated by analyzing the correlation between different regions or through more sophisticated measures of nonlinear coupling or causal dependence.

Describing these types of networks with the language of graph theory and network science is straightforward. Moreover, brain networks meet the definition of a complex systems as an ensemble with collective properties that arise from the interactions among their constituent units and are not directly attributable to the dynamic governing the single component. The increasing interest in this area of research has led to a fundamental insight: different complex systems share certain common properties despite profound differences in the details of constitutive elements. Brain networks, both at the cellular and whole-brain scale, shares some topological feature of these complex networks that are not merely aesthetically, but are guided by some efficiency principles [9]. For instance, small-world properties have been demonstrated in models of the nervous system of the nematode *Caenorhabditis elegans* [10], in vertebrate brain-steam [11,12] and in the human connectome [13]. Also many patterns of functional connections are consistent with a small-world graph, implying a short network diameter, and it is associated with a high global efficiency of information transfer [9]. These networks exhibit also a high clustering coefficient, which is correlated with robustness to random failures of nodes or edges. Other analysis identified a modular structure interconnected by hub regions with high betweeness centrality. The presence of specialized hubs is further supported by the scale-free degree distribution [9].

Clearly, a deviation from this common topological organization could be a symptom of the disruption or abnormal functioning of spatially distributed brain regions that would ordinarily constitute a large-scale network, as it has already been demonstrated in many neurological and psychiatric disorders, like schizophrenia [14] or Alzheimer's disease [15]. Thanks to further developments in the field of network theory, in the future this geometric properties could be hopefully used as a diagnostic marker to assess brain health or to identify diseases at an early stage.

Another analogy with the world of complex system is the concept of criticality. The *critical brain hypothesis* states that the brain may be poised near a critical point of a second-order transition between an ordered, silent phase and a chaotic, overactive phase [16]. Indeed the collective neuronal dynamic resembles the scenario of critical phenomena, which have already been documented in many natural processes like gene networks [17, 18], ecological dynamics [19], and flock formation [20]. In all these phenomena, such different from each other, there is the presence of long-range spatiotemporal correlated patterns which emerges in a wide variety of states [21]. The first, and probably the most famous, convincing evidence of critical dynamics in brain cells was reported by Beggs and Plentz [22]. They identified a new mode of spontaneous activity in cortical networks: the neuronal avalanches. These cascades of synchronized bursting activity that spread and distribute over the brain have a scale-free distribution well described by an inverse power-law, both in spatial and temporal domain, with exponents that agrees with the theoretical prediction for a critical branching process. Also, many other experimental and theoretical studies have linked criticality with optimal computational properties [23, 24] and flexibility to access the largest number of metastable states or, in other words, the largest repertoire of behaviours [25, 26]. From an evolutionary perspective, these benefits may have prompted the brain to self-organize at the edge of a critical phase transition which is not guided by any external inputs [16, 19]. Nevertheless, this hypothesis has remained controversial and there is an open debate going on [27]. For instance, a relevant counter-example is that many non-critical processes have also proven to be responsible for scale-free neural avalanches [28].

How this rich patterns of coordinated electrochemical activities is related to our anatomical connectivity is still largely unexplored. The structural substrate acts as a constraint on which dynamical interactions occur in the brain and partly determine the functionality of each individual node. In many studies carried out over long time periods of measurements, functional networks are robust and structural changes are relieved thanks to homeostatic mechanisms. In fact most of the biological modifications to the neural tissue are associated with aging, disease progression or experience-dependent plasticity. On the other hand, at fast timescales functional networks undergo spontaneous fluctuations and are highly responsive to external stimuli: how that is supported by the physical connectivity is part of the unresolved *structure-function relationship* problem [29, 30].

Computational models play a crucial and complementary role in this twisted road. Typically, such models are built on top of empirically derived brain structural networks that specify the wiring between neuronal units. The dynamics is instead described by differential equations derived from biophysical mechanisms regulating the units activity. In fact, the mathematical description of the origin of spikes in a single neuron is precise and predictive. During the 1950s from the recordings of the electrical activity in the squid giant axon, Nobel-prize winners Hodgkin and Huxley unveiled that the gated ion channels in neuronal membrane which generate fast depolarizing and slow hyperpolarizing currents are responsible for the initiation and propagation of action potentials [31]. Because of the considerable number of parameters, the *Hogking-Huxley* model cannot be generalized to large populations of neurons, so the common approach is to introduce a rough approximation in the equations governing the dynamics. Probably the most widely used class of models is the *integrate-and-fire neuron* model [32]. It describes the membrane potential of a neuron in terms of the injected current that it receives. An action potential is generated by the integrated effect of synaptic inputs when the membrane potential reaches a threshold, regardless of membrane conductances and ion channels driving the actual changes in membrane potential. "*The integrate-and-fire neuron model has become established as a canonical model for the description of spiking neurons because it is capable of being analyzed mathematically while at the same time being sufficiently complex to capture many of the essential features of neural processing*" [32]. In presence of strong coherence inside a population of cells in a small patch of cortex, it can be assumed that the dynamics of the entire ensemble resembles the conductance-based model of each single neuron. With this dimensionality reduction the description can be further generalized to interactions among multiple local populations, such as excitatory and inhibitory units, as done in the family of *neural mass models*. The scale of the whole-brain dynamics is then reached by coupling an ensamble on these *neural mass models* into circuits and macroscopic networks whose structure is obtained from empirical connectivity data [33].

Although many of these models were able to partly reproduce experimental findings at the macroscopic scale, a broadly accepted mathematical theory for the collective activity of neuronal populations is still missing. Moreover, the research in this field has largely proceeded without formal biophysical models of the underlying large-scale neuronal activity, leading to more descriptive than explanatory theoretical models. The concerted effort of new approaches for big data analysis with advancements in network theory and computational modelling could deliver fundamentally new insights and knowledge in "*making sense of brain network data*" [34].

The purpose of this thesis is to present the state-of-the-arts techniques for extrapolating structural and functional networks from brain imaging data and discuss their main properties from a network theory perspective (Chapter 1). Next we review the experimental and theoretical evidence that supports the critical brain hypothesis (Chapter 2). In this context, an interactive-particle stochastic model built on top of an empirically derived neuroanatomical connectivity matrix was proposed few years ago [35]. This model is able to reproduce some experimental findings from functional magnetic resonance imaging when tuned at criticality. Our work sought to expand the study of this model by investigating in more detail other evidence of criticality and the possible existence of avalanches (Chapter 3). Then we explore the influence of topology on dynamics (Chapter 4). To do that, we perform some simulations over graphs generated from classical ensembles of network structure, like random and small-world graphs. Finally, we attempt to produce a theoretical description of the model starting from a mean-field master equation.

Chapter 1

Network Neuroscience

Biological and cognitive functionalities in the human brain are the manifestation of neural interactions at multiple levels of organization. The modeling of the brain interactions lends itself so well to be described with the language of network theory. A network is a set of items, usually referred as vertices or nodes, with connections between them, called edges [36] (see also Appendix A). Recent developments in neuroscience, that have led to sophisticated empirical methods for mapping and recording neurobiological data, intersect with theoretical and computational advances in data analysis and brain modelling. The convergence of such improvements have given birth to the field of *network neuroscience* [37].

How to define nodes and edges is a crucial issue and changes depending on the spatial scale and the type of connections between units under analysis. Nodes may denote neural elements, like neurons or brain regions, that are linked by edges representing physical connections, like synapses or axonal projections, usually grouped under the name of white matter. This family of networks describing the anatomical configuration of the encephalon from inter-neuronal to inter-regional connectivity is gathered under the name of *structural networks*. However, anatomical connectivity is merely an inanimate backbone on top of which neurophysiological dynamics occurs. Indeed a network may also group the set of even spatially distinct brain areas that contribute to the operation of a particular task or control a specific sensory-motor system. In such types of networks the strength of the links is a measure of the correlation and the co-activation between a particular pair of regions, making up a *functional network* [9]. To what extent the functional operating of the brain is constrained by the anatomical configuration is still largely unknown.

In this chapter we scratch the surface of the very wide world of structural and functional brain networks, we briefly review their main topological properties within network theory framework and the experimental techniques to obtain them. Moreover, we discuss commonalities and differences between the two techniques, entering in the unresolved *structure-function relationship*.

1.1 Structural Networks

Tracing the complete neuronal architecture of living beings has been one of the most intriguing issue for many scientific branches and a long-standing technological challenges. The first complete nervous system to be mapped was that of the nematode *C. elegans*

(Fig.1.1). In fact, thanks to electron microscopy recordings, researchers were able to deduced the complete connection matrix between its set of 302 neurons from reconstructions of serial brain sections [10]. Until present, it is still the only nervous system to have been comprehensively mapped at a cellular level, because in more evolved organism the number of neurons and axonal pathways increases exponentially making it very hard to obtain a complete description, if not nearly impossible.

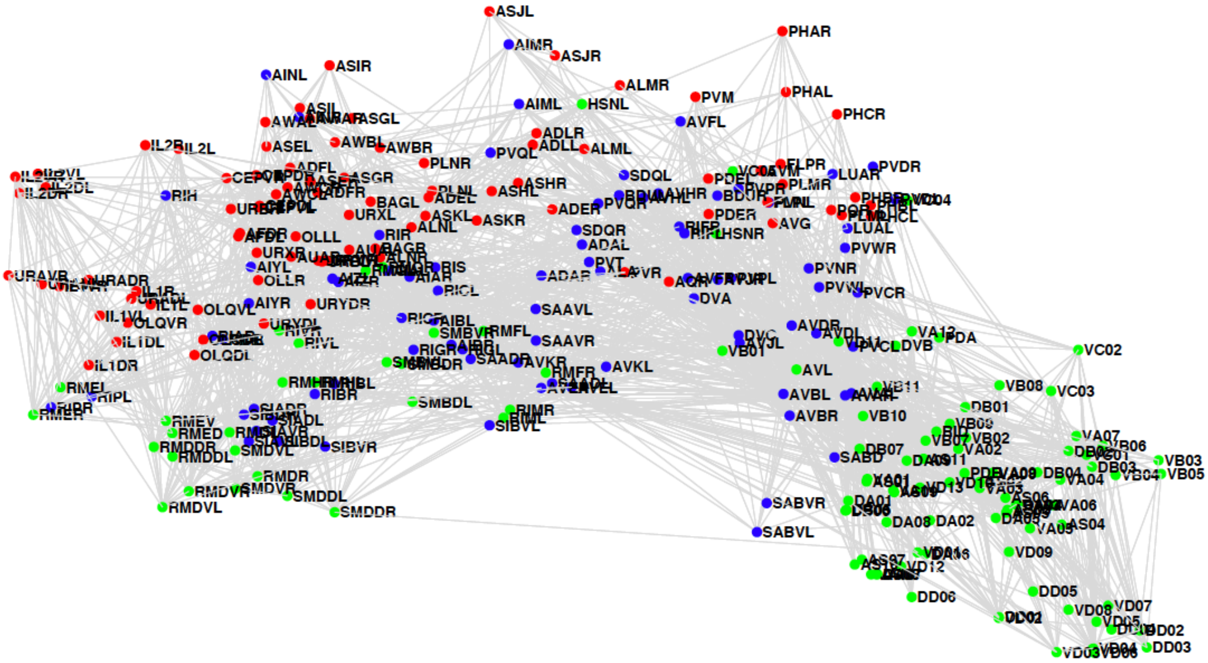

Figure 1.1: The C. elegans wiring diagram. *Red*, sensory neurons; *blue*, interneurons; *green*, motorneurons. *Gray links*, chemical and electrical synapses. From [38].

Although the *C. elegans* is one of the simplest organism with a nervous system, it has provided interesting insights regarding organizational principles of the neural substrate. Indeed it shows high levels of local clustering, combined with short paths that globally link all nodes of the network, typical of a *small-world* graph (see Appendix A.5.2). This means that all neurons are linked through relatively few intermediate steps, despite the fact that most nodes maintain only a few direct connections, mostly within a clique of neighbours. Such properties favour a rapid exchange of information through electrical signals between neurons, thus leading to better performance of the nervous system. In other words, these findings indicate that even the simplest nervous system has evolved to a non-random architecture to achieve a more efficient neural processing [9].

Histological dissection and axonal tracing have been used to map cerebral white matter connections, obtaining models of cortical sensory-motor system in vertebrates, like the macaque visual cortex [11] and the cat thalamocortical system [12]. Network analysis of such data reveals also in this cases small-world properties.

Human brain has around one hundred billion neurons and almost seven hundred trillion synaptic connections. Building a complete human connectome is thus inconceivable with existing technology. Nevertheless, scientists still manage to get a measure of global brain connectivity at mesoscopic spatial scale. With *diffusion tensor imaging* (DTI) and *tractography* methods, it is possible to track the diffusion of water in neural tissue to have an estimate of the real white matter axonal trajectories and a map of the internal structures of the brain [39]. DTI has difficulties in detecting crossing fiber bundles, which are overcome by reconstructing multiple diffusion directions in each voxel thanks to *diffusion spectrum imaging* (DSI), allowing a more accurate mapping of axonal trajectories [40].

In [13] a famous high resolution cortical connectome was derived from DSI analysis of 5 healthy participants. Connectivity matrices were obtained both at high spatial resolution, as well as for regional connectivity (Fig.1.2). Cortical volume from MRI data was first parcellated with segmentation algorithms into 66 anatomical sub-regions, which in turn were partitioned into 998 regions of interest (ROI) with an average size of $1.5cm^2$. Each entry in the overall symmetric weighted connectivity matrix (Fig.1.3-a) represents the total number of axonal pathways between a pair of ROIs, normalized by their cortical surface. In the regional connectivity matrix, the weights are averaged over fiber densities for all pairs of ROIs belonging to the same region.

Having almost 1000 units in the derived network allowed to perform an extensive graph analysis. Distributions of node degree and node strength were found exponential rather than scale-free, with most of the connections linking nodes belonging to the same anatomical sub-region or to functionally related areas [13]. Moreover, the study revealed highly clustered structural modules interconnected by specialized and highly central hubs, ensuring a short overall path lengths across the network. In addition, clusters identified by network analysis map on to known functional subdivisions of the cortex [9]. Even if only a small percentage of links connects the two hemispheres, *”the high degree of inter-hemispheric coupling further suggests that it* (the brain) *acts as a single integrated system from which processes in both cortical hemispheres are coordinated”* [13].

1.2 Functional Networks

The brain is continuously active and generates electrical signals that communicate between the various regions to coordinate the vital functions of every human being. Neuronal activity can be directly measured with electrophysiological methods, like *magnetoencephalography* (MEG), *electroencephalogram* (EEG), and *multi-electrode array* (MEA), that record electrical or magnetic potentials on the surface of sensors or electrodes, resulting in a 2-D projection of the overall neural dynamics. Despite a good temporal resolution, these methods have a poor spatial resolution, on the order of millimeters or centimeters.

To obtain activity in anatomically localized regions of cortical volume, *functional MRI* (fMRI) measures *blood oxygen level dependent* (BOLD) signals that is found to be related to neuronal activity [9]. Indeed, *”when neuronal activity increases there is an increased demand for oxygen and the local response is an increase in blood flow to regions of increased neural activity. Oxygen is delivered to neurons by haemoglobin in capillary red blood cells. Haemoglobin is diamagnetic when oxygenated but paramagnetic when deoxygenated. This difference in magnetic properties leads to small differences in the MR signal of blood depending on the degree of oxygenation. Since blood oxygenation varies according to the levels of neural activity, these differences can be used to detect brain activity”* [41].

fMRI signals are very susceptible to many sources of fluctuation, like the heartbeat, breathing or head motion artifacts, and to interference with close brain areas, therefore it requires a profound statistical analysis [42, 43] Typically, after detrending and regressing out the experimental time-series, the ”real” time course of brain regional dynamics is

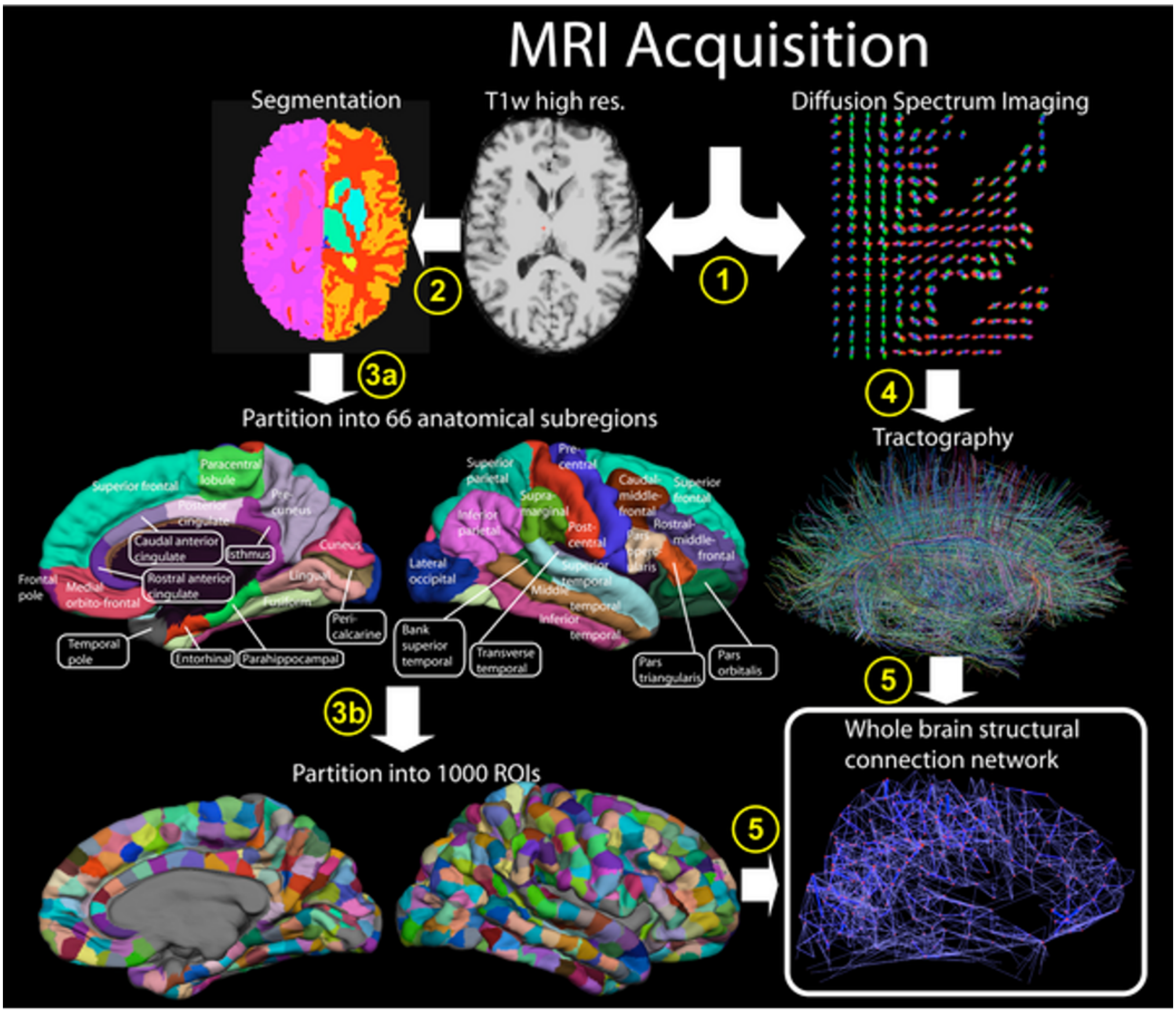

Figure 1.2: Pipeline for obtaining a structural connectivity matrix of the human brain. (1) High-resolution T1 weighted and diffusion spectrum MRI (DSI) is acquired. (2) White and gray matter segmentation is performed from the T1-weighted image. (3a) Cortical volume is parcellated into 66 cortical regions with clear anatomical landmarks, (3b) subdivided into 998 small regions of interest (ROIs). (4) Whole brain tractography is performed providing an estimate of axonal trajectories across the entire white matter. (5) ROIs identified in step (3b) are combined with result of step (4) in order to compute the connection weight between each pair of ROIs. From [13].

inferred thanks to dimensionality reduction or clustering algorithms. *Independent component analysis* (ICA) is perhaps the most commonly used. Given some space-time measurement, ICA searches for statistically independent sources that give rise to the observed signals. In this case, each source reflects the time course of the neuronal dynamics from a specific and spatially located region of the human brain [44].

Functional connectivity is defined as the *"temporal dependency of neuronal activation patterns of anatomically separated brain regions"* [45]. The weights of the functional connectivity matrix are usually computed as a cross-correlation map between the resulting pairs of time-series from ICA, that reflects the level of co-activation and functional communication between regions. fMRI measurements can be performed in task-related experiments or in patient at rest. Interestingly, studies on resting-state fMRI BOLD time-series reveal high correlations between the spontaneous neuronal dynamics of brain areas,

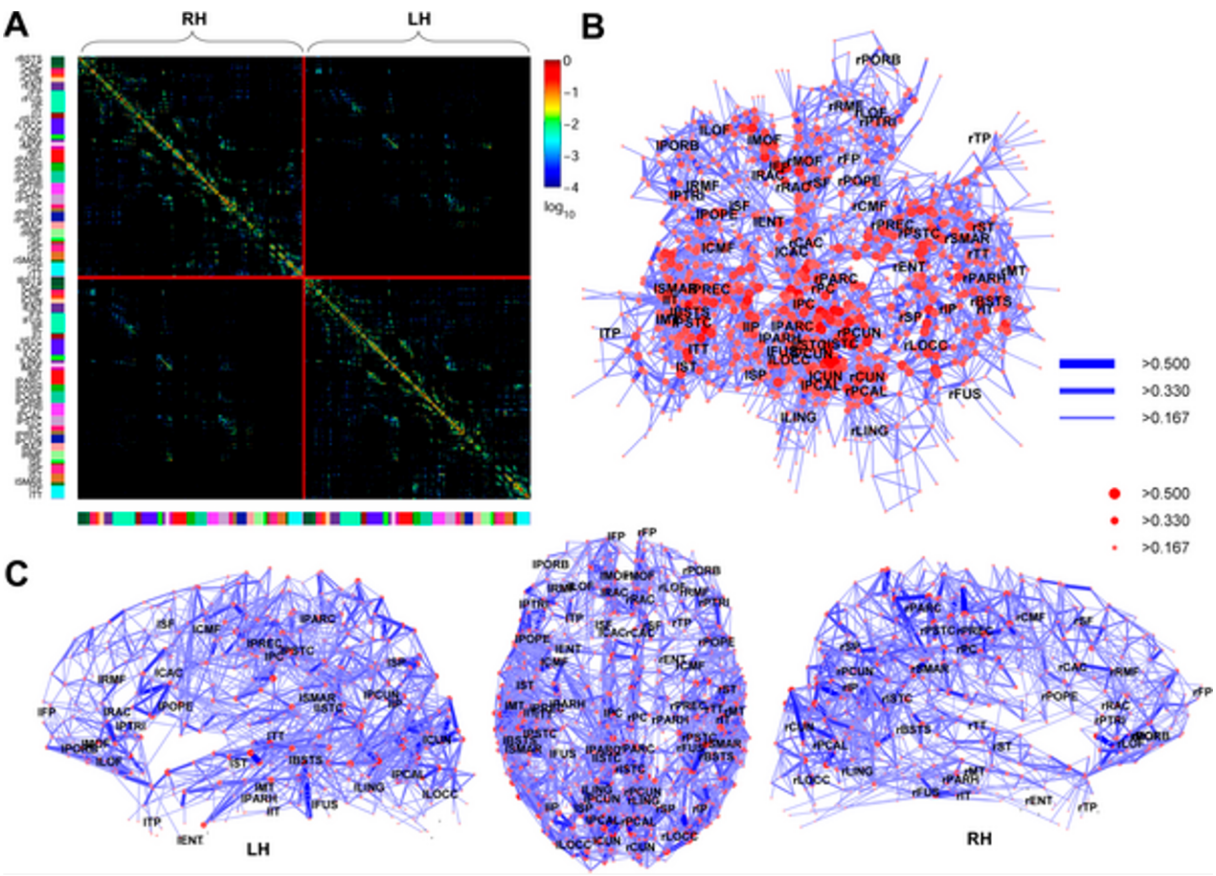

Figure 1.3: High-resolution connectome. (a) Connectivity matrix between all pairs of 998 ROIs, plotted by cerebral hemispheres. The color bars at the left and bottom of the matrix correspond to the colors of the 66 anatomical subregions shown in Fig.1.2. (b) Force-spring layout of the connectivity backbone. Nodes are coded according to strength and edges are coded according to connection weight. (c) Dorsal and lateral views of the connectivity backbone. From [13].

suggesting ongoing information processing and ongoing functional connectivity during rest. Most of the resting-state patterns tend to occur between brain regions that overlap in neuroanatomy and are known to be responsible for the functioning of a particular neural system, like motor, visual or auditory circuits and were demonstrated to be highly consistent across subjects: *"This observation suggests that brain regions that often have to work together form a functional network during rest, with a high level of ongoing spontaneous neuronal activity that is strongly correlated between the anatomically separated regions that form the network"* and *"makes spontaneous resting-state fMRI oscillations a robust measure to examine functional connections between brain regions on a whole-brain scale"* [45]. In addition, it was discovered that these *resting-state networks* (RSN) correspond to the mayor systems in the brain: visual, auditory, sensory-motor, default mode, executive control and dorsal attention [46].

Of special interest is the so-called *default mode network* (DMN). Such network is characterized by "*elevated level of neuronal activity during rest, in comparison to when cognitive tasks are performed, suggesting that activity of this network is reflecting a default state of neuronal activity of the human brain, linked to core process of human cognition, including the integration of cognitive and emotional processing, monitoring the world around us and mind-wandering*" [45].

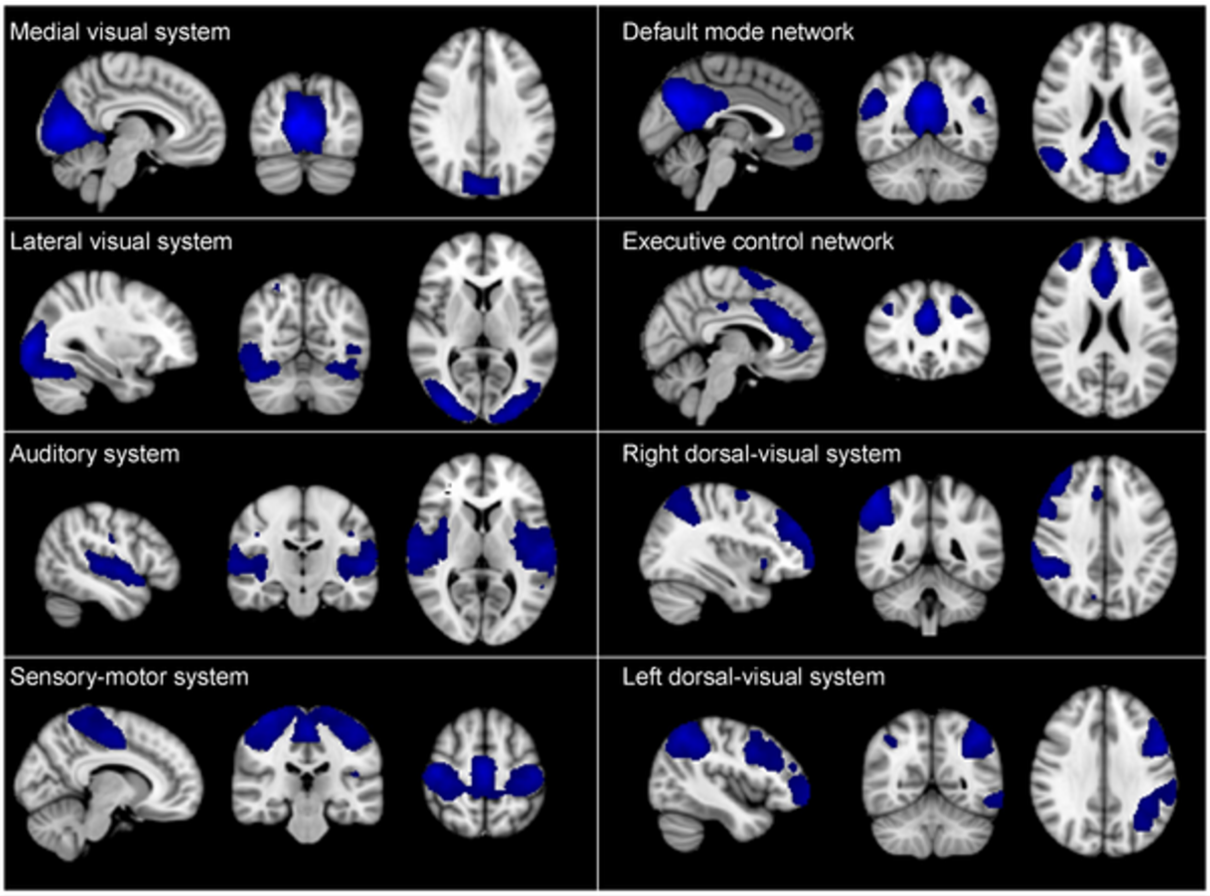

Figure 1.4: Standard masks of resting state networks (RSNs). Blue regions show brain regions included in the RSNs. From [15].

Again, graph analytical methods are used to examine the overall architecture of brain functional networks in the brain. Many studies show an efficient small-world organization, that combines a high level of local connectivity with a very short average distance between the nodes, ensuring a high level of global efficiency. Moreover, the analysis of the degree distribution suggested an exponential truncated power-law in some cases, while scale-free in others. Both class of networks are known for their high level of heterogeneity and resilience against random attack to nodes or edges, indicating a very robust functional network organization. On the other hand, scale-free organization is vulnerable to specialized attacks, especially on the highly connected hub nodes. Indeed, a failure of one of these hubs blocks the communication of signal between distant regions in the brain. It has been hypothesized that specialized hub nodes may be affected in neurological and psychiatric brain disorders as Alzheimer's desease, resulting in decreased functional efficiency in these patients [45].

1.3 Structure-Function relationship

The relationship between structure and function is a central concept in natural sciences. Indeed the architecture and the conformation of living systems mostly determine their biological function. Analogously, the function of the nervous system is shaped by the structure and arrangements of neurons and neuronal circuits. The emergence of network neuroscience offers growing opportunities to quantify the link between the organizational features of neuronal networks and the spectrum of cortical functions. In particular, combined studies of both structural and functional networks in the same subjects have allowed direct comparison of the two. These studies suggest a direct association between functional and structural connectivity in the human brain. Central hubs and clustered areas in structural networks are reflected also at the functional level. Moreover, structural weights are significantly correlated with functional weights [30]. However, the best-case estimates place the correlation coefficient between structural and functional networks are around $R^2 \approx 0.5$ [13], meaning that considerable variance, more than one half, in brain functional behaviour is unexplained by a direct one-to-one correspondence with anatomical structure. Such divergences emerge not only at local spatial scale but also globally. For instance, structural networks display evidence of assortative mixing, indicating that nodes with similar properties are more likely to be connected, in contrast to functional networks (see Sec. A.4.3 for a formal definition of assortativity). The discrepancy is particularly pronounced at the mesoscopic scale, at which clustering or community detection methods applied to structural data fail to identify some of the resting state networks, mainly due to missing anatomical interconnections [30].

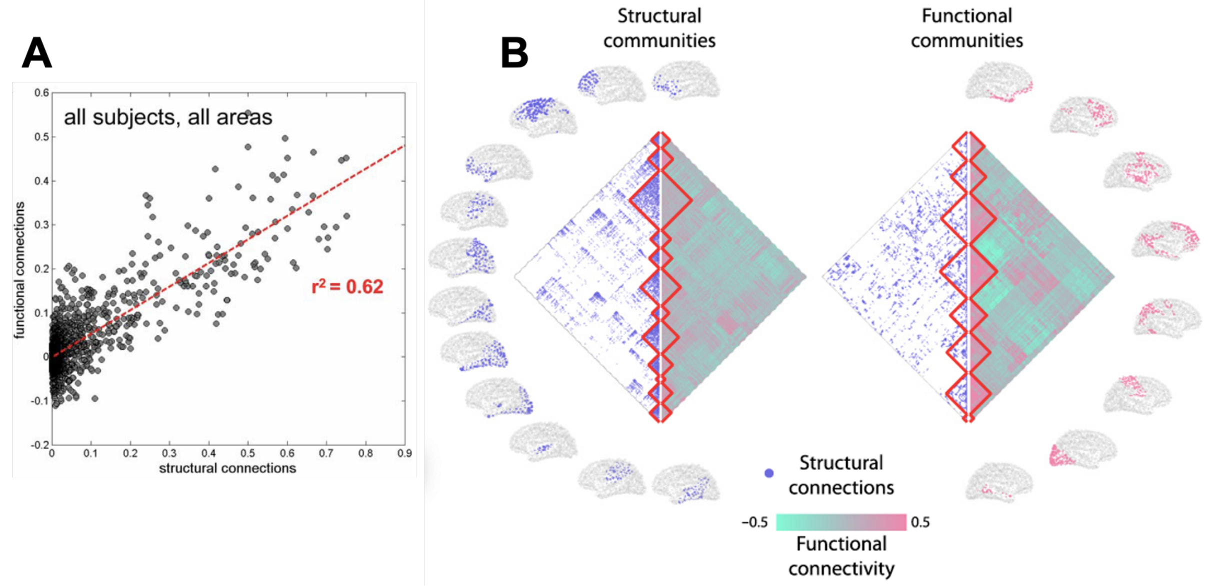

Figure 1.5: Functional connectivity of human brain can be only partially infered from structural connectivity. (a) Linear relation between structural and functional connections in the same subjects explains only around 50% of the variance. From [13]. (b) Community detection alghoritms for structural and functional networks typically yields different solutions. The matrices compare structural and functional connections, arranged following respectively structural (*left*) or functional (*right*) communities. Each community is enclosed in *red squares* and it is reported in the brain atlas around the matrices. From [30].

A plausible explanation of such discordance between structure and function in the brain is the emergence of collective, higher-order interactions among neural elements that is beyond the geometric and local clustered dependence of graph-modeled structures. Functional interactions may result from indirect structural connections, also driven by the common inputs from sensory organs and the entire organism [30]. So brain functioning seems to be an emergent properties of the human brain. This topic will be dealt in more detail in Chapter 2.

Many theoretical and computational models have been proposed to bridge the gap between anatomy and brain dynamics, with a focus on their biological interpretation and predictive utility. A set of these models with a more data-driven approach combine multiple networks from various scale and from different experimental techniques to obtain more sophisticated statistical measures. On the other hand, biologically inspired models generate detailed neuronal dynamics to make inferences and to predict brain functionality from anatomical configurations [29].

Among the other limitations, a relevant issue is the shortage of individual based analysis. Most of the structural and functional description obtained from brain imaging are based on group-average networks, that were demonstrated to be almost stable and reproducible among different studies. However, there is less experimental evidence about the structure-function relationship in individual due to the profound inter-subject variability. Individual differences may provide a probe for investigating the effects of perturbations and modifications as a result of cognitive tasks, development and aging, neurological and psychiatric disease, lesions. How to reconstruct networks while accounting for differences in individual topological organization remains a major question for future studies [30].

Chapter 2

Emergent patterns and Criticality in the Brain

The study of phase transitions is a topic well known by physicists. As you vary an external control parameter, such as the temperature or the magnetic field, in some cases the macroscopic properties of a system will abruptly change. Thermodynamics has formally explained these phenomena as discontinuities in the derivatives of the free energy. If this transition imply a divergence in the response functions, like the susceptibility or the specific heat, we are in presence of a *critical point.* The interest in critical states is related to some unique characteristics that physical systems exhibit in these particular conditions. For instance, the dynamics is mostly governed by the fluctuations of the local properties that govern the dynamics and the correlations extend to the macroscopic size of the system. In addition, fractal structures and complex dynamical pattern appear spontaneously and are self-similar when observed at different spatial scale [47].

Thus a hallmark of criticality is the absence of a typical scale, reflected by a scale-invariance in the physical quantities of the system. The only class of functions that satisfies such scale-free behaviour are power laws $f(x) \propto x^{\alpha}$. A major achievement of statistical physics is the universality of such critical behaviour: interacting systems share the same exponent α if they have the same dimensionality and if the order parameter belong to the same symmetry class, independently of the details of the microscopic components.

Critical phenomena represent only a small portion of emergent properties. The term emergent is used to evoke collective behaviour of a large number of microscopic constituents that is qualitatively different than the behaviours of the individuals [48]. In other words, these properties arise from the collaborative functioning of a group of items, whether insects, atoms or buildings, and are not encoded in any single agent. In fact the definition is fulfilled for instance by neutralization reactions of chemical systems, the construction of hills and dams by ant colonies, the complex social organization of human beings, the cohabitation of many species in ecosystems.

Like ants building up a colony or birds migrating in flocks, no single neuron hold the information for high-level cognitive tasks, like reasoning, processing sensory inputs, feeling emotions. Although the mechanisms of operation is not yet fully understood, cognitive tasks are correlated with complex emergent neural patterns.

2.1 Neuronal avalanches

These scaling patterns are also exhibited by networks of living neurons. Like avalanches [49], earthquakes [50] and forest fires [51], also brain activity can organize into a critical state in which event sizes show no characteristic scale. Back in 2003, Beggs and Plenz [22] investigated the propagation of spontaneous activity in cultured and acute slices of rat cortex on multi-electrode arrays by recording the local electric field generated by the population of neurons, called *local field potentials*. These extracellular signals often display a sharp negative peak, indicating a population spike [22]. So LFPs were binned in time and a threshold was used to determine the events of interest. At a glance, LFPs appear on many electrode in synchronized bursting interleaved by many seconds of quiescence (Fig.2.1-a). Nonetheless, by analyzing the traces at a finer temporal resolution (Fig.2.1-b), it becomes apparent that some LFPs occurred before others, forming a non-synchronous activity that spread over space and time and not propagate only in spatially contiguous electrodes as a wave.

A *neuronal avalanche* is defined as a sequence of consecutively active frames preceded and ended by a blank frame. The variability of these spatio-temporal patterns suggests to analyze the statistics of the size of the avalanches, which was defined in two ways: the number of electrodes activated during the avalanche; the sum of LFP amplitudes above threshold over all electrodes. In either, the distribution revealed a linear relationship in log-log coordinates with a cutoff near the maximal number of electrodes (Fig.2.1-c).

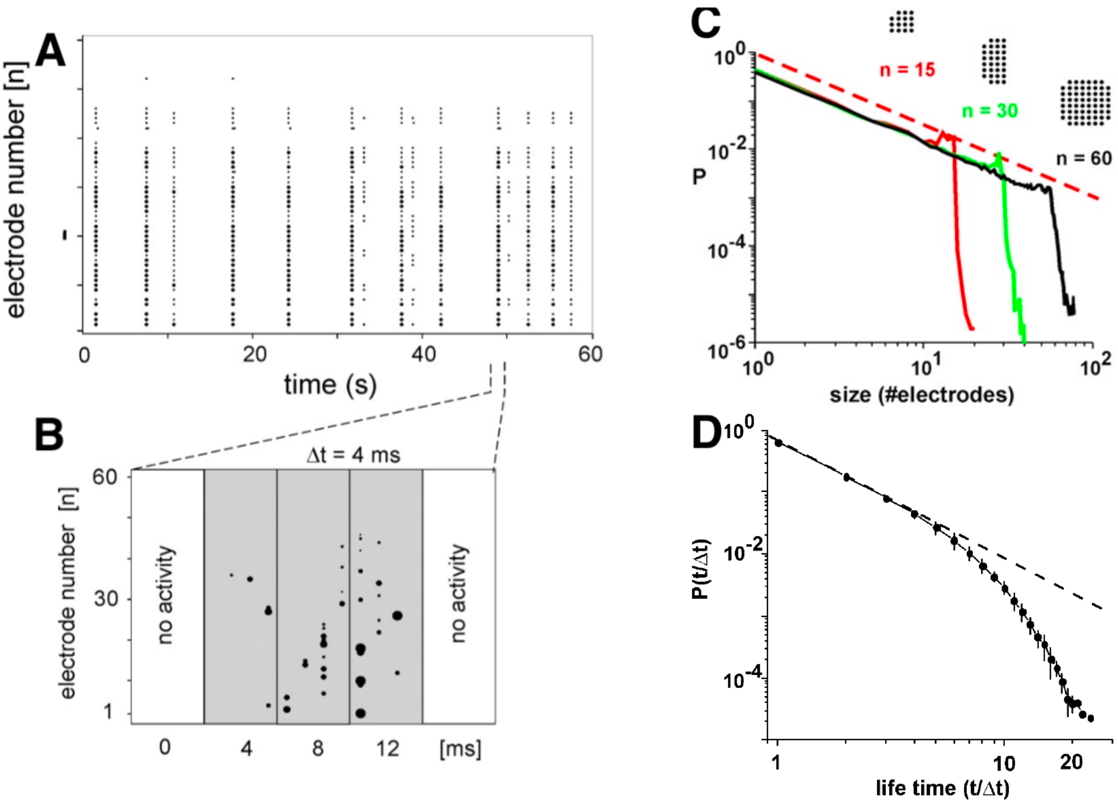

Figure 2.1: Raster plot of spontaneous activity recorded with the multi-electrode array (a) conceals an avalanche of three frames at a finer timescale (b). Distributions of avalanches size (c) and lifetime (d) follows a linear trend in log-log scale with exponents consistent with a critical branching process. From [22].

Instead, the lifetime of an avalanche is simply defined as the count of the consecutive bins in which it is present. By normalizing with respect to the temporal width of the bins, the distribution of lifetimes is likewise scale-free, but with an exponential cutoff (Fig.2.1-d).

These scaling properties provide some critical exponents close to -3/2 and -2 respectively and are shown to be very robust over the change of experimental parameters, like the bin width or the threshold for binarizaring the LFP signals. Such exponents are the same of any model belonging to the universality class of *directed percolation* in dimension larger than or equal to its upper critical dimension $d_c = 4$. What all these models have in common is the presence of a continuous phase transition that occurs between an absorbing and an active phase [52].

A simple toy model that belongs to this universality class and theoretically predict the same slopes is the *critical branching process* [53]. The original purpose of the branching process was the mathematical description of population growth in which each generation produces some offsprings according to some random numbers. The *branching parameter* σ generally indicates the expected number of children of each individual and this model seems to be naturally extensible to a system of excitable units that induce activation in neighbour sites, like a network of neurons. To investigate whether a branching process might properly describe propagation of neuronal activity in cultured populations, the branching parameter was measured directly from the system as the ratio of descendant electrodes to ancestor electrodes for two successive bins in a certain avalanche (Fig.2.2-a) [22]. From theory it is known that $\sigma > 1$ implies a supercritical, active phase in which at each time step the offsprings increases exponentially, while with $\sigma < 1$ the activity decreases over successive steps, eventually dying out (absorbing phase). The direct measurement of σ reveal values close to the critical value ($\sigma = 1.04 \pm 0.19$ for avalanches starting with a single electrode, $\sigma = 0.90 \pm 0.19$ for avalanches starting with more than one electrode) in which activity at one electrode would spread on average to one other electrode, keeping the system at the edge of stability.

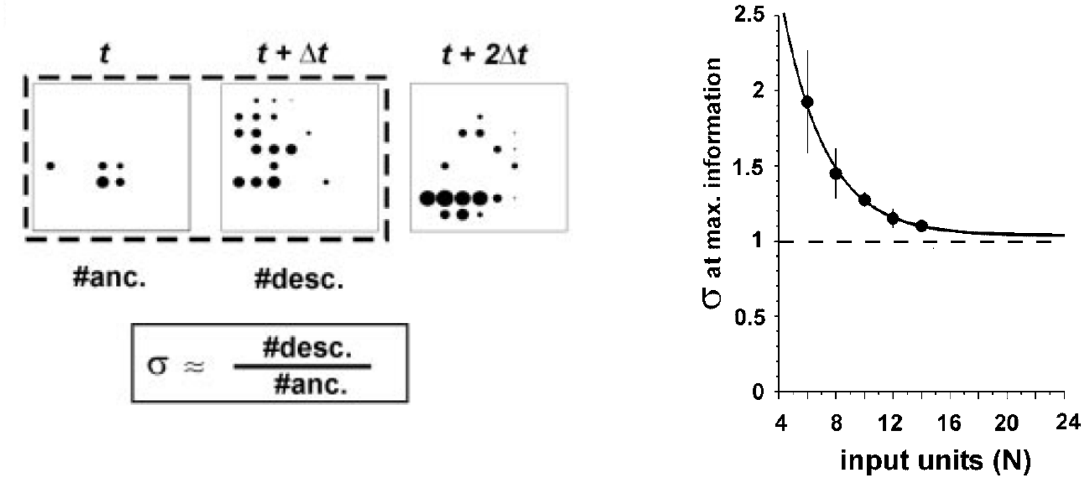

Figure 2.2: Network dynamics in cultured networks are characterized by a critical branching parameter of $\sigma = 1$, suggesting a state of optimal information transmission. (a), Experimentally the branching parameter σ of an individual avalanche is estimated as he ratio of descendant electrodes to ancestor electrodes. (b), In feedforward networks the branching parameter σ that optimizes information transmission approaches 1 for increasing network sizes. From [22].

The compatibility of the experimental branching parameter with critical condition prompts the question of what characteristics might be promoted by criticality from the perspective of signal processing. A way of exploring this issue was based on an artificial feedforward architecture that simulates the propagation of neural activity by associating to each connection a probability of successfully transmitting activity to the next unit [22]. Starting from a random pattern of activation in the input layer, this models allows to test the transmission of information through the network by varying the branching parameter[1]. The peak of information transmission asymptotically approaches the critical values as the number of input units increases (Fig.2.2-b).

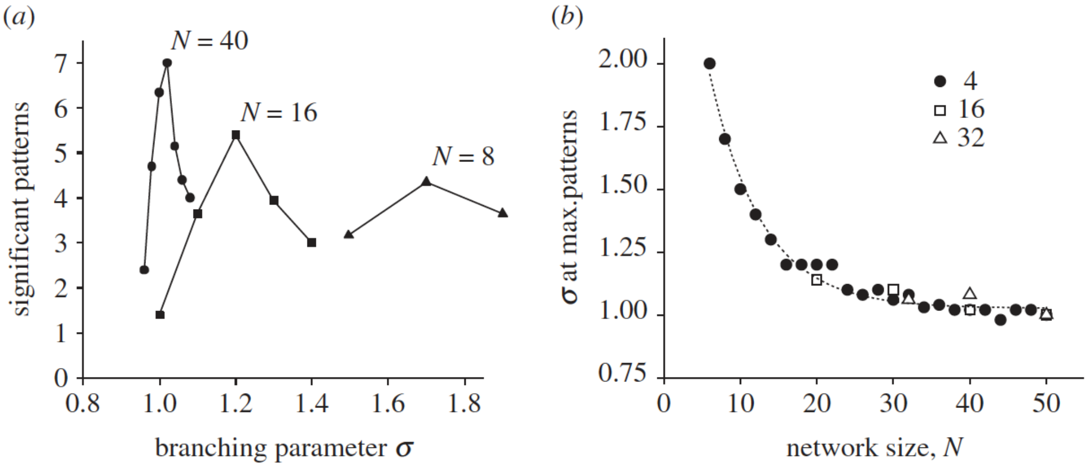

Figure 2.3: Number of statistically significant repeating avalanche patterns is maximized at the critical point. (a) Number of metastable states i.e. significant repeating avalanche patterns as a function of the branching parameter σ for different network sizes. It can be noticed that larger networks peak closer to $\sigma_C = 1$. (b) The branching parameter σ that maximizes the number of metastable states asymptotically approaches $\sigma_C = 1$ regardless of the number of connections per unit. From [24].

In cortical cultures activity does not propagate in a random manner, but in preferred paths that are significantly repeated over several hours. Such activation patterns resemble metastable attractors usually encountered in various physical, chemical, and biological systems, raising the question of what is the relation between the branching parameter and the number of these metastable states. Typically, similar complex patterns of fluctuations arise in critical systems that operate at the border of order and disorder [26]. To address this issue, the branching process was simulated in a network of processing units randomly connected to each other, resulting in a recurrent, rather than feedforward, architecture [25]. Starting with a random activation, the activity of the network is let to evolve for some time steps and then the output configurations are collected. Statistically significant repeating pattern are clustered together and each group identifies a metastable state. Again, the number of metastable stases is maximized at the critical point, that approaches $\sigma = 1$ for large systems (Fig.2.3). Therefore, criticality leads to a wider range of stable patterns in the network and this may be related to optimal information storage in human brain.

---

[1] Branching parameter is defined as $\sigma = \sum_i^C p_i$, where p_i is the probability of transmitting an activation and C is the number of nodes in the next layer. Information transmission is defined as $I(S, R) = H(R) - H(R/S)$, where $H(R)$ is the entropy of the response set, i.e. the possible binary patterns that appear in the output layer, while $H(R/S)$ is the entropy of a response given a stimulus, i.e. binary pattern presented to the input layer, calculated over all responses and stimuli.

These results seems quite reasonable from an intuitive understanding: if the system were subcritical, it is difficult for the network to spread an high level of activity, thus most of the inputs would produce similar attenuated output patterns; on the other hand, if the system were supercritical, any input would lead to a massive activation of the network, so in both cases leading to poor transmission of input information up to the output layer and few achievable configurations.

Although power laws are consistent with the idea of human brain operating near a critical point, their existence alone is not a sufficient condition for criticality [27]. Many studies propose models that produce scale-free behaviour far away from a phase transition (or that do not have a transition at all). For instance, a sparsely connected integrated-and-fire model produces such scalings in the whole range of parameters consistent with a synchronous irregular regime and is claimed to be an effect of the inhibition state, which is absent in a branching process [28]. In another integrate-and-fire model forming an Erdos-Renyi network of neurons, diverse avalanches, obeying scaling, can coexist simultaneously as a result of an underlying neutral dynamics, i.e. each event of activity is indistinguishable from others, a mechanism alternative to self-organized criticality [54].

2.2 Long-range temporal correlations

Other signatures of criticality in neural activity have been proposed. A complementary evidence to scale-free avalanches is the long-range temporal correlations (LRTC) of brain signals, which have been observed both at macroscopic [55] and microscopic levels [56]. The discovery of LRTC in the amplitude envelope of ongoing oscillations was based on 10 subjects recorded with simultaneous EEG and MEG for 20 min during eyes-closed and eyes-open rest [55].

The oscillatory activity was highlighted by peaks in the amplitude spectra both in the alpha frequency band (8-13 Hz) from signals of the occipital and parietal regions, and in the beta frequency band (15-25 Hz) from signals of the somatosensory region. To quantify the temporal structure of amplitude fluctuations, power spectrum and autocorrelation analysis were performed. The power spectrum exhibits a $1/f^{\beta}$ power-law decay (Fig.2.4-a,b) that indicates a lack of a characteristic scale for duration and recurrence of oscillations. Likewise, the autocorrelation shows a slow decay well-fitted by a power law, with statistically significant values up to time lags larger than 100 seconds, indicating that brain areas are functionally correlated for quite long period of time (Fig.2.4-c,d).

Once more, these spatio-temporal patterns of large-scale dynamics could be the result of a system self-organized close to a critical state and may provide neural circuits with the ability of integrating information over extended periods of time, an essential ingredient for information processing. For example, in decision-making and working memory tasks, this ability may increase the signal-to-noise ratio and may afford to maintain some memories of past activities [57]. A deviation from this behaviour may be responsible of lower cognitive abilities. Indeed, a reduction in the long-range correlations was proven in pathological conditions like schizophrenia [14] and lack of sleep [58].

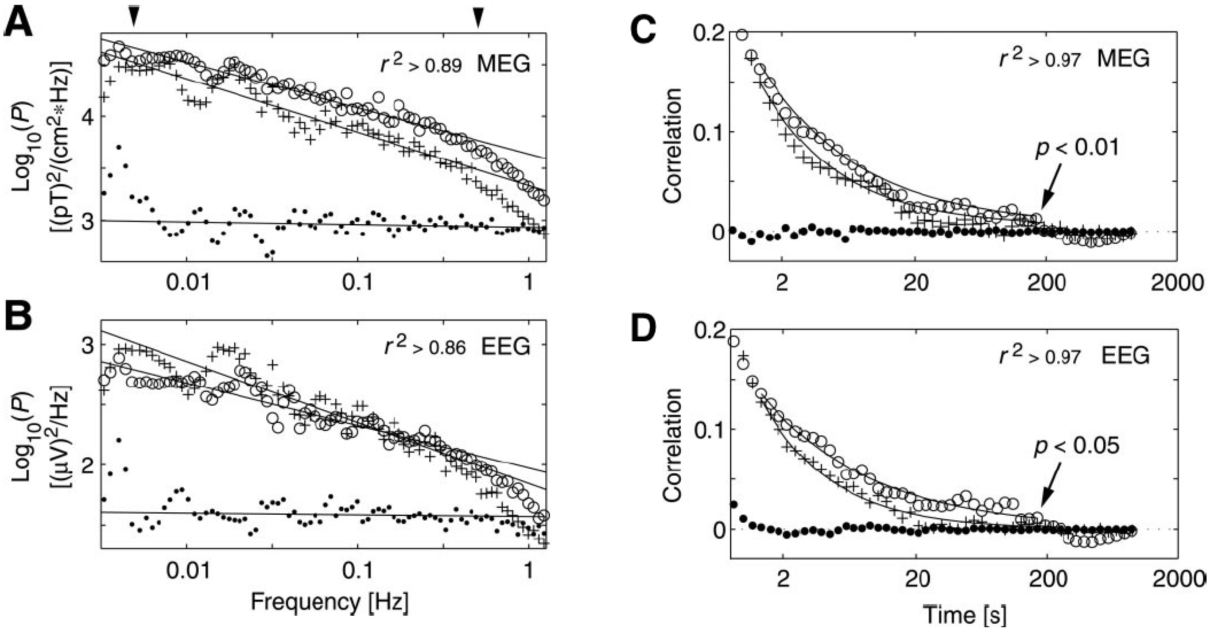

Figure 2.4: Alpha oscillations exhibit power-law spectra and long-range temporal correlations. The power spectral density is reported in double logarithmic scale for MEG (a) and EEG (b). *Arrowheads* mark the interval used for estimation of slopes. The autocorrelation function of amplitude fluctuations is reported both for MEG (c) and EEG (d) with increasing time lag. *Circles*, eyes-closed condition. *Crosses*, eyes-open condition. *Dots*, reference recording. From [55].

2.3 Signatures of criticality in Resting State Networks

In Sec.1.3 we have already argued how functional patterns of the brain at global scale might emerge from non-linear neural interactions between spatially segregated regions.

The 2-dimensional Ising model can be used to model an effective functional network. In particular, functional links are placed between nodes that have a pair-wise cross-correlation larger than a fixed threshold. Such functional Ising networks obtained at the critical temperature are claimed to be ”indistinguishable” from brain functional connecitivity data, while they strongly differ from brain networks in the sub- and super-critical phase [59]. Moreover, the fat-tail statistic of the number of links, i.e. the degree distribution, in resting state networks (RSNs) can be replicated by the 2-dimensional Ising model only when it is poised at critical temperature [59].

Another direct evidence of critical dynamics was discovered in the phase synchronization. The phase lock intervals[2] display a scale-free distribution, typical of critical phenomena [60]. Furthermore, such trend is replicated by the Ising model and the Kuramoto model, a system composed of an ensemble of coupled oscillators each with its own natural frequency, again only if tuned at criticality [60].

---

[2] defined as the length of time that a pair of neurophysiological signals, simultaneously recorded from two different MEG sensors or two different brain regions in fMRI, are in phase synchronization with each other

2.4 Importance of being critical

The human brain, in all its staggering complexity, is the product of millions of years of evolution. *"If the ability of an organism to process information about its environment is a driving force behind evolution, then the more information a system, such as the brain, receives, and the faster it can process this information, the more adequately it will be able to respond to environmental challenges and the better will be its chances of survival"* [61]. Although the details of the interpretation of the neuronal organization are still controversial, it is evident that the potential for brain evolution results not from the unorganized aggregation of neurons, but from their cooperative association.

We have already pointed out how the information processing and storage in the brain may be improved at criticality [24]. *"The limit to any intelligent system therefore lies in its abilities to process and integrate large amounts of sensory information and to compare these signals with as many memory states as possible, and all that in a minimum of time"* [61]. In order to do that, the brain needs to discriminate the largest range of environmental stimuli and to have access to the largest repertoir of states.

The dynamic range can help to quantify the responsiveness of the brain when subject to external stimuli. Widely used in psychophysics to study how physical stimuli transduce into psychological sensations, it is defined as the logarithm of the ratio between the largest and the smallest value of the stimulus that is robustly coded in variations of the response (see Sec.3.4.2 and Eq.3.14 for a more formal definition). Studies on networks of excitable elements pointed out that the dynamic range of a single neuron is substantially smaller than the dynamic range observed at the macroscopic level and is maximized at the critical point, providing further insight into emergent properties of the brain [23].

The diversity of activation patterns or global brain states reflects its information capacity and contributes to the state of consciousness of an individual [62]. The repertoire of these brain states was also explored by simulating dynamic interaction of mesoscopic brain regions using a modified spin-glass model [26]. Resting state fMRI was recorded from 20 partecipants and mapped to 10.000 cortical regions. The resulting correlation matrix, averaged across subjects, was used as connectivity matrix for the simulation. According to the Ising model, each site stochastically transitioned between up (active) and down (inactive) states under the net influence of nearest pairs. The probability of local transitions was controlled by a single parameter T, analogous to temperature in the classical Ising model, that corresponds to the level of global cortical activation. A small sample of pattern is reported in Fig.2.5-a. To measure the temporal diversity of metastable states over time at all time lags, the *dispersion index* D is defined as

$$D = K\frac{<(1-cc)>}{var(cc)} \tag{2.1}$$

where cc is the pair-wise temporal correlation matrix between states at different time lags, K is a normalization constant equal to the variance of the uniform random distribution of the same size as the cc matrix [26]. It was computed as a function of the control parameter (Fig.2.5-b). At intermediate values, metastable states dominate and the diversity of brain states as measured by dispersion index is maximum, while its value drops sharply at both smaller and larger T, suggesting the presence of a second-order phase transition. Low values of activation level may characterize suppressed cognitive states such as anesthesia

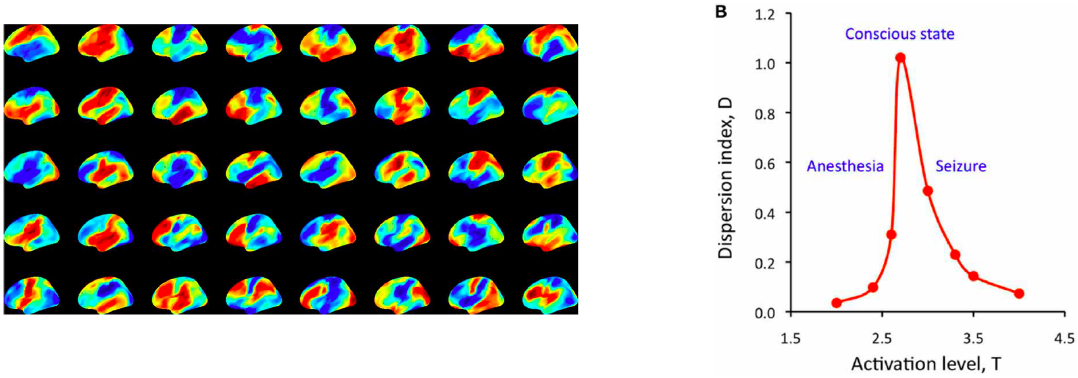

Figure 2.5: Spin-glass model predicts metastable brain states that maximize at critical activation level. (a) The 40 most frequent patterns at $T = 0$ activation level. Pseudo-color indicates the probability of up (red) and down (blue) states of each site (arbitrary scale). (b) Dispersion index D shows critical behavior as a function of activation level T. From [26].

or deep sleep, while high values are thought to correspond to hyper-activated conditions, like epilepsy [62].

A typical measure of the number of configurations to which a certain system has access is entropy. This definition, which comes from statistical mechanics, has been proven equivalent to Shannon entropy in the context of information theory. Given a random variable, Shannon entropy is the average amount of information in a possible outcome. From such definition, entropy is strictly related to transmission and storage of information, since from a theoretical point of view it is maximized by an optimal transmission channel [63]. We can thus understand the reason why human cognition benefits from being critical and having access to a large number of metastable states. In support of this, a study on fMRI data in a large sample of healthy adults has examined brain entropy, which was found to correlate with higher intelligence measures in several key brain areas [64].

2.5 How to build a critical brain

Human brain might have tuned at the edge of a phase transition to take advantage of this optimal processing properties. Nonetheless, criticality is not driven by any external parameter, like temperature or magnetic field as usually happens in physical systems, but emerges from the dynamical interaction of neurons. This phenomenon was already found in other biological systems and is named *self-organized criticality*, which is easily implemented by a feedback mechanism that increases the control parameter in the subcritical phase and decreases it in the supercritical phase [16].

One can therefore ask how a complex and highly variable system such as the brain can remain correctly tuned to this state. Moreover, the brain is constantly subject to environmental stimuli, thus the self-organization is continuosly reached in a dynamical way. An important mechanism that alters brain structure by adjusting the strength of connections between neurons and regulating the firing rates is the *spike timing-dependent plasticity* (STDP). Input spikes occurring in the presynaptic cells immediately before those in the postsynaptic cell strengthen the connection in a phenomenon called long-term potentiation (LTP). In this way, inputs that might be the cause of the post-synaptic neuron's excitation are made even more likely to contribute in the future, in the spirit of Hebbian's postulate about synaptic learning rule synthesized in the famous quote "*cells that fire together wire together*". In a totally opposite way, synaptic efficiency decreases when the firing of their incoming links is persistently independent of firing their outgoing ones, resulting in long-term depression (LTD).

This mechanism, unless mitigated by other processes, may alter the excitation of a neuron dramatically, pushing into an unstable phase, out of its ideal functional regime. These considerations have encouraged to investigate additional types of plasticity, complementary to STDP, that may constraint synaptic weights and modulate neuron's intrinsic excitability around its optimal working point. Some of these strategies are collected under the name of *homeostatic plasticity*. In complicated neural circuits, homeostatic regulation might require multiple processes acting on different timescales and in different ways. The major ones are: synaptic scaling, that occurs at the level of individual neurons and keep its synapses within some optimal and energetically advantageous size range; homeostatic intrinsic plasticity, whereby the expression of voltage- and calcium-gated ion channels adjusts the gain and the threshold of individual neurons; metaplasticity, embedded in the rules of Hebbian plasticity itself, for which the synapses undergo Hebbain modification based on previous history of neuronal activity, thus being a plasticity of the plasticity itself [65].

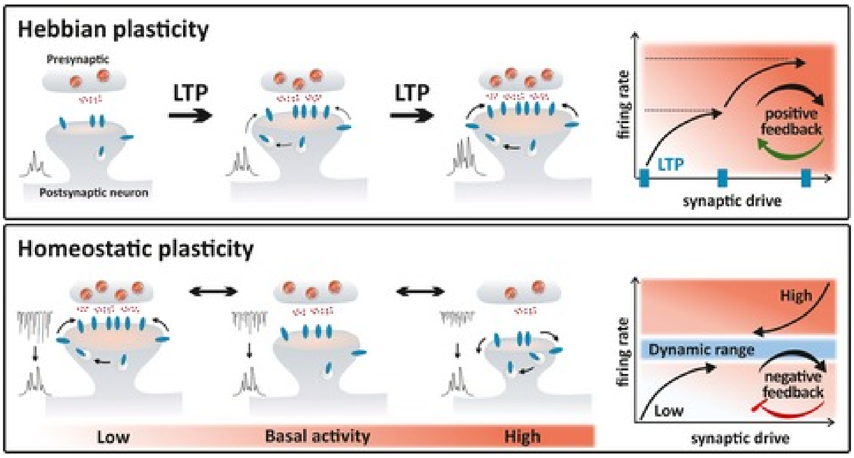

Figure 2.6: Different mechanisms of plasticity in synaptic strength dynamically tune the brain at criticality. Hebbian forms of synaptic plasticity, such as long-term potentiation (LTP), induce long-lasting changes in synaptic strength, which can be destabilizing and drive activity to supercritical regime. Conversely, homeostatic plasticity operates to compensate, stabilizing neuronal firing within a dynamic physiological range. From [66].

According to these mechanisms, self-organization seems to rely on the dynamics of local neuronal excitability rather than global regulation. Although synaptic conductances seem to be a plausible candidate as a control parameters driving the brain to the critical phase, many questions remain to be addressed about this topic [16]. Moreover, due to the highly hierarchical and modular structure of the anatomical structural matrix and due to the abundance of parameters that affect the dynamics, the global phase transition is spread out over a broad range of parameters, better appointed as critical region rather than critical point, where different modules may be in the supercritical region, while other are in the subcritical regime, maintaining equally optimal global cognitive capabilities typical of criticality. In addition, different regions may be perhaps tuned to different phase transitions, each one beneficial for various specific cognitive process [16].

Chapter 3

A stochastic whole-brain model of the human connectome

In Chapter 2 we have provided some highlights of the so called *critical brain hypothesis*, i.e. that human brain might work at the edge of a critical transition as this might be quite beneficial for information processing and transmission. These experimental and theoretical results have prompted the search for computational models consistent and capable of reproducing such behaviours.

A large class of models suitable for modelling neural activity is the one of *excitable media*. These are nonlinear dynamical systems in which a wave can propagate through the medium, after which it undergoes an inhibition phase and cannot support the passing of another wave until a certain amount of time, called *refractory time*. Like a fire burning in a forest, there cannot be another fire until the vegetation has grown back to support it [67].

A similar behaviour is observed also in neurons in the spreading of action potentials (Fig.3.1). The synapses collect electrical signal from neighboring neurons, causing a change in the resting membrane potential ($\approx -70mV$) of the receiver. If the incoming stimulus is large enough to depolarize the neuron up to a certain threshold potential ($\approx -55mV$), it triggers the inflow of sodium ions in a positive feedback, leading to an abrupt peak in the membrane potential that travels all along the axon. This is followed by the opening of potassium channels, whose outflow tends to hyperpolarize the membrane back to negative values. In the following milliseconds an action potential cannot be triggered again, until the the neuron restores the intracellular ion concentration, bringing the membrane back to the resting potential. This phase is called *refractory period* [31]. At a larger spatial scale, the same functioning consisting of moment of strong activation interspersed with silent phases can be extended more generally to neural signals between mesoscopic regions of the brain.

In the rest of this work we focus on a stochastic whole-brain model [35] built on top of the human connectome derived from DSI scans of white matter fiber tracts [13]. As done in [68], we name it "HTC" model from the initials of the first proposers. What makes this model interesting is that it is capable of reproducing some experimental findings seen in fMRI experiments when tuned at its critical point.

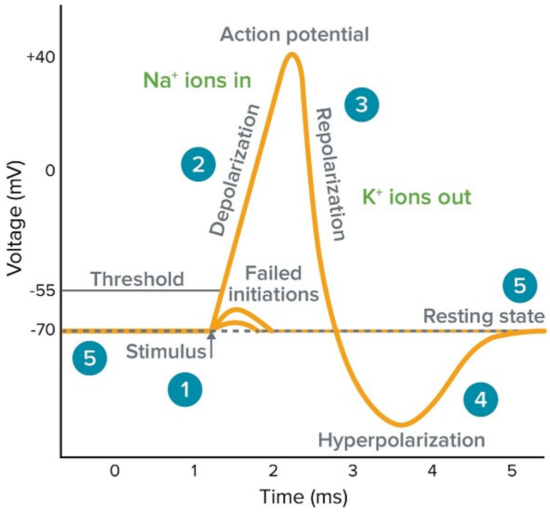

Figure 3.1: Schematic representation of an action potential. 1) An incoming stimulus causes a change in the membrane potential. 2) If the membrane potential exceeds the threshold potential, the opening of sodium channels leads to a strong depolarization. 3) The outflow of potassium ions repolarize the membrane 4) up to lower values than the resting potential. 5) Ion pumps bring the neuron back to the resting potential.

3.1 HTC model

The model consists of a network of interconnected excitable nodes following the dynamics of the *Greenberg-Hastings cellular automaton* [69]. The connections between the units are summarized by a symmetric weighted matrix W, where each entry represents the strength of the interaction between a pair of nodes. Each node can be in one of three possible states: active (A), inactive (I) and refractory (R). The state variable of a given node i, $s_i(t)$, is set to 1 if the node is active, 0 otherwise. The temporal activity of the states evolves according to the following transition rules:

$$\begin{cases} I \to A & \text{if } \sum_j W_{ij} s_j > T \text{ or with prob. } r_1 \\ A \to R & \text{with prob. } 1 \\ R \to I & \text{with prob. } r_2 \end{cases} \tag{3.1}$$

where:

- W_{ij} is the weight of the connectivity matrix of the underlying network from node i to node j
- r_1 is the probability of self-activation
- r_2 is the probability of recovery from refractory state
- T is a threshold which governs the induced activation due to interaction with neighboring nodes[1]

With this modeling the temporal evolution of each unit roughly resembles the functioning of a neuron: it can activate if the (weighted) combined activity of neighbours exceeds a

---

[1] Threshold T should not be confused with temperature, a common control parameter in statistical systems. Indeed, high temperature favors particles motion and leads to a super-critical phase, the same is obtained in the HTC model for low value of T.

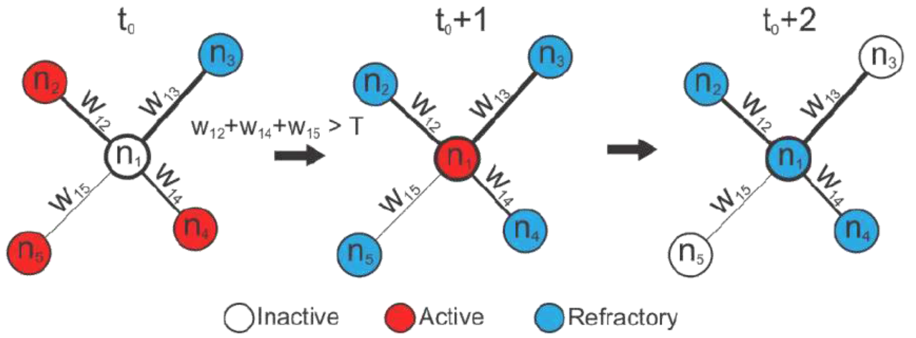

Figure 3.2: Example of dynamical transition of the HTC model: active nodes at t_0, respectively n_2, n_4 and n_5, excite n_1 at t_0+1, while they become refractory; at next step t_0+2, n_3 and n_5 have recovered and are susceptible of excitation again. From [70].

certain threshold T or due to an external stimulus r_1; after the activation, the neuron transitions to a refractory state and cannot activate again; it can escape from inactivity after a refractory period modeled on average by r_2 (Fig.3.2).

In order to characterize the simulated brain activity, the following quantities are considered:

- average network activity:

$$\langle A\rangle = \frac{1}{t_s}\sum_{t=1}^{t_s} A(t) \tag{3.2}$$

- standard deviation of network activity:

$$\sigma(A) = \sqrt{\frac{1}{t_s}\sum_{t=1}^{t_s}(A(t)-\langle A\rangle)^2} \tag{3.3}$$

  These two metrics capture the amount of activation in the global brain dynamics and its temporal variability.

- average of first and second largest cluster $\langle S_1\rangle$ and $\langle S_2\rangle$:
  Clusters are defined as network components that are structurally connected (i.e. $W_{ij} > 0$) to each other and simultaneously active (see also Sec.A.3).

where the activity for a network of N units is defined as the fraction of active nodes at a given time:

$$A(t) = \frac{1}{N}\sum_{i=1}^{N} s_i(t) \tag{3.4}$$

3.1.1 Dynamics and phase transition of the model

The simulations of HTC model were run keeping fixed r_1 ($\approx 10^{-3}$) and r_2 ($\approx 10^{-1}$) while varying T, which takes on the role of control parameter. For each value of the threshold T, the network states are updated for t_s time-steps, starting from a random configuration of active A states. From here on, unless otherwise specified, the observables are averaged over an ensemble of 100 different time-series, evolved for 6000 steps from a random initial configuration of 10% active nodes. In order to sample values near a stationary state, we let the system run for 100 steps before starting to collect data.

HTC model was originally run [35] over the structural network of neuroanatomical connections reported in Figure 1.3-a. We repeat the same study, whose results are reported in Figure 3.3. As depicted in these graphs, the dynamics of the model shows a transition between two regimes. For small values of T, even the weakest connections are enough to cross the threshold, easily transmitting activity to neighboring nodes. This leads to a regime of high activation of the network and the nodes manage to create a giant cluster that covers almost 20% of the system. We refer to this phase as "super-critical" (Fig.3.4, *left column*), characterized by sustained activation with fast and temporally uncorrelated fluctuations, as suggested by the flat spectrum and the quick decline of the autocorrelation. At the opposite side, for high values of T, only the few strongest connections are able to support the activity, resulting in a suppressed or "sub-critical" phase with regular, low-frequency and short propagating brain activity (Fig.3.4, *right column*) in which nodes fail to give rise to relevant clusters. At intermediate values of T, a continuous transition connects the two regimes, resembling a second-order phase transition (Fig.3.4, *central column*) with synchronous activity.

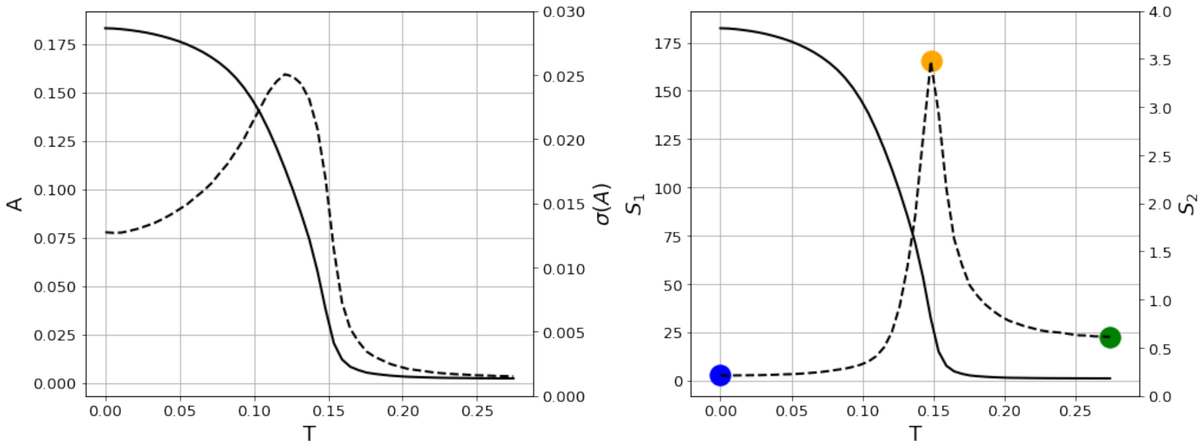

Figure 3.3: Dynamics of HTC model undergoes a second-order phase transition by varying the threshold T, as identified in the peak of the variance and the second largest cluster. (*left*) Average brain activity A (*solid line*) and its standard deviation $\sigma(A)$ (*dashed line*) for different values of threshold T. While A monotonically decreases to zero, $\sigma(A)$ shows a peak for intermediate value of T. (*right*) Average size of first S_1 (*solid line*) and second S_2 (*dashed line*) largest clusters display the same behaviour. (*colored dots*), values of T corresponding to Fig.3.4 and Fig.3.5.

Given that, the mean activity and the size of the largest cluster can be seen as order parameters, like magnetization in the Ising model, discriminating a chaotic, epileptic phase from an ordered, anesthetized phase. Similarly, the second cluster size and the variance, can be seen as a response function diverging at the critical point. We highlight that the identification of the critical point is formally defined only in the thermodynamic limit. Therefore, we use as operational definition of a critical point for a system with finite size (like the considered connectome) the value of the control parameter for which the we have the peak of the size of second largest cluster as a function of T - see Figure 3.3. This picture is supported by theoretical works in percolation theory that predict a divergence in the second largest cluster at criticality [71, 72], in which the system is at the edge of coalescing into a giant cluster, thus being a suitable observable for characterizing

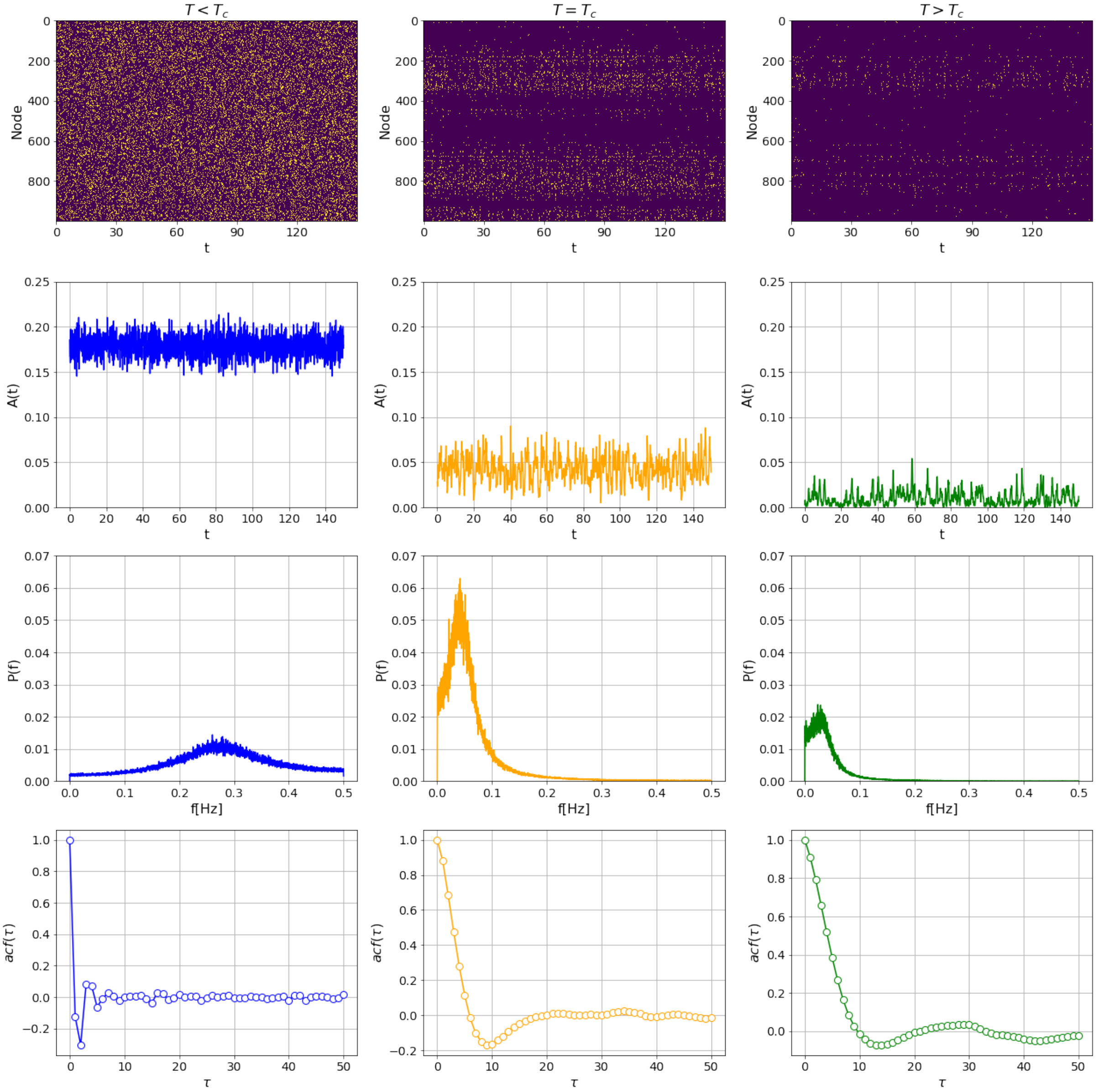

Figure 3.4: Simulated brain activity with HTC model for different value of threshold T, respectively supercritical (*left, blue*), critical (*center, yellow*), and subcritical (*right, green*). (*first row*), raster plot of nodes activation during a small time window of 150 seconds shows different pattern of activation. (*second row*), the trend of the activity is summarized by the average number of active node during each time step in the same time window. (*third row*), power spectrum is similar to a white noise for low values of T, indicating a strongly uncorrelated activity, while small burst of low frequency emerge for high values of T, with a peak thas slowly drift to smaller frequencies as T increases. (*fourth row*), autocorrelation drops rapidly to zero for low value of T, while for high value of T it has non-negligible values up to ten steps, indicating synchronized burst of activation.

the phase transition. In addition to this, also the fluctuations of the global brain activity display a peak for intermediate value of T. A higher variance in global activation is linked to a richer dynamics of the brain network and better distributed between all the nodes in the system. As discussed in Chapter 2, the repertoire of neural patterns is thought to be maximized at the edge of a second-order phase transition, allowing us to infer the critical transition by means of the standard deviation. The difference in the values of T_C

obtained with the two measures are thought to be a finite-size effect and hopefully they coincide in thermodynamic limit.

3.1.2 Numerical versus empirical results

HTC model brutally simplifies the stunning amount of degrees of freedom characterizing the underlying neurophysiological processes. Nevertheless, what makes it appealing is that, when tuned at its critical point, is able to recover some experimental findings seen in fMRI human data. Such comparison can be performed in two opposite directions: by projecting fMRI experimental time series to on-off states like HTC states, or by processing simulated data to obtain BOLD-like signals.

In [70] BOLD signals from resting state fMRI data were mapped to binary activation of voxels at the same spatial resolution of the human connectome used for the simulations. The experimental distribution of clusters from such binarized activity, following a power-law trend, was shown to closely match the simulated distribution of cluster sizes at the critical threshold T_C (Fig.3.5, *yellow circles*).

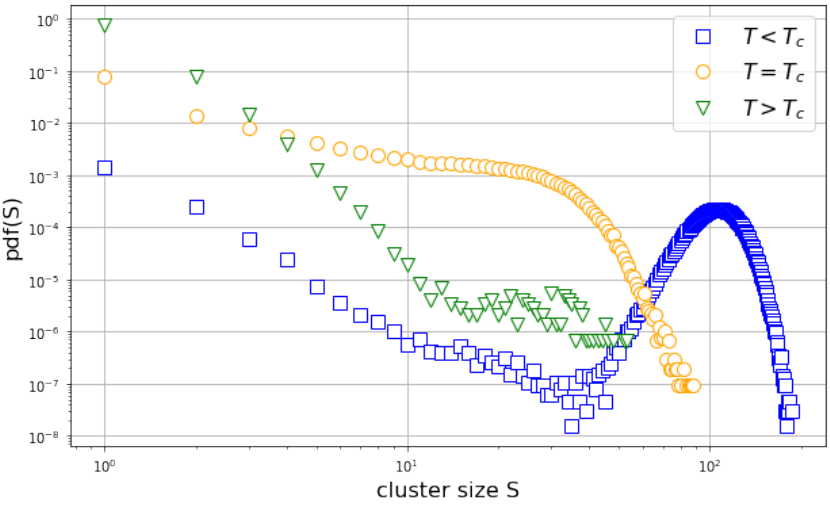

Figure 3.5: Distribution of cluster sizes for different value of threshold T, respectively supercritical (*squares, blue*), critical (*circles, yellow*), and subcritical (*triangles, green*). In the supercritical regime, only few sparse clusters appear. In the subcritical regime, the distribution shows the presence of a giant cluster at about $S \sim 10^2$. At the critical point, the distribution follows a power-law with a cut-off around $S \sim 5 * 10^1$.

On the other hand, a standard procedure to transform model output in BOLD functional signals is to convolve node activity $s_i(t)$ with a canonical double-gamma *haemodynamic response function* (HRF):

$$x_i(t) = \int_0^\infty s_i(t-\tau)h(\tau)d\tau \tag{3.5}$$

with:

$$h(\tau) = \left(\frac{\tau}{d_1}\right)^{a_1} exp\left(-\frac{\tau - d_1}{b_1}\right) - c\left(\frac{\tau}{d_2}\right)^{a_2} exp\left(-\frac{\tau - d_2}{b_2}\right) \tag{3.6}$$

Such procedure is very common in Neuroscience and it is supported by many empirical studies demonstrating that, after a stimulus was presented to a subject and consequently there is the activation of a brain area, an increase in BOLD signal is observed in MR measurements with a similar shape in different neural circuits [73]. In other words, the parameters describing the HRF function Eq.3.6 might change, but the overall shape is consistent and quite robust over brain regions [74].

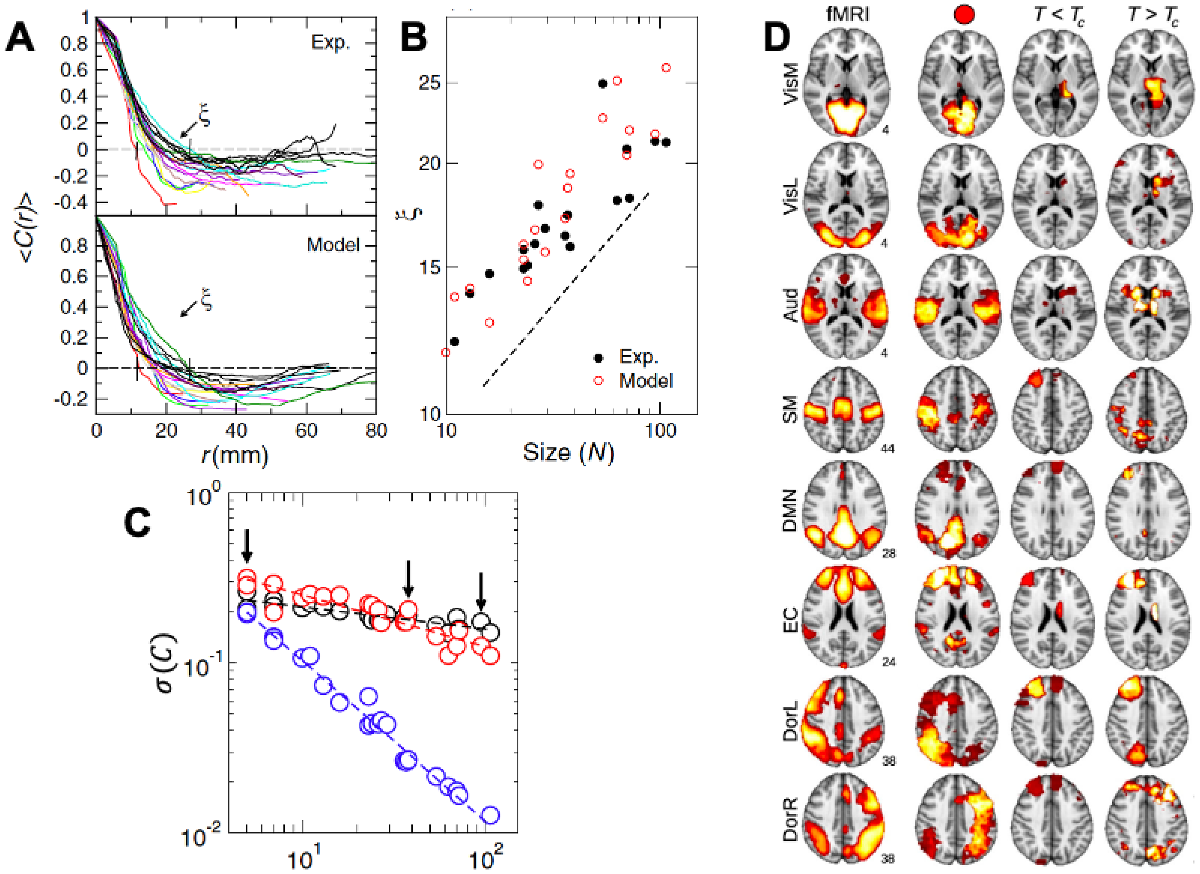

Figure 3.6: Simulated activity of HTC model at critical threshold T_C matches some experimental findings from resting state fMRI data. (a) Correlation function $C(r)$, averaged over nodes in the same RSN, computed for the model at T_C (*bottom*) closely matches experimental data (*top*). Each color represents a different RSN. (b) Correlation length ξ scale as $\xi \sim N^{1/3}$ as a function of the RSN size, both in the experiment and model data. (c) Variance of the fluctuation of the correlation function $\sigma(C)$ remains approximately constant for the human brain data (*black circles*) and for the model at T_C (*red circles*), while in the supercritical regime $T < T_C$ (*blue circles*) the variance decreases faster as the size N increases. (d) RSN from human brain data (*left column*) is better reproduced by the model at T_C (*filled circle*). From [35].

Once obtained the simulated BOLD time series, it is possible to compare the behaviour of resting state networks (RSNs) and investigate whether HTC model is predictive of some feature of human brain activity. In [35] the correlation function between nodes belonging to the same RSN was computed as a function of the physical distance between pairs of nodes, both for experimental and simulated data. When the model is tuned at T_C, the correlation function for each RSN is significantly correlated with the experimental trend (Fig.3.6-a). Moreover, the correlation length, i.e. the distance at which the correlation function approaches zero, in fMRI analysis was proven to scale with the number of units N in the RSN. A similar scaling is replicated by the model only at criticality (Fig.3.6-b). The same happens for the variance of fluctuations in the correlation, that is almost independent on N, while these rapidly decrease in the sub- and super-critical phase (Fig.3.6-c).

More generally, the overall activity of RSNs is better reproduced by the model at criticality. A visual proof is reported in Figure 3.6-d, but also quantitative comparisons highlight an increased correspondence of functional matrix at criticality.

Summarizing, HTC model proposes further confirmations on the critical nature of brain functioning.

3.2 Homeostatic plasticity

The dynamics of HTC model is mostly governed by the weights of the connectivity matrix. The activation of a node is subjected to the cooperation of active neighbours, it integrates signals from all the connected units, weighted by the strength of each link, and spikes if the overall influx is larger than the threshold. Therefore, the transmission of activity is favored by stronger and more binding edges and clearly more connected hub with larger degree (i.e. $\sum_j W_{ij}$) dominate network excitability. However, such inhomogeneity is not encountered in biological brain networks.

A plausible synaptic mechanism aimed at regulating excitation in neural systems is *homeostatic plasticity*. As we already discussed in Sec.2.5, homeostatic mechanisms are a key requirements for the maintaining of the self-organized criticality in the human brain. In [68], homeostatic plasticity was included in the HTC model through a normalization of the structural matrix W:

$$\widetilde{W}_{ij} = \frac{W_{ij}}{\sum_j W_{ij}}. \tag{3.7}$$

In words, each entry W_{ij} is normalized by the sum of incoming weights, thus fixing the in-degree of all nodes to 1 and ensuring that *"each node has at the mesoscopic level a similar contribution on regulating the simulated brain activity"* [68]. We highlight, that because of this normalization, the weighted adjacency matrix is not symmetric anymore.

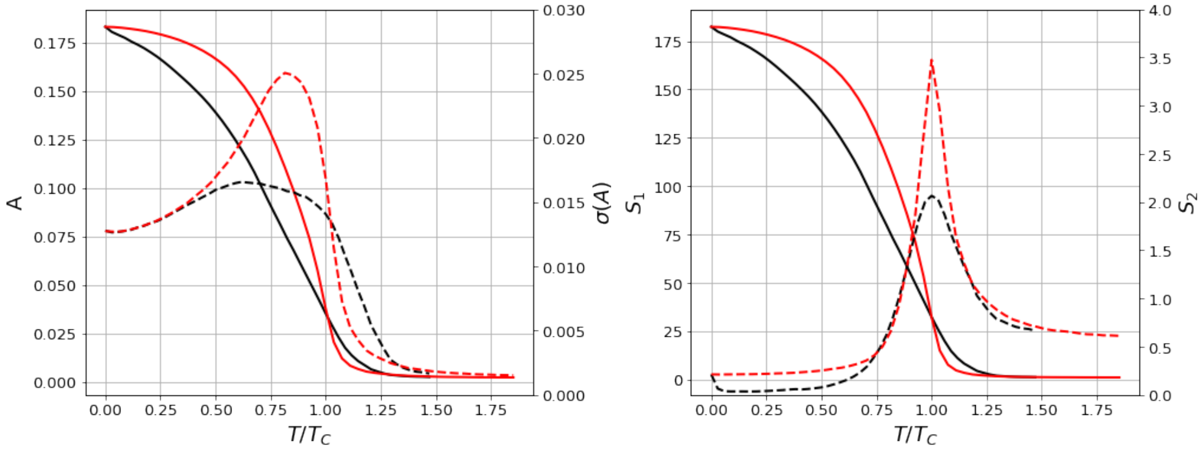

Figure 3.7: Homeostatic plasiticity principle, encoded in the normalization Eq.(3.7), increases the peak in both $\sigma(A)$ and S_1. (*left*), average brain activity A (*solid line*) and its standard deviation $\sigma(A)$ (*dashed line*) for different values of threshold T. (*rigth*), average size of first S_1 (*solid line*) and second S_2 (*dashed line*). (*black curves*), original connectome. (*red curves*), normalized connectome. The critical threshold T_C is assumed as the peak of the second cluster size S_2.

Homeostatic plasticity mechanism has an important implication in system dynamics and the emergence of the critical phase transition. Indeed, the mean activity and largest cluster size are not significantly affected by the normalization, but both peaks in $\sigma(A)$ and S_2 become more pronounced (Fig.3.7). In this way homeostatic principle may help to distribute the activity more evenly across the network, improving information processing in the brain. Not only this, but in [68] the authors highlight how the correspondence between experimental and simulated functional network is increased after such normalization.

Moreover, another important result is the universality of the different curves obtained from connectomes corresponding to different individual subjects. The dataset in [75] contains structural connectivity matrices of 43 healthy patients, divided in $N = 264$ large-scale regions, and allows to quantify the variability of simulated neural activity and the critical point. As we can see from Fig.3.8, the high fluctuations of individual behaviours in the not normalized case disappears using normalized connectomes with an almost complete collapse of the curves.

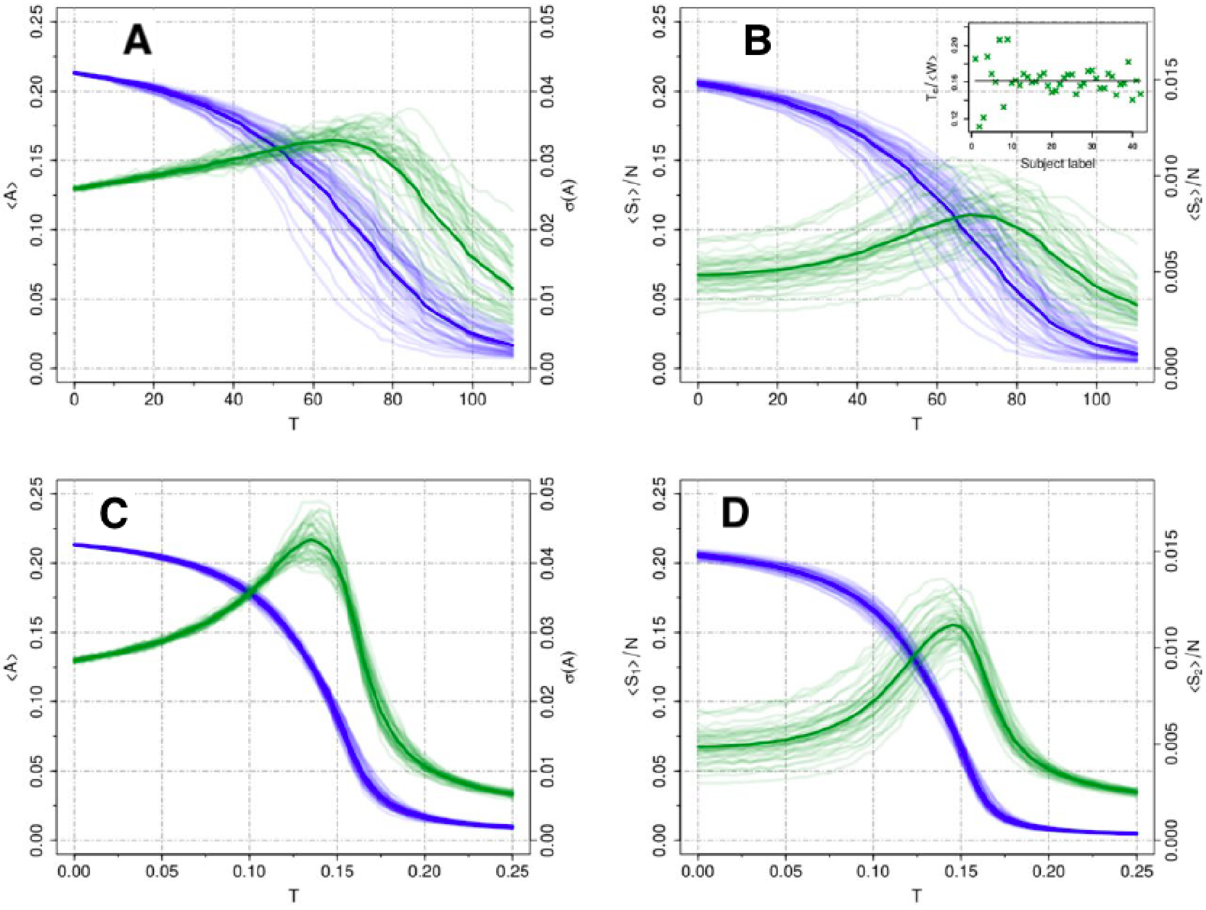

Figure 3.8: Criticality in HTC model dynamics is enhanced with homeostatic plasticity in individual connectomes from [75]. (a) Mean activity (*blue lines*) and variance (*green lines*) as a function of the threshold T for the non-normalized case. (b) First (*blue lines*) and second (*green lines*) largest cluster size as a function of the threshold T for the non-normalized case. (c,d) Same state variables but for the normalized case. We can notice a srong collapse of the curves. *Transparent curves* represent each individual; *Thicker curves* represent the group average. From [68].

This is a first insight on personalized brain modelling. In addition, these results suggest that not only the presence of interconnections between brain regions, but also the strengths of the various connections encoded in the weights of connectivity matrix play an important role on the dynamics, especially in the universality of the curves that is established with homeostatic normalization. We will investigate more in detail this universality in the following Chapter 4. Due to the importance of these results, in the continuation of the work we will always compare the effect of the normalization (Eq.3.7) in our simulations. In other words through the normalized HTC model it is possible to describe and compare the neural activity of individual brain dynamics based on real structural connectivity networks, as all the networks have the same critical point. These results provide unprecedented proofs of concept showing how personalized whole brain dynamical models poised at criticality can be used as biomarkers for individual neural activity.

3.3 Avalanches

Due to the fact that scale-free avalanches are the most appealing evidence of criticality in cortical activity, we explore their statistics in the dynamics of HTC model. How to define an avalanche is crucial and different methods are available in literature. Given the fact that for most combination of rates r_1 and r_2 the network is continuously active, the imposition of an *ad hoc* threshold is required to discriminate events of interest from silent phases. Therefore an avalanche is identified by the upwards and downwards crossing of the threshold by the network average activity. We highlight that *”this thresholding procedure is often deemed artificial because it introduces an additional parameter on which results depend. However, it is important to keep in mind that, when dealing with empirical data, the avalanche definition inevitably requires the introduction of a threshold... Usually the activity at each site is thresholded to define a local binary event”* [76].

In our case, instead, we have used a threshold based on the global activity. In particular, we have chosen the median of network activity as threshold θ, like previously done in [76]. Care should be taken not to confuse the threshold T, which is the control parameter of the HTC dynamics, with the threshold θ used to detect avalanches. A neuronal avalanche starts and ends when the signal of the average activity $A(t)$ of the network crosses θ. If the crossing points are situated at time t_i and t_f, its duration is simply $T = t_f - t_i$, while its size is defined as $s = \int_{t_i}^{t_f} d\tau[A(\tau) - \theta]$, i.e. the area above threshold (Fig.3.9).

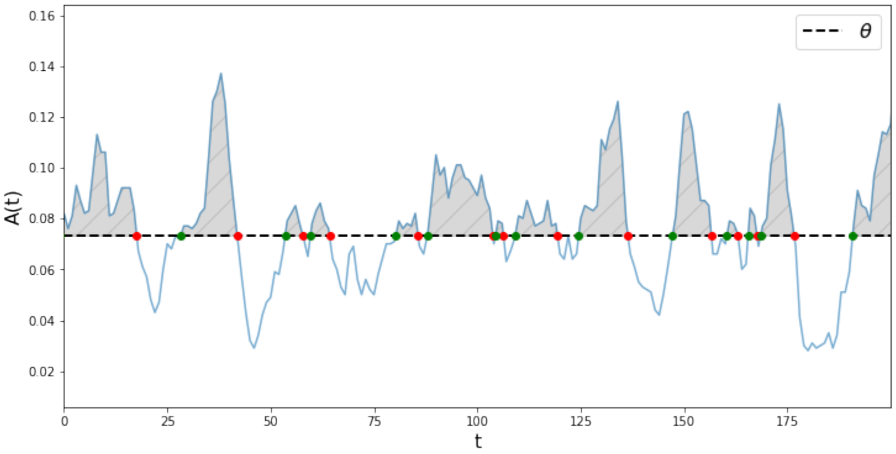

Figure 3.9: Example of avalanches in HTC model. Each avalanche start (*green dots*) and end (*red dots*) when the average activity cross the threshold θ. The avalanche duration is the time that the activity stay above θ. The avalanche size is the area of the activity above the threshold (*shaded area*).

The results of the simulation over the human connectome are reported in Fig.3.10. What

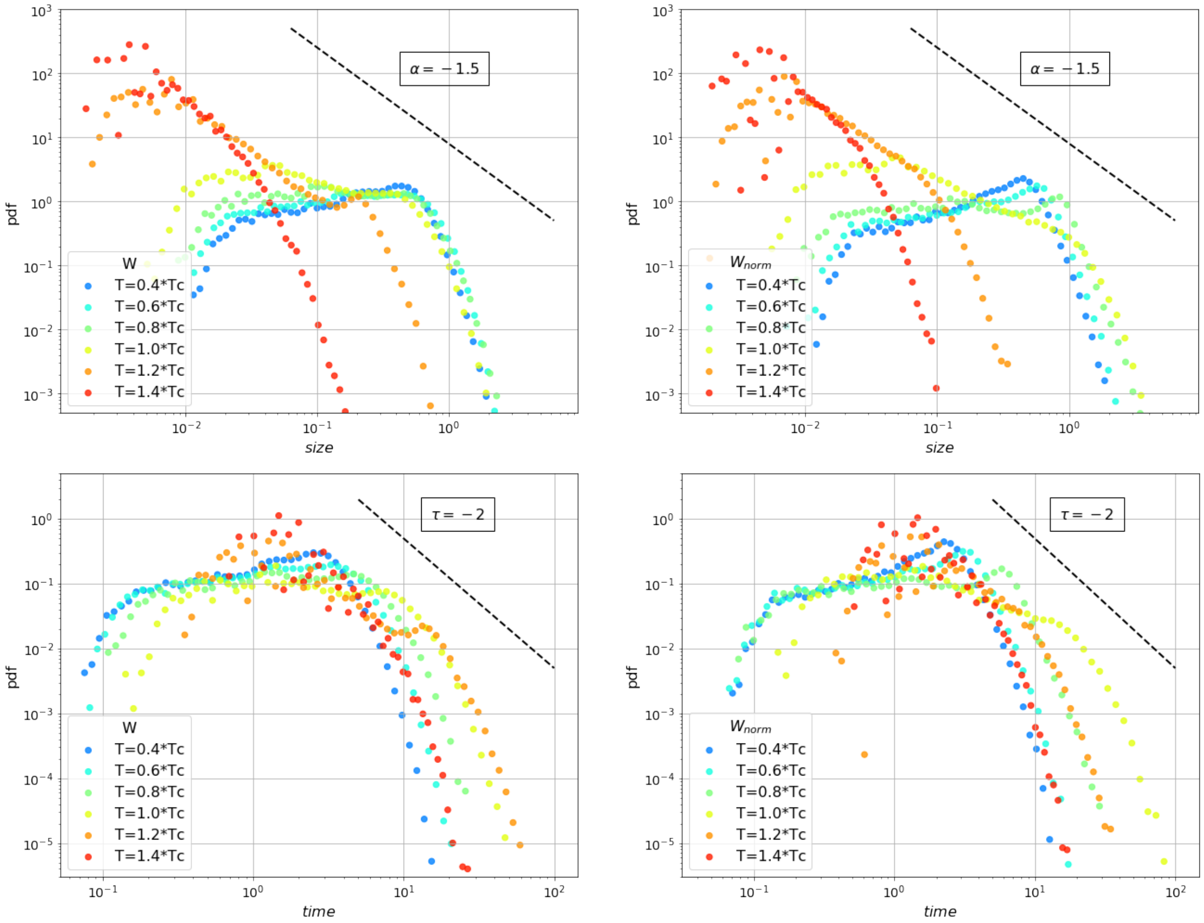

Figure 3.10: Distribution of avalanches in HTC model for different threshold T. *Top panel*, size distribution. *Bottom panel*, time distribution. *Left column*, non-normalized connectome. *Right column*, normalized connectome. *Dashed line*, power-law with classical exponents for neuronal avalanches, respectively $\alpha = -1.5$ and $\tau = -2$, for visual comparison. All the plots are in log-log scale and the distributions are evaluated with logarithmic bins.

we can observe in the statistics of avalanche sizes is an initial trend that seems almost linear in log-log scale for small sizes, ending in an exponential truncation for larger sizes. The steepness of the power-law trend depends directly on the threshold: it is quite flat for low value of T and it decreases as the threshold increases. This is something that we would have expected, since for large threshold T it is more difficult for the system to spread the activity between nodes, thus making hard to have extensive and very long-lasting avalanches.

We have discussed in Sec.2.1 how experimental data highlights scale-free patterns in neuronal avalanches. Unfortunately, the slope of the power-law trend are very far from the expected exponents. Only in the supercritical region the avalanches follows a scale-free trend close to the expected ones (*dashed lines* in Fig.3.10), but in a very limited range around one order of magnitude. Moreover, the depiction in the distribution of avalanche lifetimes is even more blurred. For these reasons, avalanches does not seem to be a relevant observable for the investigation of criticality in HTC model.

3.3.1 Causal avalanches

Because of the limitations named above, we explore other ways to define an avalanche. If we look at a microscopic scale, the spontaneous activation of a node marks the birth of a new event that triggers a cascade of activity. We can identify every individual event as a new avalanche, which will expand by inducing activation in neighbouring nodes. Each induced activation is assigned to the avalanche that caused it, therefore they were named *causal avalanches* [77]. So we obtain an alternative scenario in which diverse avalanches can coexist simultaneously (Fig.3.11).

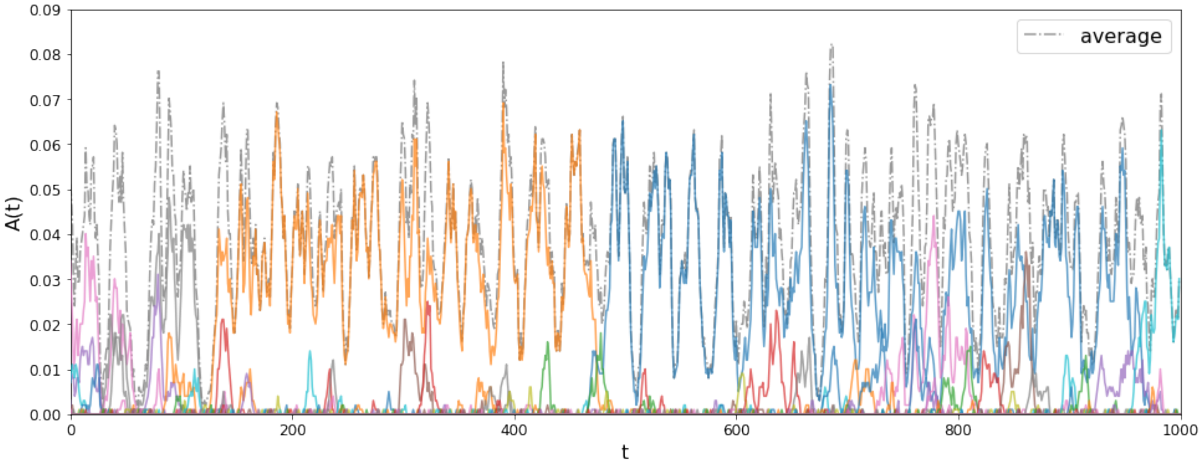

Figure 3.11: Example of causal avalanches in HTC model. Each colored time series represent the activity of a single avalanche, i.e. the fraction of active nodes at a certain time t belonging to that avalanche. The global activity density is represented with the dashed gray line.

In biological neural tissue, a neuron integrates synaptic incoming signal to fire itself. Similarly in HTC model each node can activate due to the combined work of neighbouring sites: for this reason it may happen that more avalanches contribute to the spikes of the same node. In order to assign the new activation to an avalanche, a competition principle has to be introduced. Given a certain node i that fires at a certain timestep, with probability r_1 it is a spontaneous activation, thereby with probability $1 - r_1$ it is an induced activation due to signals coming from neighbours j, each one contributing with a factor proportional to the connection strength W_{ij}. So we assign node i to the avalanche to which node j belongs with probability $\propto (1 - r_1)W_{ij}$. Thus an event of activity cannot be simultaneously part of more than one avalanche, having these to compete in order to propagate in the system. However, such choice is just a convention and other mechanisms may be considered, for instance avalanche may coalesce one with the other or intersect without competing.

A causal avalanche may eventually die out if it do not provokes any further activation. Therefore, differently from above case, there is no need to introduce any threshold to mark the end of an event of interest. We can compute again the statistics of lifetimes, i.e. the number of timesteps from the spontaneous activation to the avalanche extinction, and sizes, i.e. the total number of activations belonging to a considered avalanche.

Interestingly, the distributions follow a power-law trend regardless of the control parameter T (Fig.3.12). The only visible impact is on the cut-off that decreases as T increases. As previously, it is related to the growing difficulty for the network to spread activity

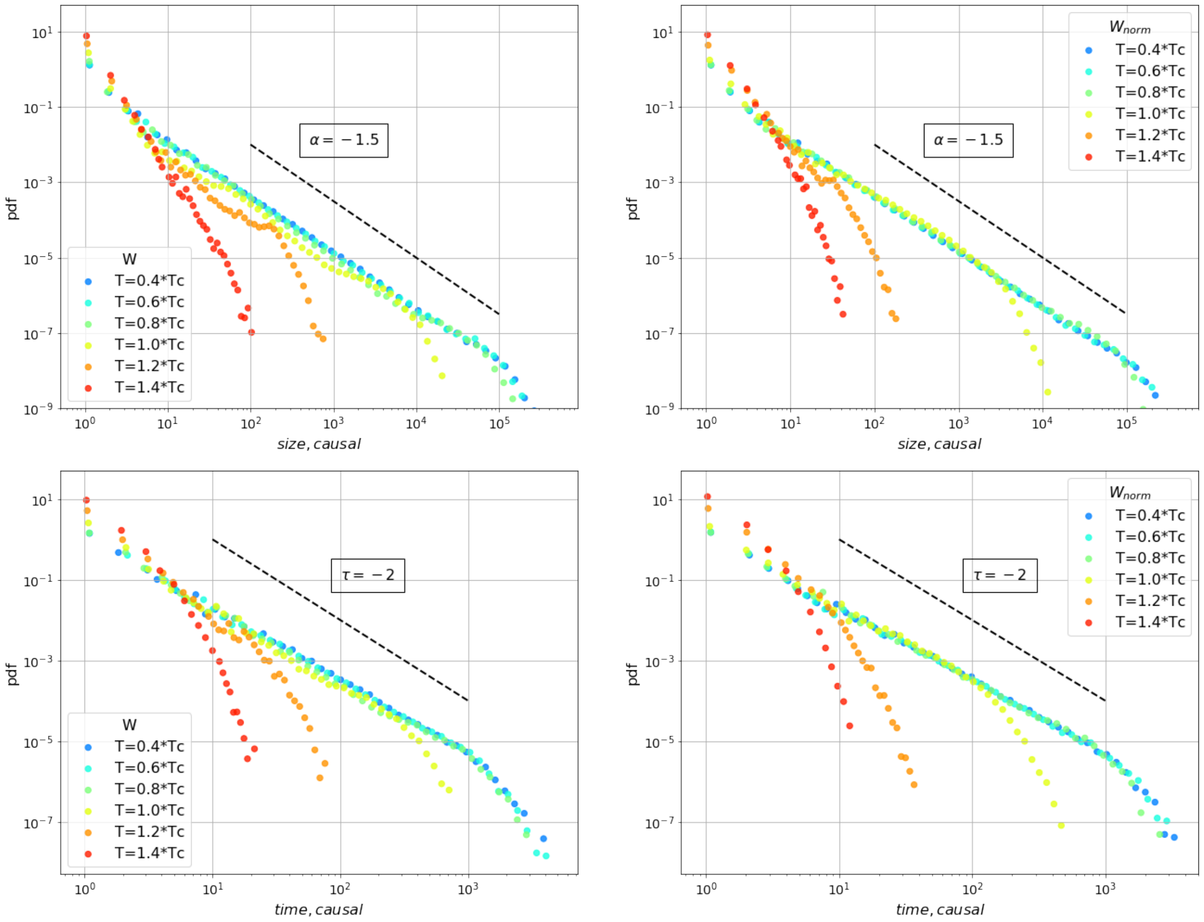

Figure 3.12: Distribution of causal avalanches in HTC model for different threshold T. *Top panel*, size distribution. *Bottom panel*, time distribution. *Left column*, non-normalized connectome. *Right column*, normalized connectome. *Dashed line*, power-law with classical exponents for neuronal avalanches, respectively $\alpha = -1.5$ and $\tau = -2$, for visual comparison. All the plots are in log-log scale and the distributions are evaluated with logarithmic bins.

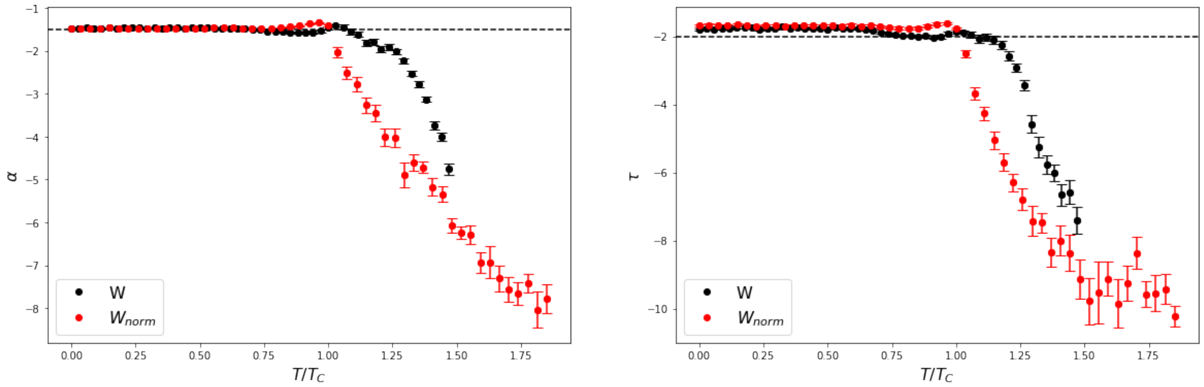

Figure 3.13: Scale-free exponents of causal avalanches from simulated data. *Left panel*, α coefficient for avalanche size. *Right panel*, τ coefficient for avalanche lifetime. *Dashed line*, classical exponents for neuronal avalanches, respectively $\alpha = -1.5$ and $\tau = -2$.

with higher threshold T. Moreover, the power-law exponents are almost close to the ones of experimental avalanches for all values of T in the supercritical region, i.e. $T < T_C$, and the critical point discriminates two phases, critical and non-critical causal avalanches (Fig.3.13). This may suggest that microscopic causal avalanches are always critical in that region of the control parameter. A similar results was obtained in [77], in which causal avalanches in an integrate-and-fire model and in a contact process were shown to be always critical and it is claimed to be due to the microscopic neutral dynamics [77]. Nevertheless, it is hard to claim that local dynamics in HTC model is neutral. This is something to be addressed in more detail in the future.

3.4 New evidence of criticality

Given the fact that criticality is not well define for finite-size system, we try to characterize the phase transition with other signatures of critical phase transitions, commonly used in other studies. We investigate the *Fisher information* and the *dynamic range* and we found that both maximize at T_C.

3.4.1 Fisher information

As we have already mentioned, physical systems are highly responsive and extremely sensitive to environmental changes nearby a critical transition. Response functions quantify the variation of a macroscopic variable of the system under the variation of an external parameter and diverges in presence of a critical point, where even a small change in the external parameter would be perceived and translated to relevant modifications in the order parameter.

Susceptibility is probably the most popular response function in magnetic medium and it is shown to be related to the amount of fluctuations in the magnetization. This measure can be generalized in an information-theoretic framework [19]. We can introduce an individual system or "agent" characterized by a probability $P_{int}(\mathbf{s}|\boldsymbol{\beta})$, depending on a set of internal parameters $\boldsymbol{\beta}$, whose scope is to adapt in response to stimulus from an environmental source $\boldsymbol{\alpha}$ by changing its internal state $\mathbf{s}$. The distribution of the agent can be parametrized in the following way:

$$P_{int}(\mathbf{s}|\boldsymbol{\beta}) = \frac{exp(-H_{int}(\mathbf{s}|\boldsymbol{\beta}))}{Z_{int}(\boldsymbol{\beta})} \tag{3.8}$$

The factor $Z_{int}(\boldsymbol{\beta})$ is defined by normalization condition, while the quantity H_{int} can be expressed as:

$$H_{int}(\mathbf{s}|\boldsymbol{\beta}) = \sum_{\mu=1}^{I} \beta_\mu \phi^\mu_{int}(\mathbf{s}) \tag{3.9}$$

where I is the number of parameters specifying the agent and $\phi^\mu(\mathbf{s})$ are suitable observables. The *Fisher information*:

$$\chi^{\mu\nu} = \left\langle \frac{\partial P(\cdot|\boldsymbol{\beta})}{\partial \beta_\mu} \frac{\partial P(\cdot|\boldsymbol{\beta})}{\partial \beta_\nu} \right\rangle_{\boldsymbol{\beta}} \tag{3.10}$$

quantifies the amount of information encoded in the state $\boldsymbol{s}$ about the unknown parameters $\boldsymbol{\beta}$ of a distribution that describe $\boldsymbol{s}$ itself and it is proven to correspond to the *generalized susceptibility*:

$$\chi^{\mu\nu} = -\frac{\partial}{\partial \beta_\mu} \langle \phi^\nu \rangle_{\boldsymbol{\beta}} = \langle \phi^\mu \phi^\nu \rangle_{\boldsymbol{\beta}} - \langle \phi^\mu \rangle_{\boldsymbol{\beta}} \langle \phi^\nu \rangle_{\boldsymbol{\beta}} \tag{3.11}$$

which is equal to the fluctuations of the observables ϕ^μ and diverges at the critical point in the limit $N \to \infty$ [19].

We compute the *Fisher information* in the HTC model from Eq.(3.11) as the covariance of the time series of the state variable between node i and node j:

$$\chi^{ij} = \frac{1}{t_s} \sum_{t}^{t_s} s_i(t) s_j(t) - \frac{1}{t_s^2} \sum_{t}^{t_s} s_i(t) \sum_{t}^{t_s} s_j(t) \tag{3.12}$$

averaged over all pairs of nodes and over each run:

$$\chi = \sum_{i \neq j} \chi^{ij} \tag{3.13}$$

As we can see from Fig.3.14, also the Fisher information peaks for intermediate value of threshold T. If the intrinsic neuronal activity is too sustained or too suppressed, the brain response to changes in the environment will be very dampened or even not perceived. Whereas at the edge of a phase transition between these two regimes, the divergence of the fluctuations in the average activity of the brain model amplifies the responsiveness of the system.

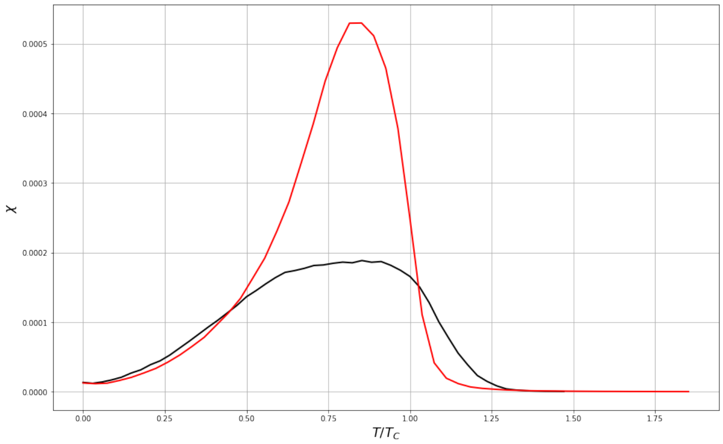

Figure 3.14: Fisher information or generalized susceptibility peak near critical point. Homeostatic plasticity (*red line*) amplifies the peak with respect to the original connectome (*black line*).

3.4.2 Dynamic range

Another quantity that characterize the ability of a system to discriminate a wide range of environmental stimuli is the *dynamic range*. In Sec.2.4 we have pointed out that dynamic range is defined as the ratio between the largest η_{high} and the smallest η_{low} stimulus, measured in dB, that results in perceptible variations of the response of the system:

$$\Delta = 10 \log(\frac{\eta_{high}}{\eta_{low}}) \tag{3.14}$$

In order to compute the dynamic range for HTC model, we simulate the dynamics for different values of r_1, which can be seen as the rate of induced activation from an external source. As could be easily expected, the average activity increases monotonically with the magnitude of the external stimulus (Fig.3.15, *top panels*), because it becomes more probable for a node to self-activate. The slope of the response curves is heavily influenced by the threshold: for low values of T, even negligible stimuli lead to an high activation, for high T a strong induced rate is necessary for having a non-zero activation of the network.

The stimulus interval in Eq.(3.14) is arbitrary. Typically, in literature it is standardly chosen as the range $[r_{0.1}, r_{0.9}]$ that lead to an average activation of 10% and 90% respectively, i.e. it corresponds to a response interval $[A_{0.1}, A_{0.9}]$ where:

$$A_x = A_{min} + x(A_{max} - A_{min}) \tag{3.15}$$

and A_{max}, A_{min} are the maximum and minimum average activity at a fixed threshold by varying r_1.

Figure 3.15 highlights a sharp peak in the dynamic range in correspondence of the critical point. This is a further confirmation that the neural activity of the human brain involved in capturing and elaborating information from environmental stimuli has the maximal sensitivity at criticality.

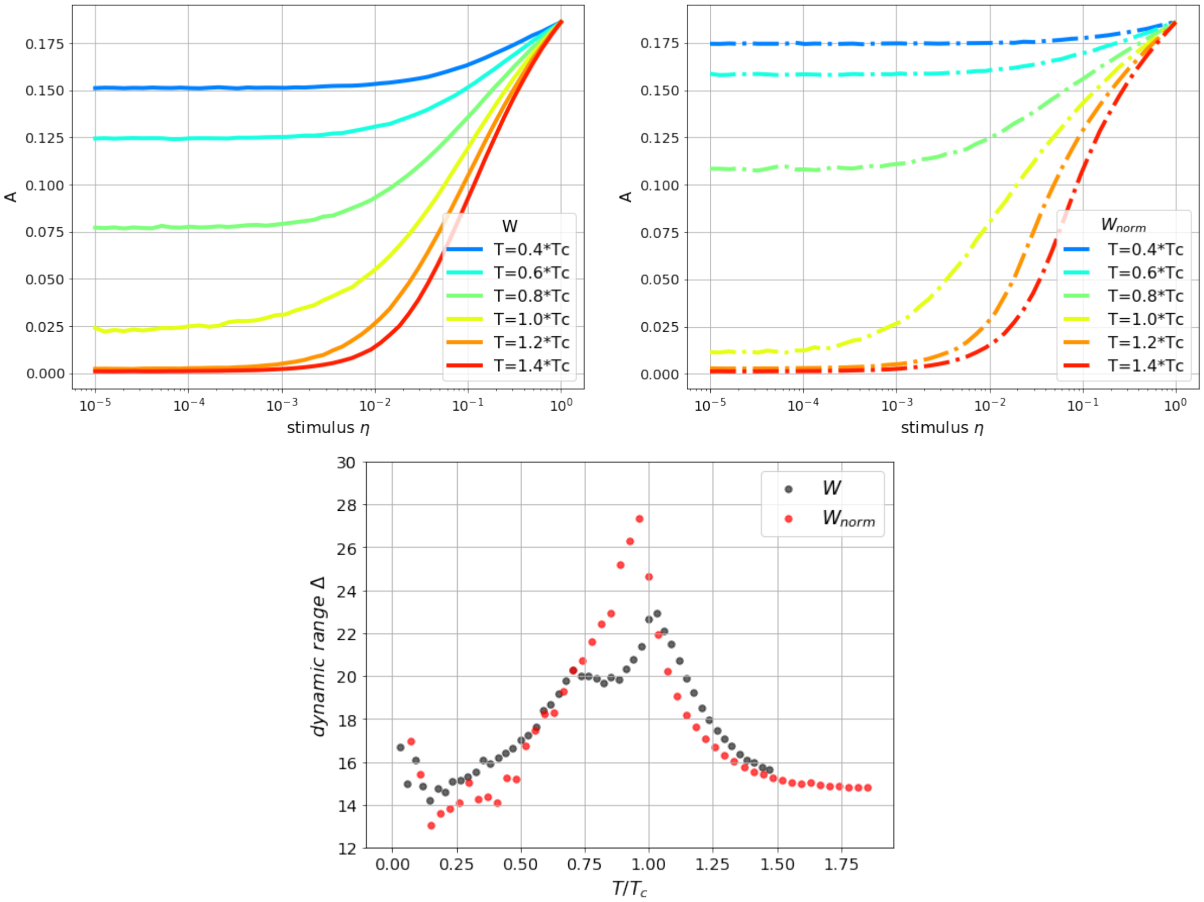

Figure 3.15: Dynamic range is maximized at T_C. (*Top panels*), response curves, i.e. mean activity versus stimulus rate, for some values of threshold T in the un-normalized (*left*) and normalized (*right*) case. (*Bottom panel*), dynamic range as a function of the threshold T displays a peak at the critical point, which is amplified by homeostatic plasticity (*red dots*).

Chapter 4

Structure-function relation in a stochastic whole-brain model at criticality

In Sec.1.3 we have seen how the underlying architecture strongly determines the overall functioning of the human brain, although not completely. Likewise, from a theoretical perspective, the structure of a network is very often crucial in the description of a model. Indeed, in Statistical Mechanics the critical exponents usually vary depending on the dimension and the particular topology. This means that the topology may strongly affect the universality class of a model.

In this Chapter we investigate in more detail the role of the topology in the HTC model, either in a theoretical framework (Sec.4.1) and by simulating the HTC model on top of random matrices (Sec.4.2).

4.1 Scaling of the critical point in the mean-field approximation

In the following Sec.4.2 we are going to highlight how the underlying graph strongly affect the phase transition in the HTC model. For this reason, it is usually very hard to obtain a general mathematical description that is valid for different geometries. Nevertheless, we propose a theoretical formulation of the model in a simplified case, in which every node is structurally connected to each other, namely in the *mean-field approximation*. Moreover, we assume that the weights are all equal. From these hypotheses we were able to describe the time evolution of the system by means of a *master equation*. The full derivation is reported in Appendix B.

The other important result that we obtain is that in the limit of large number of neurons in the network, i.e. in the thermodynamic limit $N \to \infty$, there are two global and stable equilibria, that we called x_+ and x_-, respectively for a high and low level of global activity, that even coexist for an intermediate range of threshold T delimited by T_+ and T_-.

The thermodynamic limit is clearly a theoretical operation. In reality, the human connectomes are limited in size. In order to test the validity of our findings, we simulate the HTC model over fully-connected networks with finite dimension. However, in this case the clusters of co-activation are no longer a relevant observables, due to the fact that nodes are always structurally connected, thus when activated they belong to the same unique cluster. For this reason, we will focus only on the average global activity as order parameter and its fluctuations. In the following simulations we fixed parameters $r_1 = 10^{-1}$ and $r_2 = 10^{-1}$ for visualization purposes, otherwise T_- would have been too small, but the results were found consistent also for other combinations of parameters, including the ones used for the simulations reported in Chapter 3.

As we can notice from Fig.4.1, the average activity almost perfectly match the theoretical expectations of x_+ and x_- reported in Eq.(B.15) and Eq.(B.20). In the intermediate range of threshold marked by T_+ and T_- (see Eq.(B.16) and Eq.(B.21)), there is a overall decrease in the global level of activation in the network. Such transition is also highlighted by a peak in the variance $\sigma(A)$, similarly to what we already found with the human connectome.

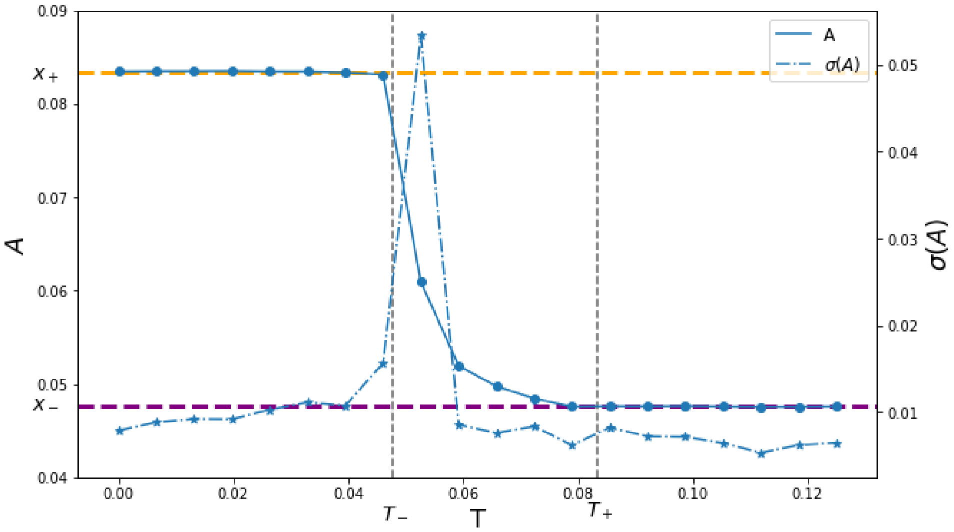

Figure 4.1: Dynamics of HTC model over a fully-connected finite-size matrix ($N = 10^5$) is consistent with the theoretical predictions of mean-field approximation in the thermodynamic limit. The average activity in the sub- and super-critical region almost perfectly collapse on the expected values Eq.(B.15) (*orange line*) and Eq.(B.20) (*purple line*). In the coexistance region, there is a decrease of A, while the variance $\sigma(A)$ display a sharp peak that identifies the phase transition.

However, the peak does not correspond to any of the two relevant thresholds T_+ and T_-. In order to further understand the role of these two points, we perform a finite-size scaling of the critical point identified in the peak of the variance. As shown in Fig.4.2, the peak of $\sigma(A)$ shifts towards T_- as the size of the system increases. Interestingly, it seems to scale exponentially towards T_- as a function of the size N (Fig.4.3): indeed in the limit $N \to \infty$ the interpolation reaches a value very close to the analytical expectation of T_-.

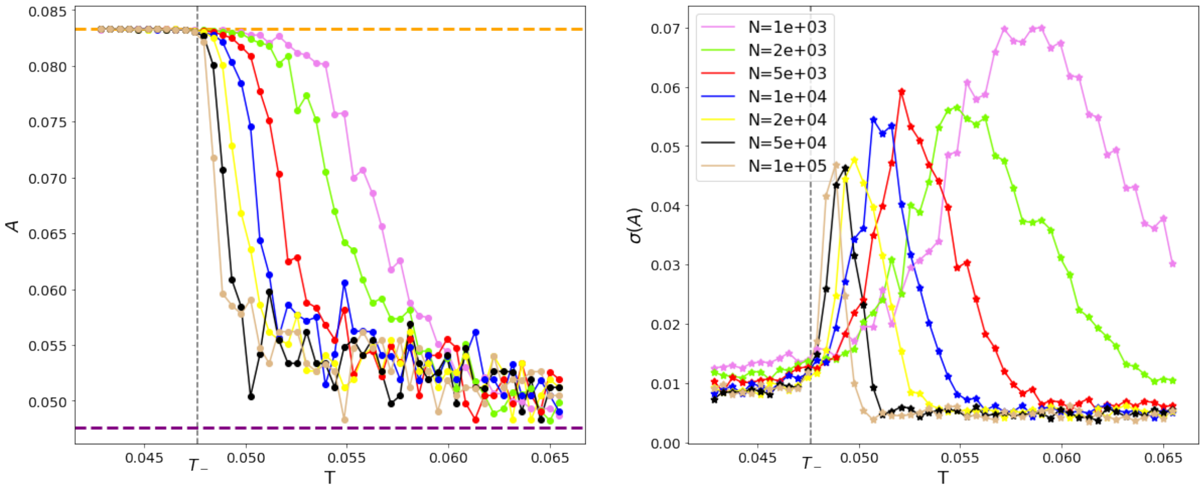

Figure 4.2: Critical point of HTC model over fully-connected networks shifts towards T_- as the size of the network N increases. *Left panel*, average network activity. *Right panel*, fluctuations of network activity $\sigma(A)$. Each colored line correspond to a different size N. *Dashed lines*, analytical values of T_+ (*orange*) and T_+(*purple*).

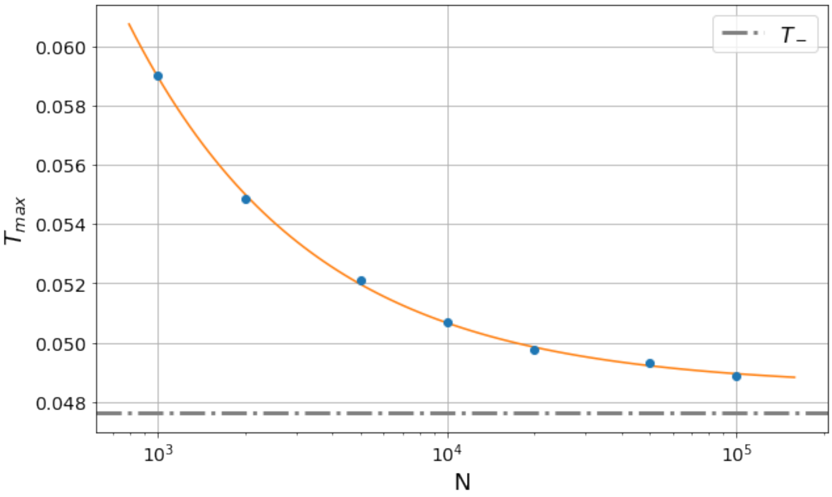

Figure 4.3: Scaling of the peak of $\sigma(A)$ as a function of the system size N in fully-connected networks. *Orange line*, interpolation with an exponential function of the type $T_{max} = ke^{-\mu N} + c$. To be noted that the coefficient $c = 0.0499$ has a value close to the theoretical expectation of $T_- = 0.0476$.

4.1.1 Adding random noise

A non-trivial topology, like the human connectome, introduces a spatial disorder in the system and clearly alters the symmetry of the dynamics, since a node is no longer connected to each other, but only to a bunch of them. The lack of some edges somewhat affects the activation of neurons in the same way that internal noise would do. Such consideration prompted us to check what happens if we alter the state variable of a neuron $s_i(t)$ by injecting a random noise:

$$s_i(t) \rightarrow s_i(t) + k \cdot \xi_i \tag{4.1}$$

where ξ_i is a random variable uniformly distributed $\xi_i \sim U(-1, 1)$ and k is the strength of the noise. Therefore, the state variable of each neuron is no longer binary, only active

(1) or not (0), but it brings some additional informations.

As the strength of the noise increases, the peak of $\sigma(A)$ becomes more smeared and less defined (Fig.4.4). In addition, it drifts away from T_- (Fig.4.5).

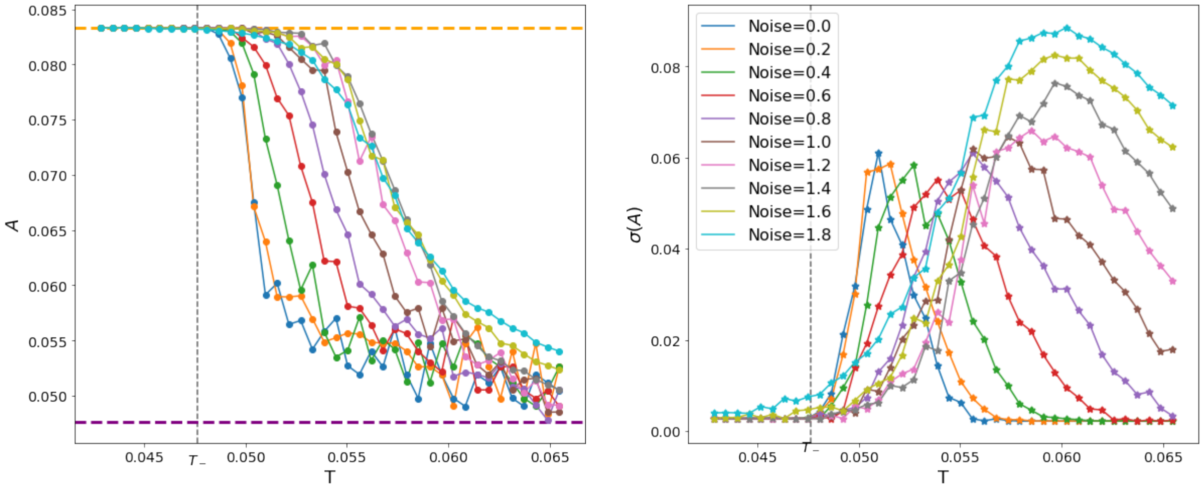

Figure 4.4: Critical point of HTC model over fully-connected networks drifts away from T_- as the strength of the internal noise k increases. *Left panel*, average network activity. *Right panel*, fluctuations of network activity $\sigma(A)$. Each colored line correspond to a different noise stregth k. *Dashed lines*, analytical values of T_+ (*orange*) and T_+(*purple*).

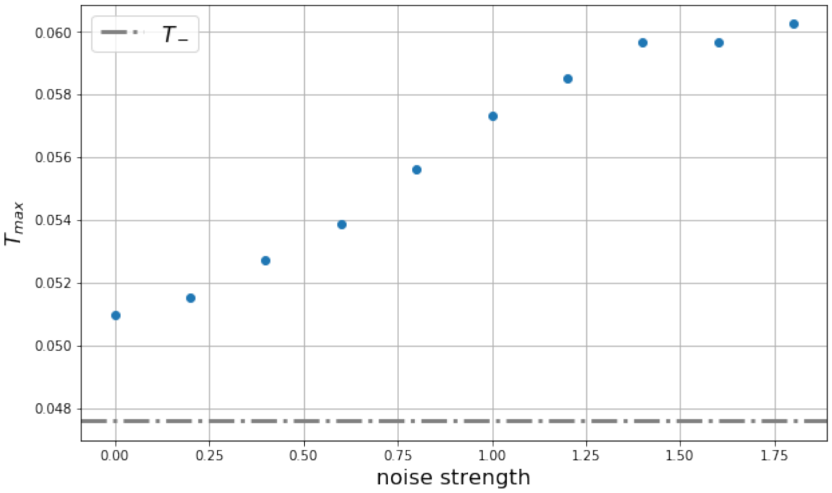

Figure 4.5: Scaling of the peak of $\sigma(A)$ as a function of noise strength in a fully-connected network of size $N = 10^4$.

4.2 HTC model with synthetic connectomes: the effect of connectivity

The connectome used for the previous simulation is a matrix with fixed structural properties, therefore it does not allow to determine to what extent some feature of the underlying topology, like the connectance or the presence of hubs, affect the dynamics of HTC model. In order to investigate the role of the topology in the phase transition, we simulate the model on top of architectures generated from some of the common ensambles of network structure: random graphs (Sec.A.5.1), Watts-Strogatz small-world graphs (Sec.A.5.2), and Barabási scale-free graphs (Sec.A.5.3).

More in detail, for each run we generate $M = 50$ different realizations of a particular type of graph with a defined average degree $\langle k \rangle$. In the case of small-world graphs and Barabási graphs we fixed the probability of rewiring at $p = 0.5$. To mimic the weights distribution of the human connectome, the weights of the adjacency matrices were drawn from a power-law distribution with exponent $\lambda = -1.5$, a value that is fitted to the empirical weight distribution [13]. In addition, we keep only connected matrices, otherwise we would have many subnetworks that do not interact in the spreading of the activation, which is something that does not occur in the human brain. The size of all the networks was fixed to $N = 800$, that is close to the size of the connectome [13] used in Chapter 3.

4.2.1 Dynamical regimes

The first interesting result is that HTC model ranges different dynamical regimes as we vary the overall connectivity of the architectures. Such observation was already presented in [78] for small-world graphs, but we further extend it to other class of networks. As we can notice from Fig.4.6, at low average degree $\langle k \rangle$, the usual peak in $\sigma(A)$ and S_2 is barely visible, if not completely absent, with a monotonic decrease of the curves. Thus, for such level of connectivity the dynamics is characterized by few small and uncorrelated clusters and an overall activity that is not well balanced in the network for any value of threshold T. Moreover, this regime resembles the so-defined *segregated regime* previously described in [79].

Increasing the value of $\langle k \rangle$, the model dynamics becomes similar to the second-order phase transition already observed in Chapter 3 with the simulation over the human connectome. In particular, we observe a critical threshold T_C in the peak of $\sigma(A)$ and S_2. Therefore, the system develops long-range clusters of simultaneously active nodes that resembles the behaviour of brain RSN.

For large enough values of $\langle k \rangle$ we encounter a different type of transition: both the order parameters A, S_1 and the fluctuations measures $\sigma(A)$, S_2 exhibit an apparently discontinuous behaviour at the transition point.

This is a first insight on how the overall large-scale activity depend on the topological details of the underlying structural network [78]. These results shows that patterns exhibited in brain RSN need certain minimum of connectivity level: for relatively low level of $\langle k \rangle$ the neuronal activity is too segregated, while in the other extreme the activity is too integrated. From a neuroscientific point of view "*a minimum of connectivity needs to be predetermined (perhaps via evolution) in order for the dynamics to achieve the dynamical features of criticality (via modulation of excitability or threshold). On the other hand,* *the discontinuous percolation that appears only for extremely connected networks, might constitute pathological conditions observed in real nervous systems*" [78].

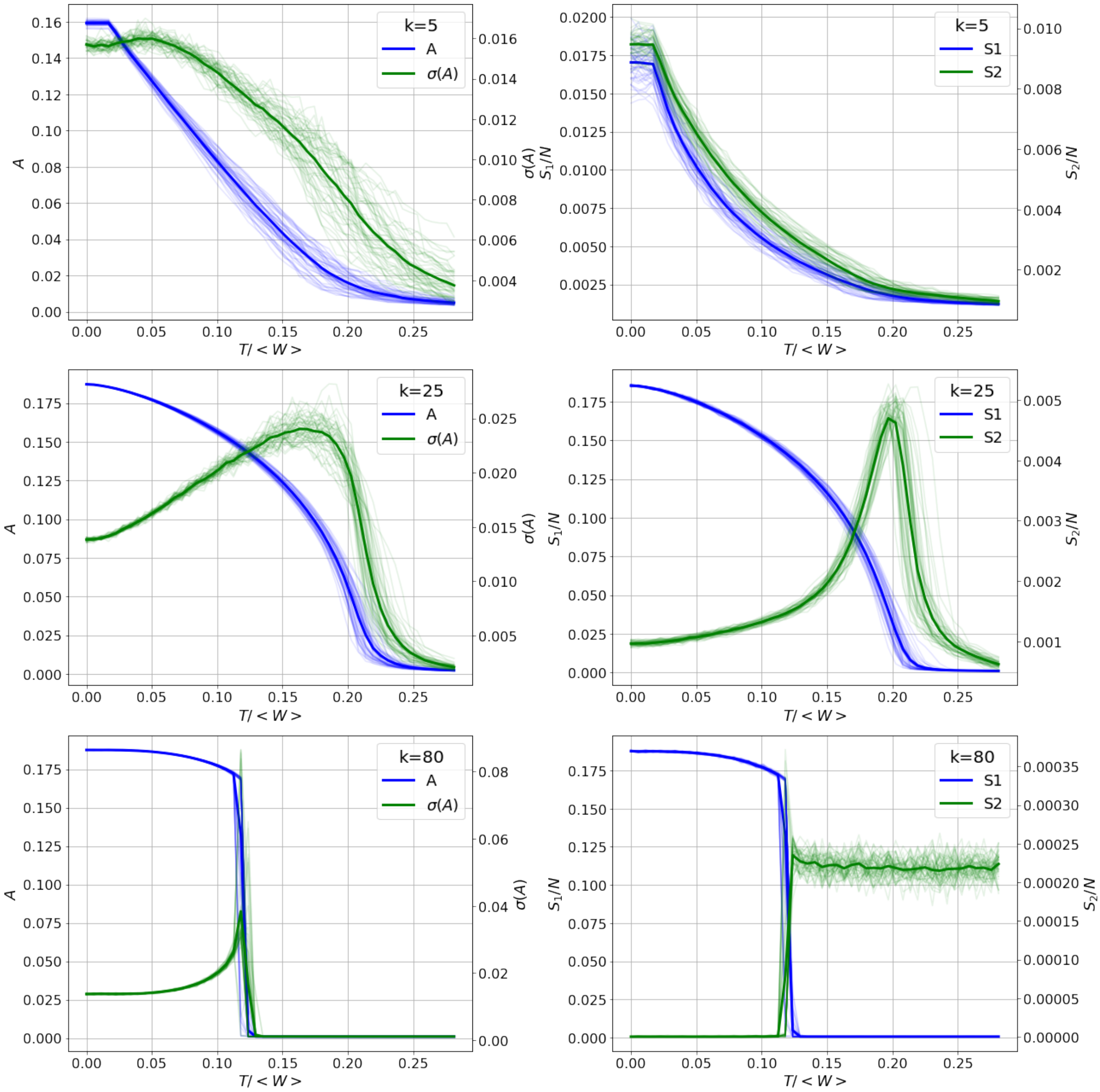

Figure 4.6: HTC model span different dynamical regimes as the overall connectivity of the network varies. Reults obtained with random networks, but are qualitatively similar also for small-world graph and Barabási graphs. *Solid line*, average over $M = 50$ different realizations of the network, displayed with *dashed lines*.

4.2.2 Effect of homeostatic plasticity

Then we try to investigate the effect of the homeostatic normalization Eq.(3.7) in the different class of networks. In Figure 4.7 and Figure 4.8 we compare respectively the average network activity with its fluctuations and the average cluster sizes in topologies with the same average degree $\langle k \rangle$.

What we can easily notice is a strong increase in both peaks of $\sigma(A)$ and S_2 by means of the homeostatic principle. The behaviour is quite similar for random and small-world graph, while such peak rise is very pronounced in Barabási networks. This effect can be easily understood if we focus on the purpose of the homeostatic normalization: it was introduce to regulate network excitability by ensuring that each node has a similar contribution to the overall activity, thus mitigating the role of hubs that are a peculiarity in scale-free networks (see Sec.A.5.3).

Moreover, another visible effect can be seen in the variability between different realization of the same network, that is softened with the homeostatic normalization. All the curves in Fig.4.7 and Fig.4.8 with non-normalized matrices (*left columns*) are quite blurred, while the peaks seems more consistent in the normalized case (*right columns*).

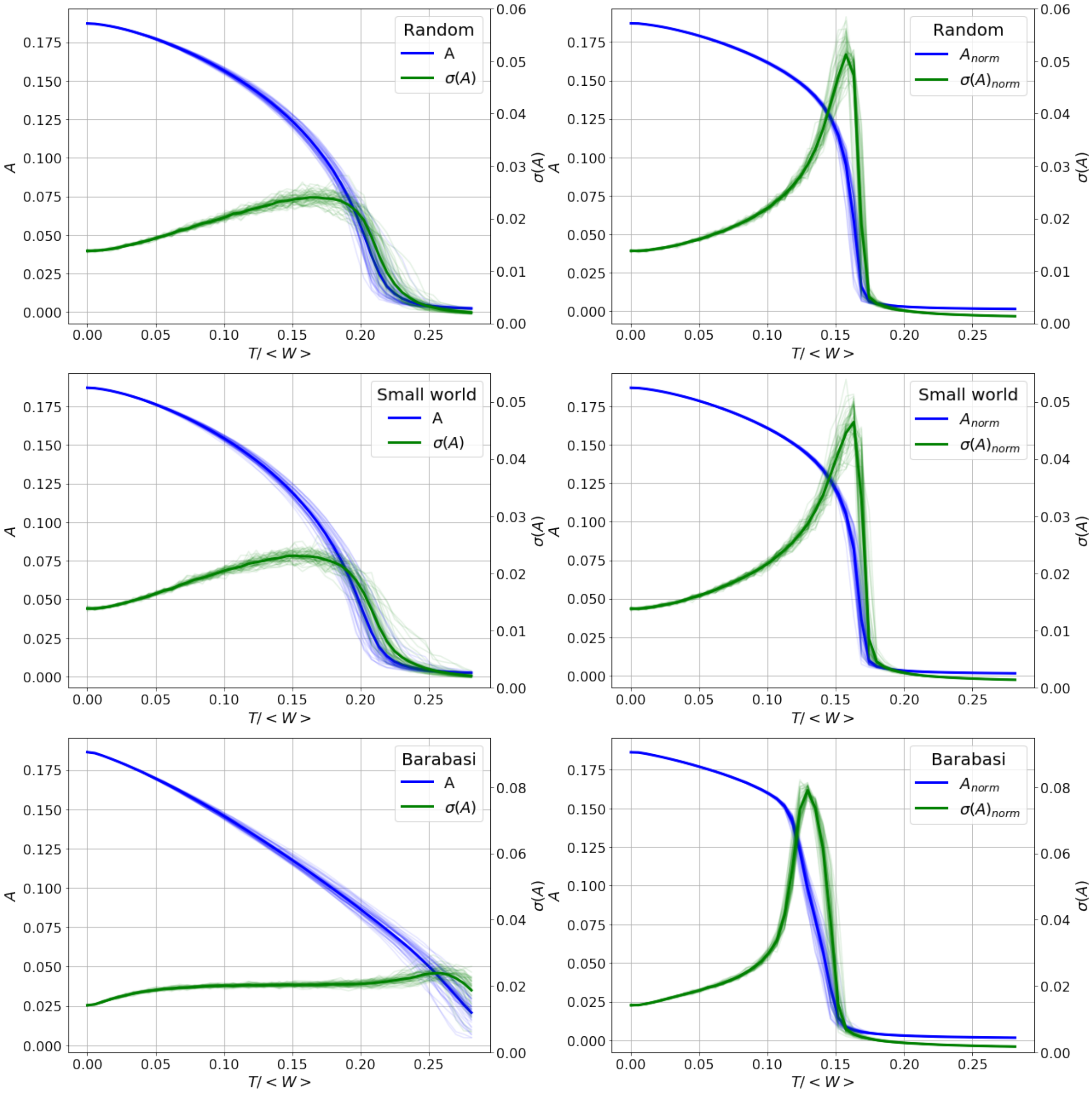

Figure 4.7: Effect of homeostatic normalization on the average activity and the fluctuations for different type of networks with the same average degree $\langle k \rangle = 25$. *Left column*, non-normalized case. *Right column*, normalized case.

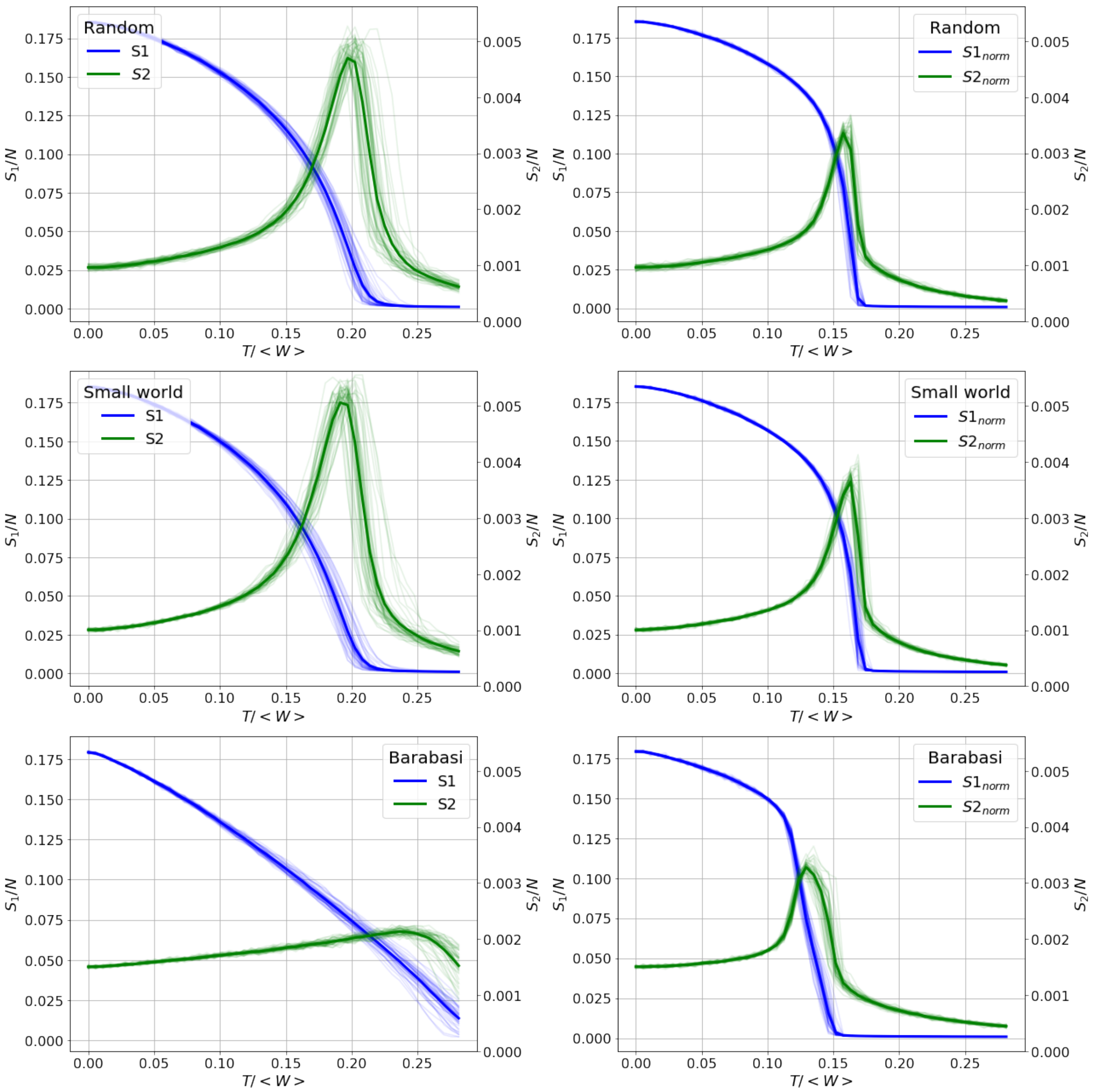

Figure 4.8: Effect of homeostatic normalization on the average cluster sizes for different type of networks with the same average degree $\langle k \rangle = 25$. *Left column*, non-normalized case. *Right column*, normalized case.

A further analysis that can be conducted concerns the critical point T_C. In Figure 4.9 we display how the values of the critical point, estimated as the peak in the second cluster size S_2, the fluctuations in the network activity $\sigma(A)$, and the generalized susceptibility χ, varies as we change the overall level of connectivity. It seems that for all the three measures at low connectivity the critical threshold T_C initially shifts from small to larger values and than saturates for larger $\langle k \rangle$. Furthermore, also in this simulations the variability of the critical point is attenuated thanks to the homeostatic normalization, since for all the different definition provide much closer estimates, thus more consistent (Fig.4.10).

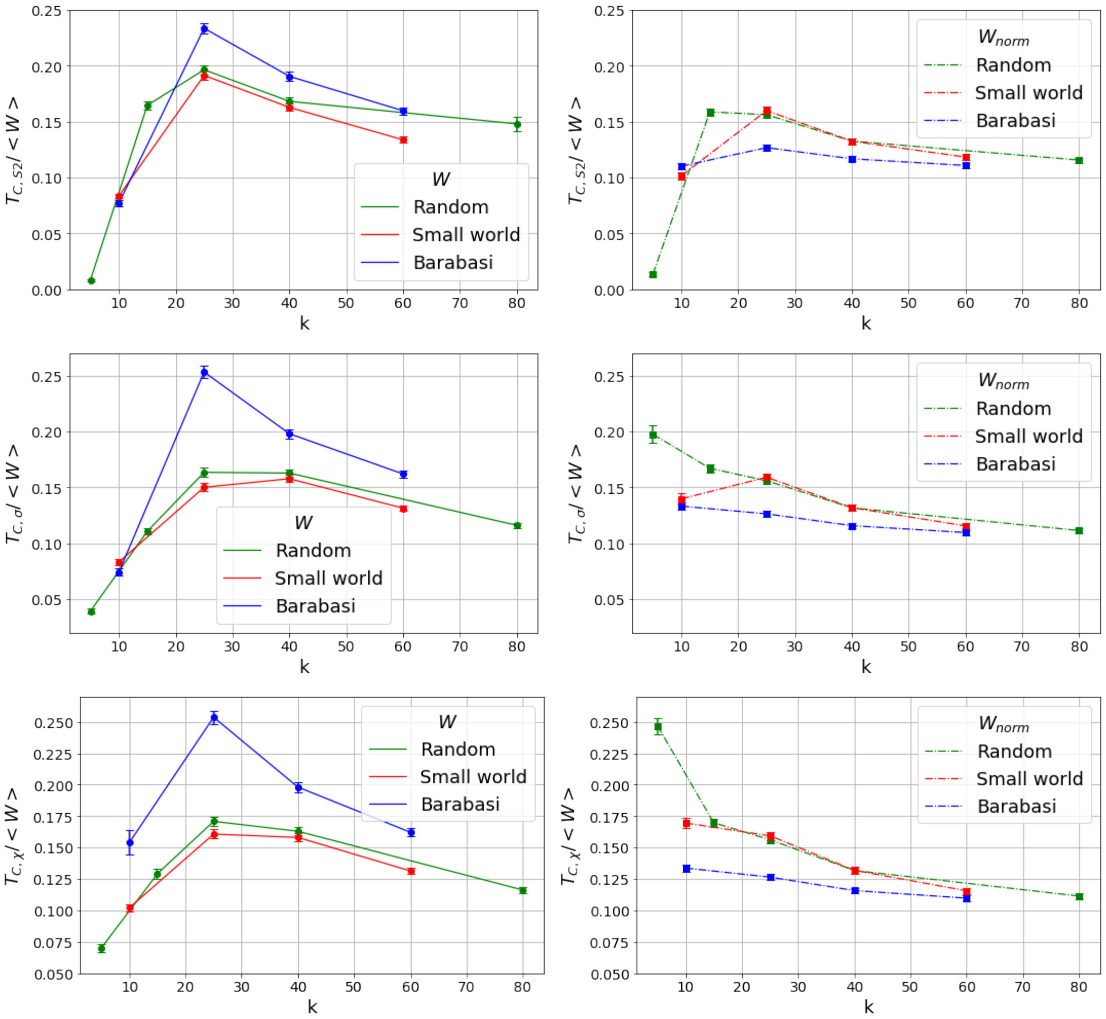

Figure 4.9: Shift of the critical point T_C as the average degree $\langle k \rangle$ varies. The critical threshold is identified as the peak in: the second cluster size S_2 (*top row*); the fluctuations in the network activity $\sigma(A)$ (*middle row*); the generalized susceptibility χ (*bottom row*). *Left column*, non-normalized matrices. *Right column*, normalized matrices.

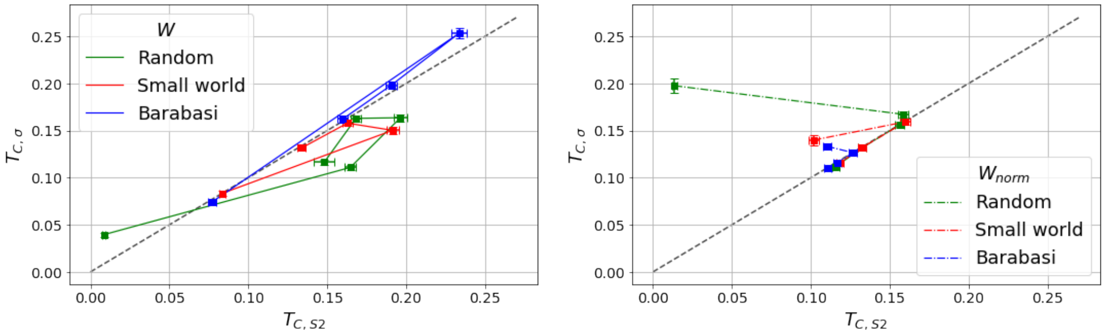

Figure 4.10: Peak of S_2 versus peak of $\sigma(A)$ for the different topologies. The introduction of the homeostatic normalization (*right panel*) seems to generally bring the two estimates of the critical point closer togheter (i.e. close to the bisector *dashed line*), while in the non-normalized case (*left panel*) there is much more variability.

4.2.3 Constant weights

The dynamics of the HTC model is not only influenced by the presence or absence of connections, but also by the weight associated with them, which may partly cover the true effect of the topology in the dynamics. To overcome this issue, we simulate the HTC model over different topologies but with constant weights over all the networks.

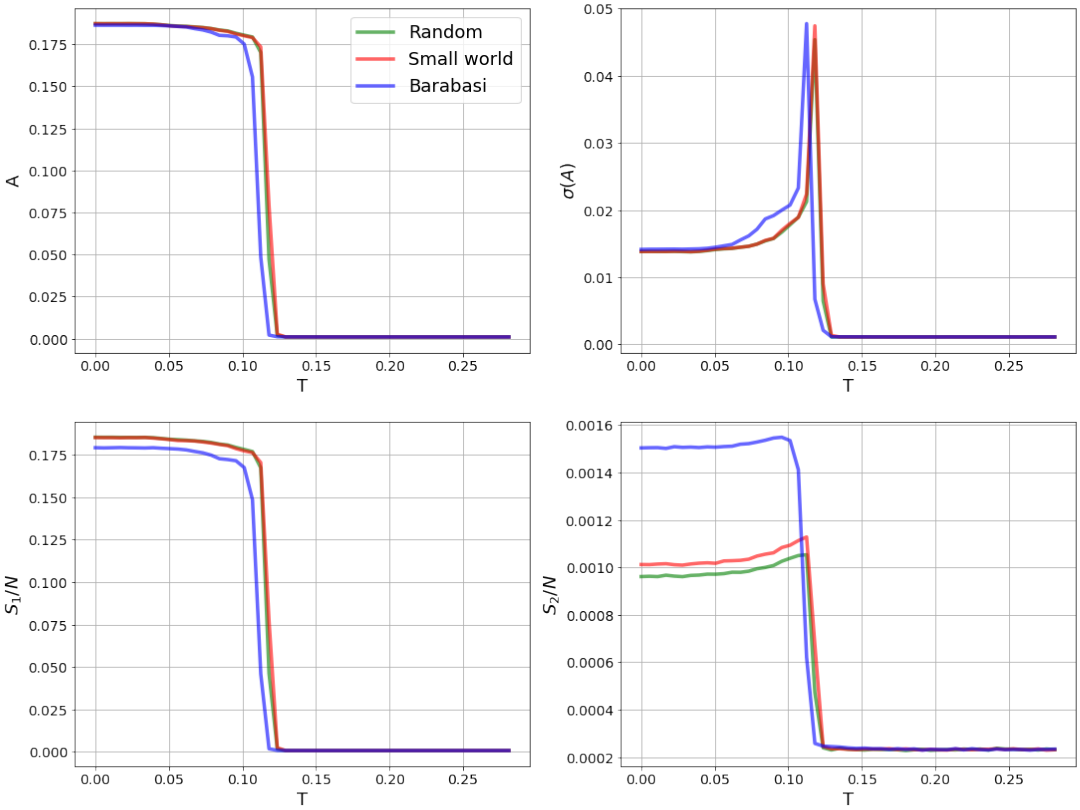

Figure 4.11: Simulation of HTC model over networks with constant weights. These results are obtained with the homeostatic normalizazion for topologies with $\langle k \rangle = 25$. Each curve represents the average over $M = 50$ different realizations of the networks.

The results of the simulations are reported in Figure 4.11. The order parameters display a sharp transition between the super-critical and a sub-critical phase in correspondence of a critical threshold T_C that can be identified in a sharp peak of $\sigma(A)$. However, a peak in the second cluster size S_2 is barely visible and the curve display a discontinuous jump, resembling more a first-order transtion rather than a critical ones.

We can further understand the effect of the weights by comparing such simulations to the previous results reported in Figure 4.7 and Figure 4.8 where we drawn the weights from a power-law distribution, since we have fixed the same average degree $\langle k \rangle$. The introduction of heterogeneous weights seems to smooth out the transition over a broader range of parameters and to give rise to a peak in the second cluster size. This is, nevertheless, a non-trivial result that calls for deeper analyses and investigations.

4.2.4 Finite size scaling

The use of generated topologies allows us to perform a finite-size scaling of the observables to hopefully provide a more robust characterization of criticality. Indeed, the human connectome [13] has a fixed size, thus prevent us from testing any finite-size effects. We perform some simulations of HTC model over different topologies by fixing the average degree $\langle k \rangle$ and varying the network size N.

In Figure 4.12 and Figure 4.13 we report the behaviour of the activity, while in Figure 4.14 the trend of the second cluster size. First of all, we can notice that the behaviour of the order parameter is quite similar for different sizes, thus not influenced by the changing of network size N. On the other hand, the height of the peak of the second cluster size S_2 keeps increasing with N: such result seems foreseeable, since in larger networks it becomes more probable to give rise to large connected clusters of activiation. The opposite happens for the peak of $\sigma(A)$ that decreases with N. Such fact can be explained in this way: for network with very small sizes, the role of fluctuations is prominent.

In [78] it was discovered that the largest value of the second cluster size S_2 in small-world graphs follows a power-law trend as a function of the network size. In that work, the critical exponent was consistent with the theoretical critical exponents of the mean-field percolation universality class, that scales with the system size as:

$$S_{2,max} \sim N^{d_f/d} \tag{4.2}$$

where d is the effective dimension of the system and d_f is the fractal dimension of the percolating cluster [71]. Since $d = 6$ and $d_f = 4$, the expected exponents is $d_f/d = 2/3$. Also in our data we recover such power-law scaling of $S_{2,max}$ not only for small-world graphs but also for random graphs and Barabási graphs. However, the scaling exponents are close but not consistent with the mean-field percolation exponent (around 0.72 for random and small-world graphs, 0.5 for Barabási graphs). Nevertheless, in our opinion it seems hard to claim that the HTC model should belong to the same universality class of the mean-field percolation, as it does not display any absorbing state, and, moreover, its dynamics is affected by non-trivial topology with relatively sparse connectivity and power-law distributed weights, i.e. very far from a lattice topology.

Finally, still in [78], the researchers found that also not only the average degree $\langle k \rangle$, but also the rewiring probability influenced the dynamical regime (Fig.4.16). At low $\langle k \rangle$, the emergence of a critical transition is favoured by an increased rewiring probability π, most likely because it is linked to a decreased average path legth. Instead for large $\langle k \rangle$ a large π transforms the transition from a second-order to a discontinuous ones.

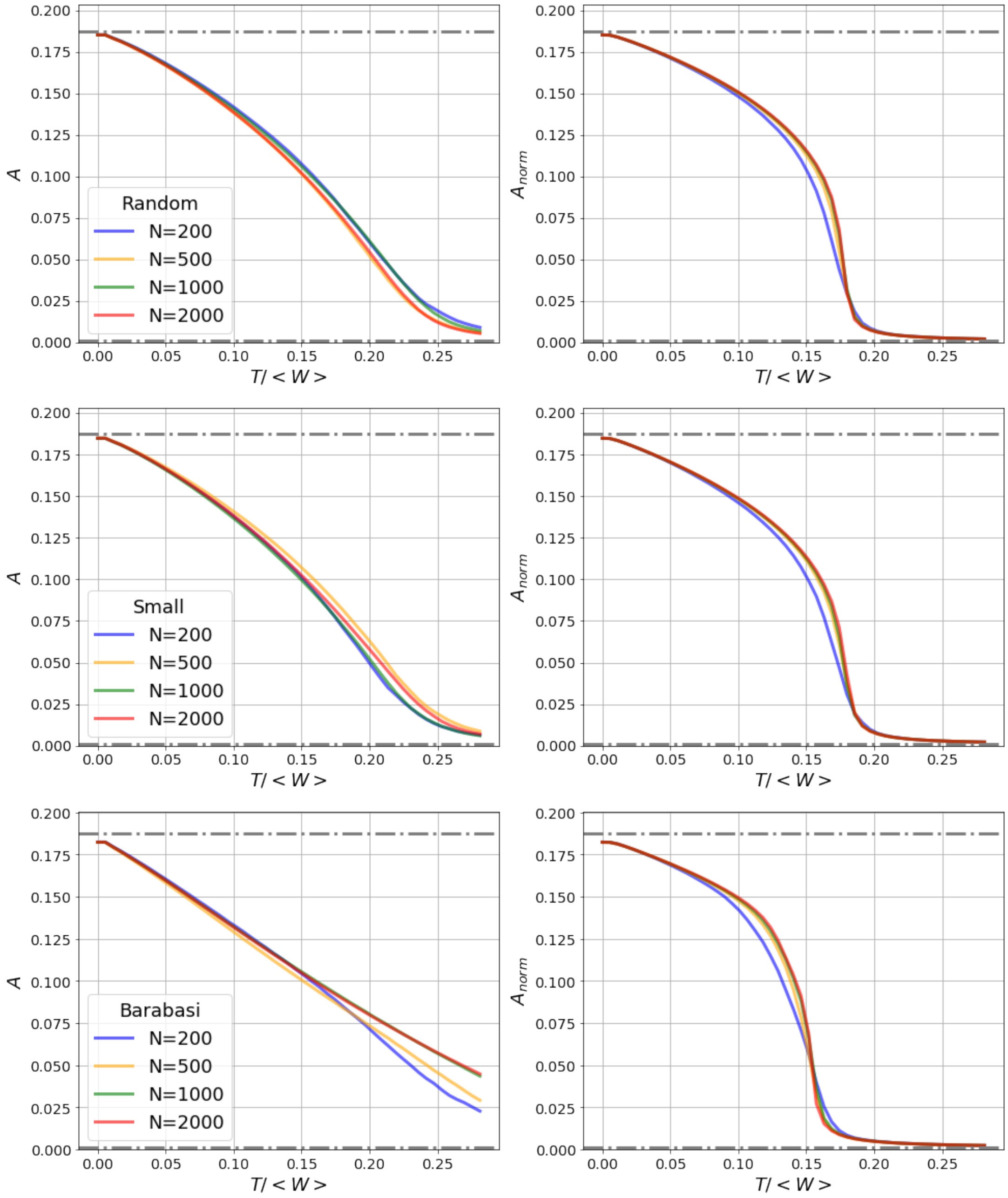

Figure 4.12: Finite size scaling of the activity for different networks with $\langle k \rangle = 15$. The *dashed lines* are the theoretical expectation of x_+ and x_-. Each color represents the average over different realizations of the network for each size N.

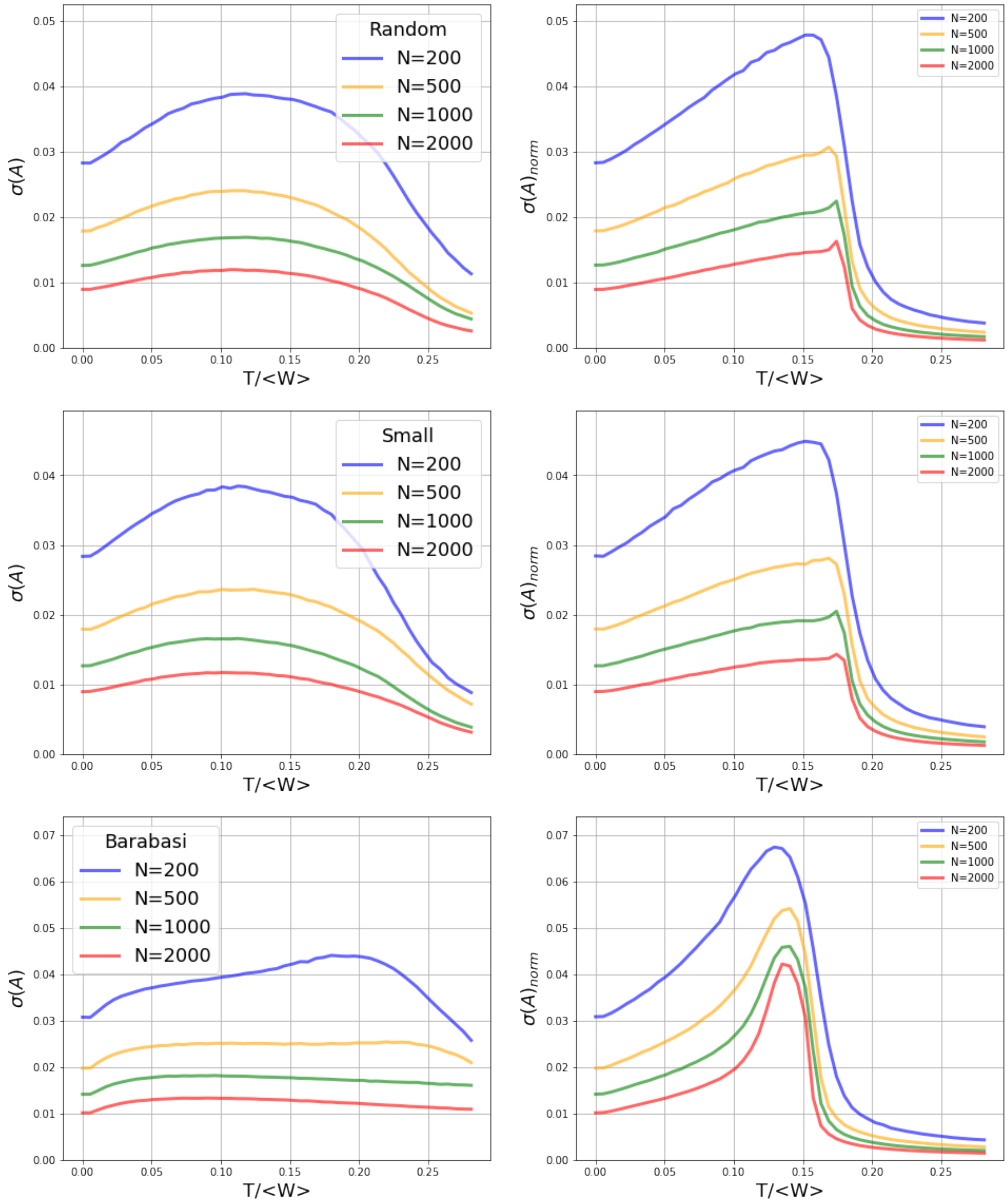

Figure 4.13: Finite size scaling of $\sigma(A)$ for different networks with $\langle k \rangle = 15$. Each color represents the average over different realization of network for each size N.

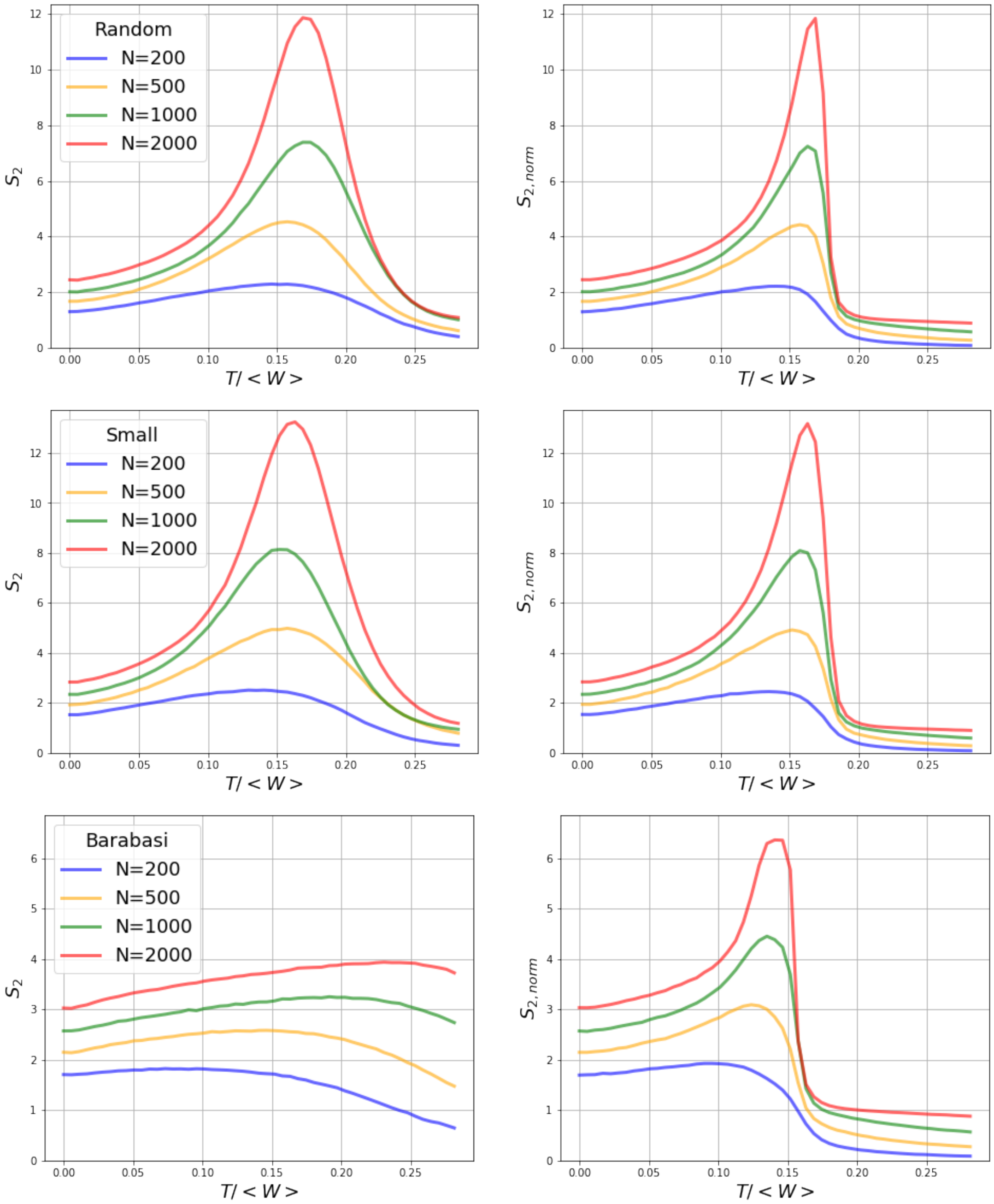

Figure 4.14: Finite size scaling of the second cluster size for different networks with $\langle k \rangle = 15$. Each color represents the average over different realization of network for each size N.

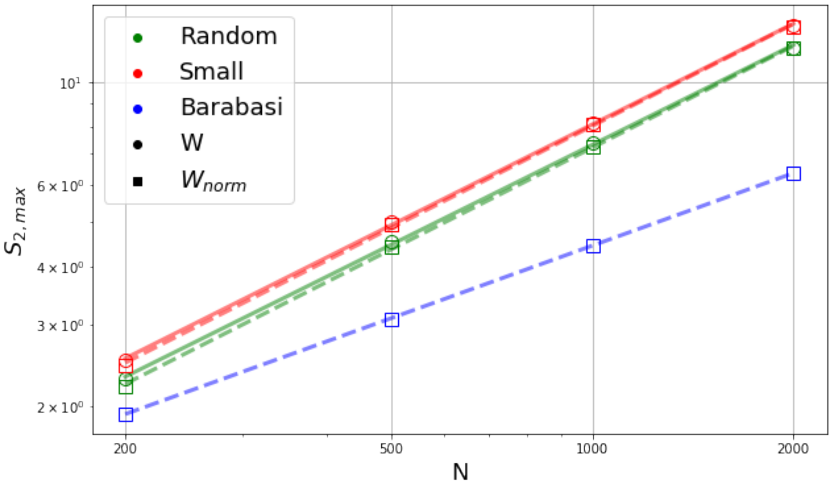

Figure 4.15: Scaling of the maximum of the second cluster size S_2 as a function of network size N. The lines display a power-law interpolation.

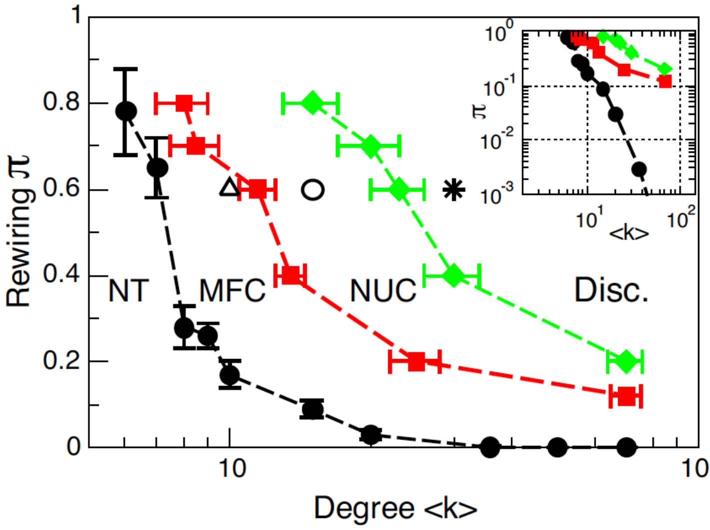

Figure 4.16: Parameter space for the topology values $(\pi; \langle k\rangle)$ in the simulations of small-world networks, where π is the rewiring probability and $\langle k\rangle$ is the average degree. Below the black line there is no dynamical phase transition (NT). Between the black line and the red dashed one (MFC) the behavior became scale-invariant with exponents consistent with the mean field percolation universality class. Further above, in the region denoted as NUC, behavior can be still scale invariant and critical (i.e. the transition is still second order) but without universal exponents. Finally, above the green dashdotted line, the transition becomes discontinuous (Disc.) and the dynamic is short-range correlated and oscillatory. In the inset the same data is plotted in double log axis to best denote the relative sizes of each dynamical regime. From [78].

Chapter 5

Conclusions and future perspectives

In this Thesis we have focused on a recently proposed stochastic dynamical model of interconnected nodes following the empirical structure of neuroanatomical connections [35]. What makes it interesting also from a neuroscientific point of view, is the ability to replicate fundamental features of spontaneous brain activity repeatedly seen in fMRI experiments. However, such correspondence is made possible only for a particular value in the parameter space spanned by the control parameter that resembles a critical point in a second-order phase transition. Therefore in Chapter 2 we have contextualized the model in the emerging, but still controversial, *critical brain hypothesis* [16,80] by reviewing some of the most promising evidences of critical dynamics in the human brain and the benefits the brain might reap from tuning itself at the edge of a critical phase transition.

Then in Chapter 3 we also explore further evidence of critical dynamics in HTC model in order to provide additional confirmations of the critical nature of the model. Of particular interest are the neuronal avalanches [22], an appealing probe of criticality in neural systems, even though scale free avalanches can be displayed also by non-critical systems [27]. For our current knowledge the avalanches had not yet been investigated in HTC model and our first approach requires to be developed in more detail.

Another crucial aspect in HTC model is the role of the topology. Currently, we still have poorly understand to what extent the topological features of the underlying network influence the overall dynamics. We try to investigate this issue in Chapter 4 by simulating the model over "synthetic" connectomes generated from the commons models of network structures. Hopefully in the future deeper insights would be possible also thanks to advancements in the young field of *network neuroscience* [37].

Moreover, a recent work that is currently under review demonstrates how lesions to the biological connectivity due to strokes alters the dynamics to the point that the critical transition is no longer present compared to healthy control patients [81]. These results open significant horizons regarding personalized brain modelling, since HTC model along with empirical connectivity data at the level of single subjects might be used as a biomarker for assessing brain health.

Finally, because of the increasing importantance of the critical brain hypothesis both in neuroscientific and clinical fields, a more theoretical understanding is required. In this sense we propose a mathematical description of the model via mean-field approximation that provide us some interesting hints regarding the nature of the critical transitions

(Appendix B). However, human connectomes are quite far from a mean-field topology, therefore it is necessary a more precise description. The use of the so-called *heterogeneus mean field* seems a prominent idea to prosecute [82]. In addition, such theoretical framework can be extended to analyze the presence of oscillations in the network activity, for instance by applying the *Van Kampen expansion* [83] to the Fokker-Planck equation Eq.(B.9).

Appendix A

A Hint of Network theory

In this Appendix we briefly introduce some basic theoretical tools used to describe and analyze networks, most of which come originally from the mathematical branch of graph theory. We mainly follow the discussion and the formalism presented in [84].

As previously mentioned, *graph* is commonly used as a synonym for *network*, a collection of nodes (or vertices) joined by edges (or links). Most of the networks have at most a single edge between any pair of nodes. In the rare cases where there can be more than one edge between the same nodes, those edges are collectively referred as a *multiedge*. In most networks there are also no edges that connect nodes to themselves, although such edges can occur in a few situations. Edges that connect nodes to themselves are called *self-edges* or *self-loops*. In the rest of the Chapter we will focus on networks that has neither self-edges nor multiedges, called *simple networks*.

In addition, a link may represent a reciprocal relation between a pair of nodes, i.e. in *undirected networks*, or it may have a direction, pointing from one node to another, i.e. in *directed networks*.

A.1 Adjacency matrix

There are a number of different ways to represent a network mathematically. Consider a network with N nodes and let us label the nodes with integer labels $1, ..., N$. Clealy, it does not matter which node gets which label, only that each label is unique, so that we can use the labels to refer to any nodes unambiguously.

The *adjacency matrix* $\mathbf{A}$ of a directed network is defined as the NxN matrix with elements A_{ij} such that:

$$A_{ij} = \begin{cases} 1 \text{ if there is an edge from node } j \text{ to node } i \\ 0 \text{ otherwise} \end{cases} \tag{A.1}$$

A couple of points to note about the adjacency matrix: the direction of the edge runs from the second index to the first; for a network with no self-edges, i.e. $A_{ii} = 0$, the diagonal matrix elements are all zero; for an undirected network, if there is an edge between i and j then there is necessarily an edge between j and i, thus $A_{ij} = A_{ji}$, so the adjacency matrix is symmetric.

In many situations, however, the edges carry on additional informations that cannot be reduced to simple binary connections. Thus it is useful to represent edges as having a strength or a weight, usually a real number. Such *weighted networks* can be represented mathematically by an adjacency matrix with the elements A_{ij} equal to the weights of the corresponding connections.

A.2 Degree and connectance

The most straightforward way to characterize a node is through its level of connectivity with other nodes. The *degree* of a node is the number of edges connected to it. For an undirected network of N nodes the degree of node i, namely k_i, can be written in terms of the adjacency matrix as:

$$k_i = \sum_{j=1}^{N} A_{ij} \tag{A.2}$$

The sum of the degrees is also related to the total number of edges m in the network:

$$m = \frac{1}{2}\sum_{i=1}^{N} k_i = \frac{1}{2}\sum_{ij} A_{ij} \tag{A.3}$$

From a macroscopic perspective, the maximum possible number of edges in a simple network is $\binom{N}{2}$. The *connectance* or *density* ρ of a graph is the fraction of those edges that are actually present:

$$\rho = \frac{m}{\binom{N}{2}} = \frac{2m}{N(N-1)} = \frac{\langle k \rangle}{N-1} \tag{A.4}$$

where $\overline{k}$ is the average degree. We can note that the density ρ strictly lies in the range $0 \leq \rho \leq 1$, so it can be interpeted as the probability that a pair of nodes picked randomly is connected by an edge.

In a directed network we have to distinguish between two type of degrees: the *in-degree*, i.e. the number of ingoing edges connected to a node, and the *out-degree*, i.e. number of outgoing edges. From the adjacency matrix definition, in- and out-degrees can be written as:

$$k_i^{in} = \sum_{j=1}^{N} A_{ij} \qquad k_j^{out} = \sum_{i=1}^{N} A_{ij} \tag{A.5}$$

A.3 Components

A network might not consist of just a single connected set of nodes. Many networks have two or more separate parts that are disconnected from one another. Such parts are called *components.*

Technically, a component is a subset of the nodes of a graph such that there exists at least one *path*, i.e. a sequence of nodes such that every consecutive pair of nodes in the sequence is connected by an edge, from each element of that subset to each other, and such that no other node in the network can be added to the subset while preserving this property.

A network in which all nodes belong to the same single component is said to be *connected.* Conversely, a network with more than one component is *disconnected.*

A.4 Measures and metrics

The adjacency matrix contains in principle all the information about the structure of a network. However, such raw data are not easy for humans to comprehend, especially for more complex networks. It is therefore necessary to introduce some mathematical measures that capture interesting features of network structure quantitatively.

A.4.1 Centrality and hubs

The nodes of a network do not have all the same importance or, in other words, the same *centrality* in the network. There are many possible definitions of importance and correspondingly many centrality measures. We are now going to describe just a few of the definitions of centrality that can be found in the literature.

Perhaps the simplest centrality measure for a node in a network is just the number of edges connected to it, i.e. its degree, sometimes called *degree centrality.*

The degree considers neighbours as equivalent. However, not all neighbours are equal. In many cases, a node's importance in a network is increased by having connections to other nodes that are themselves important. *Eigenvector centrality* is an extension of degree centrality that takes this factor into account by evaluating the centrality x_i of a node i as proportional to the centrality scores of the neighbors, that making use of the adjacency matrix becomes:

$$x_i = \kappa^{-1} \sum_{j=1}^{N} A_{ij} x_j \tag{A.6}$$

where κ is the constant of proportionality. Such formula can be also written in matrix notation as:

$$\boldsymbol{A}\boldsymbol{x} = \kappa \boldsymbol{x} \tag{A.7}$$

where $\boldsymbol{x}$ is the vector with elements equal to the centrality scores x_i. In other words, $\boldsymbol{x}$ is an eigenvector of the adjacency matrix. Since there are N different eigenvectors of the NxN adjacency matrix, the centrality scores are still not completely defined. It is usually assumed that $\boldsymbol{x}$ is the eigenvector corresponding to the largest eigenvalue. In this way, thanks to *Perron-Frobenius theorem*, the centrality scores are non-negative.

A different concept of node importance is captured by *betweenness centrality*, which measures the extent to which a node lies on paths between other nodes. If we assume that information always takes the shortest available path through the network, the amount of information passing through each node is proportional to the number of shortest paths the node lies on. This number of shortest paths is exactly the betweenness centrality.

It seems plausible that nodes with highest betweenness centrality are crucial to efficient communication in the network. Nodes with high degree or high centrality are usually called *hubs.* If a hub is removerd, all the information that would have passed through that node must now be rerouted another way, that in most cases will be a longer path, thus more expensive in term of energy resources.

A.4.2 Clustering

Another important notion is *transitivity.* In the language of graph theory it is implicit that the relation for which transitivity is analyzed is "a node being connected by an edge". So if node u is connected to node v, and v is connected to w, then u is also connected to w if the relation is transitive. In the language of social networks, "the friend of your friend is likely also to be your friend". The level of network transitivity can be quantify as the fraction of paths of length two in the network that are also closed, named *clustering coefficients*:

$$C = \frac{\text{(number of closed paths of length two)}}{\text{(number of paths of length two)}} \tag{A.8}$$

$C = 1$ implies perfect transitivity, while $C = 0$ implies no closed triads. The most common way of defining the clustering coefficient is perhaps in term of triangles of connected nodes:

$$C = \frac{\text{(number of triangles)x3}}{\text{(number of connected triples)}} \tag{A.9}$$

The clustering coefficient is also a measure of the degree to which nodes in a graph tend to cluster together. The above definition is a property of an entire network, but it can be easily extended to the level of single nodes with the so-called *local clustering coefficient*:

$$C_i = \frac{\text{(number of pairs of neighbours of } i \text{ that are connected)}}{\text{(number of pairs of neighbours of } i\text{)}} \tag{A.10}$$

A.4.3 Assortativity

Suppose we have a network in which the nodes are classified according to some characteristic that has a finite set of possible values. For instance, the nodes could represent people and be classified according to many features such as nationality, political orientation, or gender. Or in the case of brain networks, the nodes may be classified according to the anatomical region. It turns out in many systems that nodes have a strong tendency to associate with others whom they perceive as being similar to themselves in some way. This tendency is called *homophily* or *assortative mixing.*

A network is said to be assortative if a significant fraction of the edges in the network run between nodes of the same type. However, such fraction in many cases is 1 if all nodes belong to the same single type. A better measure turns out to be the following: w take the fraction of edges that run between nodes of the same type, and then we subtract the fraction of such edges we would expect to find if edges were positioned at random without regard for node type.

If we denote by g_i the group of node i, which is a integer $1, ..., n_g$, with n_g being the total number of groups, then the total number of edges that run between nodes of the same type is:

$$\sum_{\text{edges}(i,j)} \delta_{g_i g_j} = \frac{1}{2} \sum_{ij} A_{ij} \delta_{g_i g_j} \tag{A.11}$$

where δ_{ij} is the Kronecker delta. Instead, the expected number of edges between all pairs of vertices of the same type is:

$$\frac{1}{2} \sum_{ij} \frac{k_i k_j}{2m} \delta_{g_i g_j} \tag{A.12}$$

where m is the total number of edges. We therefore define the *modularity* as:

$$Q = \frac{1}{2} \sum_{ij} \left(A_{ij} - \frac{k_i k_j}{2m} \right) \delta_{g_i g_j} \tag{A.13}$$

This is a measure of the extent to which like is connected to like in a network. This quantity is strictly less than 1, takes positive values if there are more edges between nodes of the same type than we would expect by chance, and negative ones if there are less.

A better approach is to use the *assortativity coefficient*:

$$r = \frac{\sum_{ij}(A_{ij} - k_i k_j/2m) x_i x_j}{\sum_{ij}(k_i \delta_{ij} - k_i k_j/2m) x_i x_j} \tag{A.14}$$

where x_i is the value of a given property of node i. Even if not immediately obvious, this is an example of a (Pearson) correlation coefficient.

A.4.4 Community structure

In real-world network, it is common to observe a number of densely connected clusters of nodes, corresponding to groups of units with similar features. As an example, each group may correspond to scientists who have worked closely together or close friends between high school students. The problem of finding groups of nodes in networks is called *community detection*. More formally, community detection is intended to find the natural divisions of a network into groups of nodes such that there are many edges within groups and few edges between them. Altough it turns out to be a challenging task, but a number of methods have been developed that return good results in practical situations.

The most widely used approach is the method of *modularity maximization*. It searches for the division that has the highest modularity score already presented in Eq.(A.13). However, applying the modularity maximization method directly is a hard task, since it has to score all the possible assignments of the nodes to the groups, which is exponential in the number of groups. So a range of heuristic algorithms have been proposed that finds approximate but acceptable solutions.

A.5 Models of network structure

In the preceding sections we have looked at how the structure of networks is measured. This section is devoted to an examination of some of the most widely used models of network structure, models that mimic the patterns of connections in real-world networks and were also used for the simulations of HTC model.

A.5.1 Random graphs

A *random graph* is a model network in which the values of certain properties are fixed, but the network is in other respects random. One of the most common examples of random graphs is the one where we fix only the number of nodes N and the number of edges m or the probability p of edges between nodes. The second class of models, $G(N, p)$, is usually referred as *Erdős-Rényi graph* or *Poisson random graph* because the probability p_k of a node to be connected to other k nodes is:

$$p_k = \binom{N-1}{k} p^k (1-p)^{N-1-k} \tag{A.15}$$

thus the degree distribution is binomial.

As we said, the number of edges m in the Erdős-Rényi model is not fixed, but its expectation $\langle m \rangle$ can be easily computed:

$$\langle m \rangle = \binom{N}{2} p \tag{A.16}$$

and we can further derive the average degree $\langle k \rangle$:

$$\langle k \rangle = \left\langle \frac{2m}{N} \right\rangle = \frac{2\langle m \rangle}{N} = (N-1)p \xrightarrow[N \to \infty]{} Np \tag{A.17}$$

Another measure that is very easy to derive is the clustering coefficient:

$$C = \frac{\langle k \rangle}{N-1} \tag{A.18}$$

This is one of several respects in which the random graph differs sharply from most real-world networks. Indeed, real-world networks often have quite high clustering coefficients, while Eq.(A.18) tends to zero for $N \to \infty$ and even for the finite values of N appropriate to real-world networks the value of C in the random graph is often very small. Moreover, there is no correlation between the degrees of adjacent nodes, since the edges are placed completely at random, thus interesting structure communities or hubs do not emerge.

A.5.2 Small-world graphs

The *small-world model* is a stylized model first proposed by Watts and Strogatz [85] originally intended to illustrate how two characteristic features of social networks—high clustering coefficient and short path lengths—can coexist in the same network.

The model is construct as follows. One starts off with a regular lattice of some kind, for instance with a ring where each node is connected to its l nearest neighbours. Then, this network is randomized by rewiring some of the edges from their positions to new random positions. Specifically, each of the edges is removed with some probability p and replace it with another that joins two nodes chosen uniformly at random from the network. The randomly placed edges are commonly referred to as shortcuts because, they create shortcuts from one part of the ring to another.

To be noted that during the rewiring procedure the total number of edges remain unchanged, so the average degree is simply:

$$\langle k \rangle = l \tag{A.19}$$

In a regular lattice, i.e. $p = 0$, the clustering coefficient is quite high but the average path lenghts between two random chosen nodes is very high. On the other hand, a random graph, i.e. $p = 1$, is characterized by short path lenghts but low clustering coefficient. In the small-world model there is a significant parameter range in between in which the network has both properties simultaneously, short paths and high clustering.

A.5.3 Scale-free graphs

Many networks are observed to have degree distributions that approximately follow power laws and the presence of highly connected hubs. Examples include the Internet, the World Wide Web, citation networks, and some social and biological networks. A possible mechanism of network formation that give rise to a power-law distribution is the *preferential attachment*, a name coined by Barabási and Albert [86].

If we think to a social network, it is more easy for a people with a very large number of friends to meet new people. The same happens also in a citation network, where a famous paper is more likely to be cited in the future. The preferential attachment mechanism can be thus summarized under the maxima "*the rich get richer*". Indeed, such type of networks are created in a dynamical way: starting with a fully connected clique of q_0 nodes, new vertices are continually added to the network. Each new node is connected to $q \leq q_0$ existing nodes with a probability p_i that is proportional to the number of links that the existing nodes already have, i.e. its degree k_i:

$$p_i = \frac{k_i}{\sum_j k_j} \tag{A.20}$$

In the limit of large degree k, the degree distribution p_k gives:

$$p_k \sim k^{-3} \tag{A.21}$$

that is precisely a scale-free distribution with exponent $\alpha = -3$.

The average degree in a Barabási-Albert graph of size N can be estimated in the following way: the initial number of edges is $\binom{q_0}{2}$, then the other $(N - q_0)$ brings q new edges each, so the total number of edges m in the network is:

$$m = \frac{N\langle k\rangle}{2} = \frac{q_0(q_0-1)}{2} + q(N - q_0) \tag{A.22}$$

We further assume that $q = q_0$, so the expected degree $\langle k\rangle$ becomes:

$$\langle k\rangle = 2q - \frac{q}{N} - \frac{q^2}{N} \xrightarrow[N\to\infty]{} 2q \tag{A.23}$$

Appendix B

Mean-field approximation

In this Appendix we present the derivation of a Master Equation that describes the temporal evolution of HTC model in the mean-field approximation. Furthermore, we notice the emergence of two stable equilibria that even coexist for a certain range of thresholds.

B.1 Derivation of the master equation

The HTC model describe a network of N neurons that can be in one of three possible states: active x, refractory y, and inactive $\emptyset$. We redefine respectively the number and the density of: active nodes n_x and x; refractory nodes n_y and y; inactive nodes $n_\emptyset$ and $\emptyset$. We recall the possible reactions between the states:

$$\begin{cases} \emptyset \xrightarrow{p_{act}} x \\ x \xrightarrow{1} y \\ y \xrightarrow{r_2} \emptyset \end{cases} \tag{B.1}$$

where p_{act} is the probability of activation and r_2 is the rate of escaping from refractoriness. Once activated, a neuron becomes refractory, i.e. it passes from x to y, with probability 1. A neuron fires, i.e. becomes active with probability 1, if the weighted sum of neighbouring activation is larger than the threshold T, otherwise it can activate with probability r_1. So we can model the total probability p_{act} of transition from inactive to active state as:

$$p_{act} = r_1 + (1 - r_1)\Theta\left[\sum_j W_{ij} s_j - T\right] \tag{B.2}$$

where $\Theta[\ \cdot\ ]$ is the Heaviside step function: it is equal to 1 if the argument is positive, otherwise it is null.

Here we propose a mean-field approximation of the model, namely we assume that the underlying graph W is fully-connected, so each node is structurally connected to every other. Moreover, we introduce a further approximation on the connections between the pairs of nodes, that we assume constant in all the network, i.e. $W_{ij} = c \ \ \forall i, j$. In this way, considering also the homeostatic normalization, the weights of the structural matrix are:

$$\widetilde{W}_{ij} = \frac{W_{ij}}{\sum_j W_{ij}} = \frac{c}{\sum_j c} = \frac{c}{Nc} = \frac{1}{N} \tag{B.3}$$

Thus the argument inside $\Theta[\,\cdot\,]$ in Eq.(B.2) becomes:

$$\begin{aligned}\sum_j \widetilde{W}_{ij} s_j - T &= \frac{1}{N}\sum_j s_j - T \\ &= \frac{n_x}{N} - T \\ &= x - T\end{aligned} \tag{B.4}$$

The reactions in Eq.(B.1) are translated in the following transition rates:

$$\begin{cases} T[(n_x, n_y) \to (n_x + 1, n_y)] = (N - n_x - n_y)[r_1 + (1 - r_1)\theta(x - T)] = T^+ \\ T[(n_x, n_y) \to (n_x - 1, n_y + 1)] = n_x = T^{-+} \\ T[(n_x, n_y) \to (n_x, n_y - 1)] = r_2 n_y = T^- \end{cases} \tag{B.5}$$

From these rates we can summarize the temporal evolution of the probability $P(n_x, n_y)$ that at a certain time the network has n_x active, n_y refractory and $n_\emptyset = N - n_x - n_y$ neurons, by mean of the following *master equation*:

$$\begin{aligned}\dot{P}(n_x, n_y) = &\; P(n_x - 1, n_y)\; T^+ \\ &+ P(n_x + 1, n_y - 1)\; T^{-+} \\ &+ P(n_x, n_y + 1)\; T^- \\ &- P(n_x, n_y)\; [T^+ + T^{-+} + T^-]\end{aligned} \tag{B.6}$$

From here on we describe the system by the density of active and refractory neurons, respectively $x = n_x/N$ and $y = n_y/N$, so $\Delta x = 1/N$, $\Delta y = 1/N$. Thus we can normalize the rates:

$$\begin{cases} \widetilde{T}^+(x, y) = (1 - x - y)[r_1 + (1 - r_1)\theta(x - T)] = T^+/N \\ \widetilde{T}^{-+}(x, y) = x = T^{-+}/N \\ \widetilde{T}^-(x, y) = r_2 y = T^-/N \end{cases} \tag{B.7}$$

and describe the state of the system by mean of $P(x, y)$. We assume that both $P(x, y)$ and the rates $\widetilde{T}$ vary smoothly with x and y, meaning that we can effectively treat them as differentiable function. This is clearly an approximation if N is finite, but in the limit of large N, Δx and Δy become infinitesimal. This allows to make Taylor expansions for the terms $\widetilde{T}(x \pm \Delta x, y \pm \Delta y)$ and $P(x \pm \Delta x, y \pm \Delta y)$ up to the second order, ignoring all higher order, as follows:

$$\begin{aligned}&\widetilde{T}(x \pm \Delta x, y \pm \Delta y)P(x \pm \Delta x, y \pm \Delta y) = \widetilde{T}(x, y)P(x, y) \\ &\pm \Delta x \frac{\partial}{\partial x}[\widetilde{T}(x, y)P(x, y)] \pm \Delta y \frac{\partial}{\partial y}[\widetilde{T}(x, y)P(x, y)] \\ &+ \frac{1}{2}\Delta x^2 \frac{\partial^2}{\partial x^2}[\widetilde{T}(x, y)P(x, y)] + \frac{1}{2}\Delta y^2 \frac{\partial^2}{\partial y^2}[\widetilde{T}(x, y)P(x, y)] \\ &\pm \frac{1}{2}\Delta x \Delta y \frac{\partial}{\partial x}\frac{\partial}{\partial y}[\widetilde{T}(x, y)P(x, y)] + O(\Delta x^3, \Delta y^3)\end{aligned} \tag{B.8}$$

By taking the continuum limit of the master equation Eq.(B.6) and by expanding all the terms up to the second order as shown in Eq.(B.8), we obtain the so-called *Fokker-Plank* *equation* for the probability density $p(x,y)$:

$$\begin{aligned}\frac{\partial}{\partial t}p(x,y) = &-\frac{\partial}{\partial x}[A_1(x,y)p(x,y)] + \frac{1}{2N}\frac{\partial^2}{\partial x^2}[B_{11}(x,y)p(x,y)]+\\ &-\frac{\partial}{\partial y}[A_2(x,y)p(x,y)] + \frac{1}{2N}\frac{\partial^2}{\partial y^2}[B_{22}(x,y)p(x,y)]+\\ &+\frac{1}{2N}\frac{\partial^2}{\partial x\partial y}[(B_{12}(x,y)+B_{21}(x,y))p(x,y)]\end{aligned} \tag{B.9}$$

where the coefficients are:

$$\begin{cases} A_1(x,y) &= (1-x-y)[r_1+(1-r_1)\Theta(x-T)]-x\\ A_2(x,y) &= x-r_2y\\ B_{11}(x,y) &= (1-x-y)[r_1+(1-r_1)\Theta(x-T)]+x\\ B_{22}(x,y) &= r_2y+x\\ B_{12}(x,y) &= -x\\ B_{21}(x,y) &= -x\end{cases} \tag{B.10}$$

and $P(x,y) = p(x,y)\Delta x\Delta y$. The Fokker-Planck equation is a deterministic differential equation describing how the probability distribution of states $p(x,y)$ evolves over time. Physically, it describes the evolution of an ensemble of systems: if we simulate a huge number of populations of neurons, all with the same parameters, they will have different evolutions due to random fluctuations, but the fraction of systems that have a density of states in $[x, x+dx; y, y+dy]$ at time t will be given exactly by $p(x,y)dxdy$ (in the limit of an infinite ensemble).

An equivalent description can be derived by instead following a single population of neurons. In this case, a change in population density $[dx, dy]$ under the effect of stochastic fluctuations ξ is given by the *Langevin equation*:

$$\begin{bmatrix}\dot{x}\\ \dot{y}\end{bmatrix} = \begin{bmatrix}A_1(x,y)\\ A_2(x,y)\end{bmatrix} + \frac{1}{\sqrt{N}}\begin{bmatrix}B_{11}(x,y) & B_{12}(x,y)\\ B_{21}(x,y) & B_{22}(x,y)\end{bmatrix}^{1/2}\begin{bmatrix}\xi_1\\ \xi_2\end{bmatrix} \tag{B.11}$$

where $\boldsymbol{\xi} = [\xi_1, \xi_2]$ is an uncorrelated 2d white gaussian noise, i.e. such that $\xi_i \sim N(0,1)$ and $\langle\xi_i(t)\xi_j(t')\rangle = \delta_{ij}\delta(t-t')$. Indeed Eq.(B.11) is an example of stochastic differential equation. It can be noticed how $\boldsymbol{A}(x,y)$ are deterministic drift term, while $\boldsymbol{B}(x,y)$ encloses the stochastic diffusive part [87].

B.2 Thermodynamic limit

In the limit of a large number of interacting units in the system, the effect of random fluctuations are gradually less evident. In the thermodynamic limit $N \to \infty$, the diffusive terms in the Langevin equation Eq.(B.11) disappear:

$$\begin{cases}\dot{x} = (1-x-y)[r_1+(1-r_1)\Theta(x-T)]-x\\ \dot{y} = x-r_2y\end{cases} \tag{B.12}$$

The evolution of the systems is thus described by a deterministic map. We try to analitically solve Eq.(B.12) but it seems intractable. Nevertheless, we can still explore the existence of equilbria in the system. We are going to show that the dynamics of the system discriminates between two different regimes based on the value of $\Theta[\,\cdot\,]$, each one with its own equilibrium, by varying the threshold T. Since these two phases are characterized by respectively high and low level of activity, we call them super- and sub-critical phases.

We further investigate the nature of the equilibria through *linear stability analysis* techniques [88]. Indeed Eq.(B.12) is a map of the type:

$$\dot{\boldsymbol{z}} = \boldsymbol{f}(\boldsymbol{z}) \tag{B.13}$$

with $\boldsymbol{z} = (x, y)$ a 2-dimensional vector. The equilibria $\boldsymbol{z}^*$ of this map are the ones that satisfy $\boldsymbol{f}(\boldsymbol{z}^*) = 0$. If we focus on the dynamics near the fixed points, we can perform a change of variables $x = x^* + \Delta x$, $y = y^* + \Delta y$. In the limit of small variations $|\Delta \boldsymbol{z}| \to 0$, meaning that we are considering states infinitesimally near the fixed points, Eq.(B.13) can be Taylor-expanded as:

$$\begin{aligned} \dot{\Delta \boldsymbol{z}} &= \boldsymbol{f}(\boldsymbol{z}^*) + \frac{\partial \boldsymbol{f}}{\partial \boldsymbol{z}}\bigg|_{\boldsymbol{z}=\boldsymbol{z}^*} \Delta \boldsymbol{z} + \dots \\ &= \boldsymbol{J}(\boldsymbol{z}^*)\Delta \boldsymbol{z} \end{aligned} \tag{B.14}$$

Thus the dynamics near the fixed points is governed, at the first order, only by the Jacobian matrix $\boldsymbol{J}$. In particular, the (real part of) the eigenvalues λ of $\boldsymbol{J}$ can tell us information regarding the stability or instability. If $max\ Re(\lambda) > 0$, the trajectories asymptotically diverge from the equilibria, otherwise for $max\ Re(\lambda) < 0$ the trajectories converge to the fixed point, which is stable in this case.

B.2.1 Super-critical phase

In the super-critical phase $x > T$ and at stationarity, Eq.(B.12) leads to:

$$\begin{cases} y_+ = \dfrac{1}{2r_2 + 1} =: C(r_2) \\ x_+ = r_2 C(r_2) \end{cases} \tag{B.15}$$

The disequality $x > T$ must be satisfied by the equilibrium Eq.(B.15) in order to exist. So the super-critical equilibrium (x_+, y_+) exists only if:

$$T < \frac{r_2}{2r_2 + 1} =: T_+(r_2) \tag{B.16}$$

The jacobian evaluated at (x_+, y_+) is:

$$J_+ = \begin{bmatrix} -2 & -1 \\ 1 & -r_2 \end{bmatrix} \tag{B.17}$$

The eigenvalues of Eq.(B.17) are:

$$\lambda_+ = -\frac{2 + r_2 \pm i\sqrt{4r_2 - r_2^2}}{2} \tag{B.18}$$

The stability condition holds if:

$$Re(\lambda_+) = -1 - \frac{r_2}{2} < 0 \tag{B.19}$$

which is always satisfied (since the rate r_2 indentifies a probability, so $0 \leq r_2 \leq 1$), thus the super-critical fixed point (x_+, y_+) is a *stable focus*.

B.2.2 Sub-critical phase

In the sub-critical phase $x \leq T$ and at stationary, Eq.(B.12) leads to:

$$\begin{cases} y_- = \dfrac{r_1}{r_2 + (r_2+1)r_1} =: D(r_1, r_2) \\ x_- = r_2 D(r_1, r_2) \end{cases} \tag{B.20}$$

Again, the disequality $x \leq T$ must be satisfied by (B.20) in order to observe the fixed point. So the sub-critical equilibrium (x_-, y_-) exists only if:

$$T \geq \frac{r_1 r_2}{r_2 + (r_2+1)r_1} =: T_-(r_1, r_2) \tag{B.21}$$

The jacobian evaluated at $[x_-, y_-]$ is:

$$J_- = \begin{bmatrix} -1 - r_1 & -r_1 \\ 1 & -r_2 \end{bmatrix} \tag{B.22}$$

whose eigenvalues are:

$$\lambda_- = \frac{-(1 + r_1 + r_2) \pm \sqrt{(1 + r_1 + r_2)^2 - 4(r_1 + r_2 + r_1 r_2)}}{2} \tag{B.23}$$

Also in this phase the stability condition is $Re(\lambda_-) < 0$ is satisfied $\forall r_1, r_2$ (since $0 \leq r_1 \leq 1$ and $0 \leq r_2 \leq 1$).

We observe two different regimes by varying the parameters r_1 and r_2: if $r_1 - 2\sqrt{r_1} + 1 < r_2$ the eigenvalues have an imaginary part, while in the other case they are pure real (Fig.B.1). So in the first cases the fixed point is a *stable focus*, while it is a *stable knot* in the other case. It can be noted that from a physical point of view, both r_1 and r_2 are usually defined as quite small values in all the simulations, typically less than 10^{-1}. Therefore, in most cases we should observe a *stable knot* at (x_-, y_-).

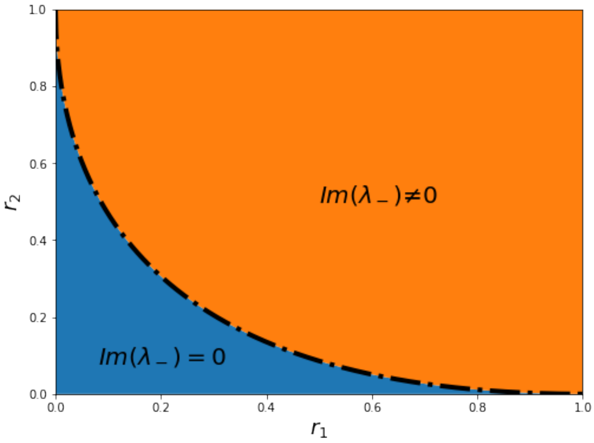

Figure B.1: Eigenvalues λ_- of the sub-critical equilibrium as a function of r_1, r_2. *Blue region*, eigenvalues are pure real. *Orange region*, eigenvalues have non-zero imaginary part. *Dahsed line*, values belonging to the curve $r_2 = r_1 - 2\sqrt{r_1} + 1$ that divide the two regions of parameters.

B.2.3 Diagram of equilibria

As expected, we can notice from Eq.(B.15) and Eq.(B.20) that the fraction of active nodes x_+ at equilibrium in the supercritical phase is always larger (i.e. $\forall r_1, r_2$) than the subcritical equilibrium x_-, since $r_1, r_2 \leq 1$. In addition, in the range of threshold for which the fixed points exist, respectively Eq.(B.16) and Eq.(B.21), these are global equilibrium and are both stable, each one with its own basin of attraction. Moreover, from Eq.(B.16) and Eq.(B.21) we can deduce that $T_- < T_+ \ \forall r_1, r_2$, thus three regions emerge in the parameter space spanned by T (Fig.B.2):

- $T \leq T_-$:
  the sub-critical equilibrium x_- does not exist, so we should observe only the super-critical equilibrium x_+.
- $T_- < T \leq T_+$:
  coexistence of both equilibria x_+ and x_-.
- $T > T_+$:
  only the sub-critical equilibrium x_- exists.

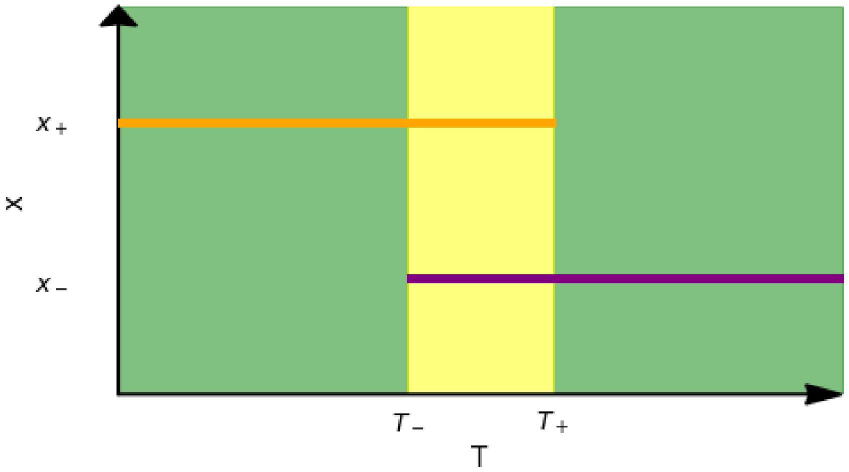

Figure B.2: Diagram of fixed points as a function of the threshold T. *Green regions*, only one fixed point exists. For $T < T_-$, x_- does not exist, so we should observe only x_+. Conversely, for $T > T_+$, x_+ does not exist, so we should observe only x_-. *Yellow region*, coexistence of the two equilibria in the range $T_- < T < T_+$.

Such theoretical predictions are supported by the numerical integration of Eq.(B.12): indeed in the limit of large times, the fraction of active nodes reach the aforementioned equilibria (Fig.B.3).

Finally, we compare the theoretical prevision with simulations of HTC model over a finite-size fully-connected matrix with constant weights. From the trajectories displayed in Fig.B.4 it can be observed that simulated data are consistent with the analytical results. So the mean-field approximation in the thermodynamic limit is predictive of the behaviour of HTC model run over structural matrix with constant entries in the limit of large connectivity.

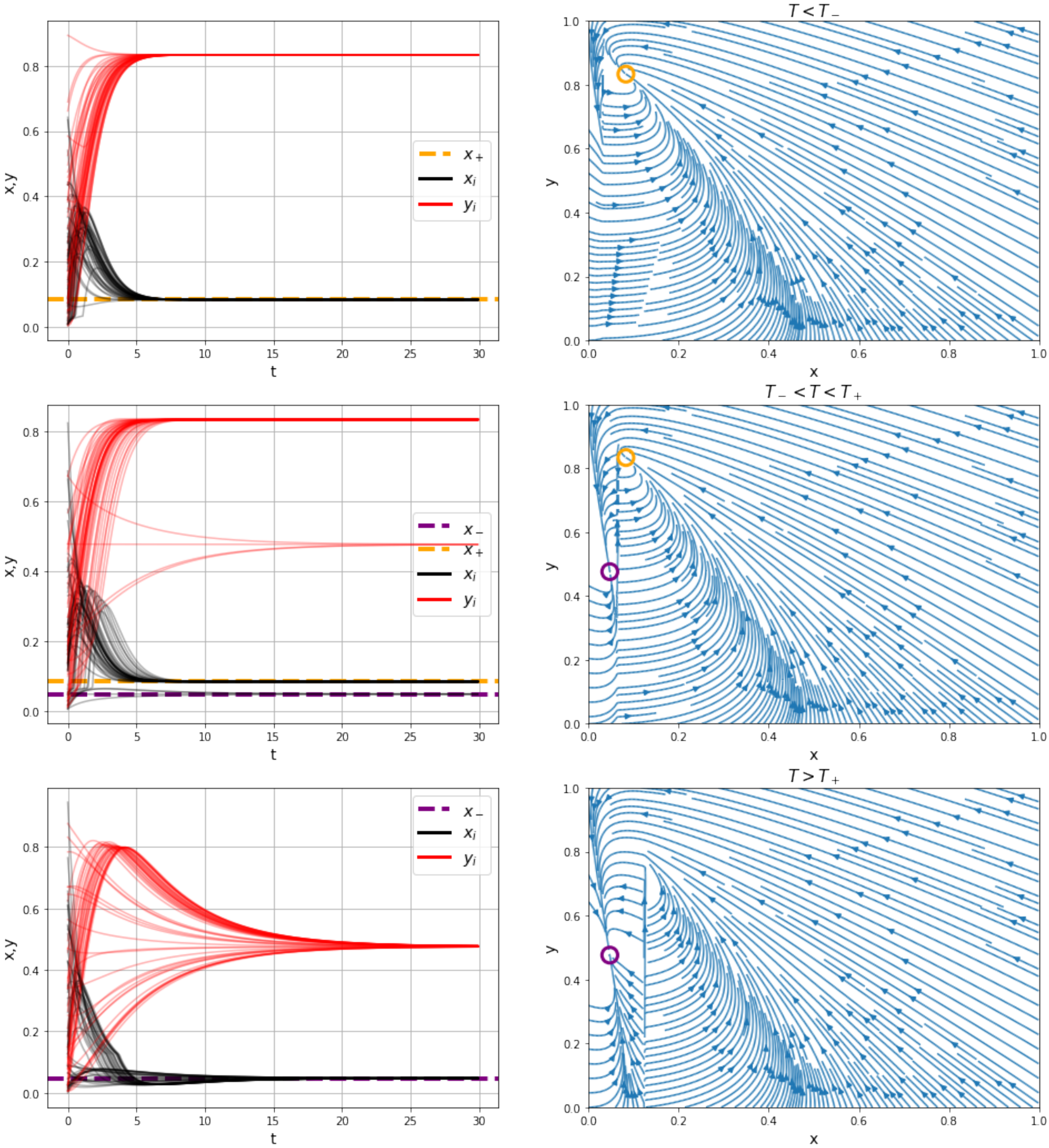

Figure B.3: Numerical integration of the mean-field model in the thermodynamic limit Eq.(B.12) for values of T in the three regions shown in Fig.B.2. *Left column*, trajectories of variables x and y, starting from random initial configurations. (Dire che nel primo e terzo caso, convergono a un solo valore, mentre nel mezzo a due). *Right column*, streamplot of Eq.(B.12). *Orange circle* and *Purple circle* are the theoretical predictions of equilibria from Eq.(B.15) and Eq.(B.20). These results are obtained with $r_1 = 10^{-1}$ and $r_2 = 10^{-1}$, but are consistent also with different choices of parameters.

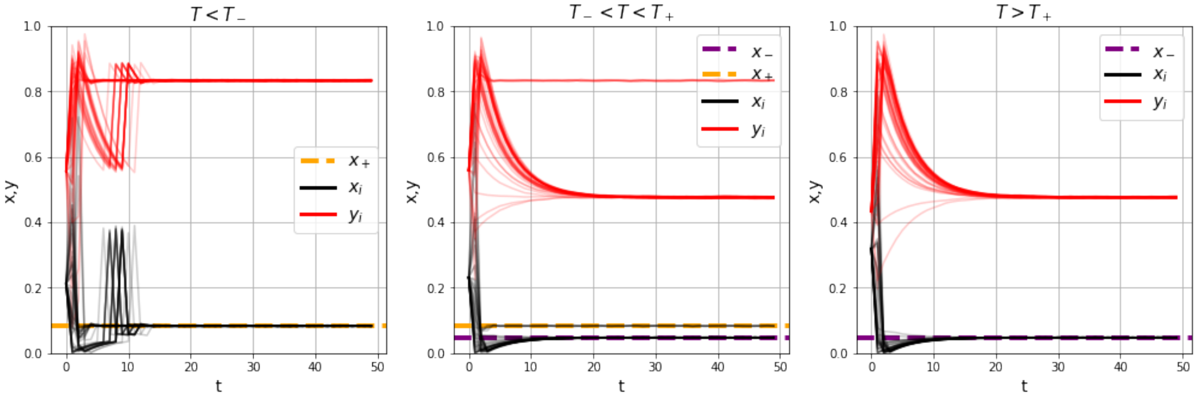

Figure B.4: Theoretical predictions are respected by HTC model simulated over a fully-connected matrix. Network size $N = 10^5$, parameters $r_1 = 10^{-1}$ and $r_2 = 10^{-1}$.

Bibliography

[1] Doug Laney. 3D Data Management: Controlling Data Volume, Velocity, and Variety. *Gartner*, file N. 949. `https://blogs.gartner.com/doug-laney/files/2012/01/ad949-3D-Data-Management-Controlling-Data-Volume-Velocity-and-Variety.pdf`, 6 February 2001.

[2] Jens Eilers, Ralf Schneggenburger, and Arthur Konnerth. *Patch Clamp and Calcium Imaging in Brain Slices*, pages 213–229. Springer US, Boston, MA, 1995.

[3] Alexander C Thompson, Paul R Stoddart, and E Duco Jansen. Optical stimulation of neurons. *Current Molecular Imaging (Discontinued)*, 3(2):162–177, 2014.

[4] Gary H Glover. Overview of functional magnetic resonance imaging. *Neurosurgery Clinics*, 22(2):133–139, 2011.

[5] Terrence J Sejnowski, Patricia S Churchland, and J Anthony Movshon. Putting big data to good use in neuroscience. *Nature Publishing Group*, 17(11):1440–1441, 2014.

[6] National Institutes of Health. BRAIN 2025 Report. `https://braininitiative.nih.gov/strategic-planning/brain-2025-report`, 2014.

[7] Katrin Amunts, Alois C. Knoll, Thomas Lippert, Cyriel M. A. Pennartz, Philippe Ryvlin, Alain Destexhe, Viktor K. Jirsa, Egidio D'Angelo, and Jan G. Bjaalie. The Human Brain Project — Synergy between neuroscience, computing, informatics, and brain-inspired technologies. *PLOS Biology*, 17(7):1–7, 07 2019.

[8] D.C. Van Essen, K. Ugurbil, E. Auerbach, D. Barch, T.E.J. Behrens, R. Bucholz, A. Chang, L. Chen, M. Corbetta, S.W. Curtiss, S. Della Penna, D. Feinberg, M.F. Glasser, N. Harel, A.C. Heath, L. Larson-Prior, D. Marcus, G. Michalareas, S. Moeller, R. Oostenveld, S.E. Petersen, F. Prior, B.L. Schlaggar, S.M. Smith, A.Z. Snyder, J. Xu, and E. Yacoub. The human connectome project: A data acquisition perspective. *NeuroImage*, 62(4):2222–2231, 2012.

[9] Ed Bullmore and Olaf Sporns. Complex brain networks: graph theoretical analysis of structural and functional systems. *Nature Reviews Neuroscience*, 10(3):186–198, 2009.

[10] J. G. White, E. Southgate, J. N. Thomson, and S. Brenner. The structure of the nervous system of the nematode caenorhabditis elegans. *Philosophical Transactions of the Royal Society of London. Series B, Biological Sciences*, 314(1165):1–340, 1986.

[11] Daniel J Felleman and David C Van Essen. Distributed hierarchical processing in the primate cerebral cortex. *Cerebral cortex (New York, NY: 1991)*, 1(1):1–47, 1991.

[12] J.W. Scannell, G.A.P.C. Burns, C.C. Hilgetag, M.A. O'Neil, and M.P. Young. The Connectional Organization of the Cortico-thalamic System of the Cat. *Cerebral Cortex*, 9(3):277–299, 04 1999.

[13] Patric Hagmann, Leila Cammoun, Xavier Gigandet, Reto Meuli, Christopher J. Honey, Van J. Wedeen, and Olaf Sporns. Mapping the structural core of human cerebral cortex. *PLoS Biol*, 6(7), 2008.

[14] James K. Moran, Georgios Michail, Andreas Heinz, Julian Keil, and Daniel Senkowski. Long-range temporal correlations in resting state beta oscillations are reduced in schizophrenia. *Frontiers in Psychiatry*, 10:517, 2019.

[15] Sofie M. Adriaanse, Maja A. A. Binnewijzend, Rik Ossenkoppele, Betty M. Tijms, Wiesje M. van der Flier, Teddy Koene, Lieke L. Smits, Alle Meije Wink, Philip Scheltens, Bart N. M. van Berckel, and Frederik Barkhof. Widespread disruption of functional brain organization in early-onset alzheimer's disease. *PLOS ONE*, 9(7):1–12, 07 2014.

[16] Janina Hesse and Thilo Gross. Self-organized criticality as a fundamental property of neural systems. *Frontiers in Systems Neuroscience*, 8:166, 2014.

[17] Matti Nykter, Nathan D. Price, Maximino Aldana, Stephen A. Ramsey, Stuart A. Kauffman, Leroy E. Hood, Olli Yli-Harja, and Ilya Shmulevich. Gene expression dynamics in the macrophage exhibit criticality. *Proceedings of the National Academy of Sciences*, 105(6):1897–1900, 2008.

[18] P. Rämö, J. Kesseli, and O. Yli-Harja. Perturbation avalanches and criticality in gene regulatory networks. *Journal of Theoretical Biology*, 242(1):164–170, 2006.

[19] Jorge Hidalgo, Jacopo Grilli, Samir Suweis, Miguel A. Muñoz, Jayanth R. Banavar, and Amos Maritan. Information-based fitness and the emergence of criticality in living systems. *Proceedings of the National Academy of Sciences*, 111(28):10095–10100, 2014.

[20] Gabriel Baglietto, Ezequiel V. Albano, and Julián Candia. Criticality and the onset of ordering in the standard vicsek model. *Interface Focus*, 2(6):708–714, 2012.

[21] Dante Chialvo. Emergent complex neural dynamics. *Nature Physics*, 6(10):744–750, 2010.

[22] John M Beggs and Dietmar Plenz. Neuronal avalanches in neocortical circuits. *The Journal of neuroscience: the official journal of the Society for Neuroscience*, 23(35):11167–77, 2003.

[23] Osame Kinouchi and Mauro Copelli. Optimal dynamical range of excitable networks at criticality. *Nature Physics*, 2(5):348–351, May 2006.

[24] John M Beggs. The criticality hypothesis: how local cortical networks might optimize information processing. *Philosophical transactions. Series A, Mathematical, physical, and engineering sciences*, 366(1864):329–43, 2008.

[25] Clayton Haldeman and John M. Beggs. Critical branching captures activity in living neural networks and maximizes the number of metastable states. *Phys. Rev. Lett.*, 94:058101, Feb 2005.

[26] Anthony G. Hudetz, Colin J. Humphries, and Jeffrey R. Binder. Spin-glass model predicts metastable brain states that diminish in anesthesia. *Frontiers in Systems Neuroscience*, 8:234, 2014.

[27] John Beggs and Nicholas Timme. Being critical of criticality in the brain. *Frontiers in Physiology*, 3:163, 2012.

[28] Jonathan Touboul and Alain Destexhe. Power-law statistics and universal scaling in the absence of criticality. *Phys. Rev. E*, 95:012413, Jan 2017.

[29] Karla Batista-García-Ramó and Caridad Ivette Fernández-Verdecia. What we know about the brain structure–function relationship. *Behavioral Sciences*, 8(4), 2018.

[30] Laura E. Suárez, Ross D. Markello, Richard F. Betzel, and Bratislav Misic. Linking structure and function in macroscale brain networks. *Trends in Cognitive Sciences*, 24(4):302–315, 2020.

[31] A. L. Hodgkin and A. F. Huxley. A quantitative description of membrane current and its application to conduction and excitation in nerve. *The Journal of Physiology*, 117(4):500–544, 1952.

[32] AN Burkitt. A review of the integrate-and-fire neuron model: I. homogeneous synaptic input. *Biological cybernetics*, 95(1):1–19, 2006.

[33] Michael Breakspear. Dynamic models of large-scale brain activity. *Nature Neuroscience*, 20(3):340–352, 2017.

[34] Olaf Sporns. Making sense of brain network data. *Nature Publishing Group*, 10(6):491–493, 2013.

[35] A. Haimovici, E. Tagliazucchi, P. Balenzuela, and D.R. Chialvo. Brain organization into resting state networks emerges at criticality on a model of the human connectome. *Physical review letters*, 110(17):178101, 2013.

[36] Mark EJ Newman. The structure and function of complex networks. *SIAM review*, 45(2):167–256, 2003.

[37] Danielle S Bassett and Olaf Sporns. Network neuroscience. *Nature Neuroscience*, 20(3):353 – 364, 2017.

[38] Lav R Varshney, Beth L Chen, Eric Paniagua, David H Hall, and Dmitri B Chklovskii. Structural properties of the caenorhabditis elegans neuronal network. *PLoS Comput Biol*, 7(2):e1001066, 2011.

[39] Denis Le Bihan, Jean-François Mangin, Cyril Poupon, Chris A Clark, Sabina Pappata, Nicolas Molko, and Hughes Chabriat. Diffusion tensor imaging: concepts and applications. *Journal of Magnetic Resonance Imaging: An Official Journal of the International Society for Magnetic Resonance in Medicine*, 13(4):534–546, 2001.

[40] Van J Wedeen, Patric Hagmann, Wen-Yih Isaac Tseng, Timothy G Reese, and Robert M Weisskoff. Mapping complex tissue architecture with diffusion spectrum magnetic resonance imaging. *Magnetic resonance in medicine*, 54(6):1377–1386, 2005.

[41] Hannah Devlin, Stuart Clare, and Irene Tracey. What is FMRI? University of Oxford, Medical Science Division. `https://www.ndcn.ox.ac.uk/divisions/fmrib/what-is-fmri`, 2021.

[42] Karl J Friston, Steven Williams, Robert Howard, Richard SJ Frackowiak, and Robert Turner. Movement-related effects in fmri time-series. *Magnetic resonance in medicine*, 35(3):346–355, 1996.

[43] Karl J Friston. Functional and effective connectivity: a review. *Brain connectivity*, 1(1):13–36, 2011.

[44] Martin J McKeown, Lars Kai Hansen, and Terrence J Sejnowsk. Independent component analysis of functional mri: what is signal and what is noise? *Current Opinion in Neurobiology*, 13(5):620–629, 2003.

[45] Martijn P. van den Heuvel and Hilleke E. Hulshoff Pol. Exploring the brain network: A review on resting-state fmri functional connectivity. *European Neuropsychopharmacology*, 20(8):519–534, 2010.

[46] D. Mantini, M. G. Perrucci, C. Del Gratta, G. L. Romani, and M. Corbetta. Electrophysiological signatures of resting state networks in the human brain. *Proceedings of the National Academy of Sciences*, 104(32):13170–13175, 2007.

[47] Luciano Reatto. A complex view of criticality. *Nature Physics*, 3(9):594–595, 2007.

[48] Sophia Kivelson and Steven A Kivelson. Defining emergence in physics. *npj Quantum Materials*, 1(16024), 2016.

[49] Leo P Kadanoff, Sidney R Nagel, Lei Wu, and Su-min Zhou. Scaling and universality in avalanches. *Physical Review A*, 39(12):6524, 1989.

[50] Marco Baiesi and Maya Paczuski. Scale-free networks of earthquakes and aftershocks. *Physical review E*, 69(6):066106, 2004.

[51] Siegfried Clar, Barbara Drossel, and Franz Schwabl. Forest fires and other examples of self-organized criticality. *Journal of Physics: Condensed Matter*, 8(37):6803–6824, sep 1996.

[52] Serena di Santo, Pablo Villegas, Raffaella Burioni, and Miguel A. Muñoz. Simple unified view of branching process statistics: Random walks in balanced logarithmic potentials. *Phys. Rev. E*, 95:032115, Mar 2017.

[53] Theodore E. Harris. *The theory of branching processes.* New York, Dover, 1989.

[54] Matteo Martinello, Jorge Hidalgo, Amos Maritan, Serena di Santo, Dietmar Plenz, and Miguel A. Muñoz. Neutral theory and scale-free neural dynamics. *Phys. Rev. X*, 7:041071, Dec 2017.

[55] Klaus Linkenkaer-Hansen, Vadim V. Nikouline, J. Matias Palva, and Risto J. Ilmoniemi. Long-range temporal correlations and scaling behavior in human brain oscillations. *Journal of Neuroscience*, 21(4):1370–1377, 2001.

[56] Craig D. Lewis, Gerard L. Gebber, Peter D. Larsen, and Susan M. Barman. Long-term correlations in the spike trains of medullary sympathetic neurons. *Journal of Neurophysiology*, 85(4):1614–1622, 2001.

[57] Steven B Lowen, Sydney S Cash, Mu-ming Poo, and Malvin C Teich. Quantal neurotransmitter secretion rate exhibits fractal behavior. *Journal of neuroscience*, 17(15):5666–5677, 1997.

[58] Christian Meisel, Kimberlyn Bailey, Peter Achermann, and Dietmar Plenz. Decline of long-range temporal correlations in the human brain during sustained wakefulness. *Scientific Reports*, 7(11825), 2017.

[59] Daniel Fraiman, Pablo Balenzuela, Jennifer Foss, and Dante R Chialvo. Ising-like dynamics in large-scale functional brain networks. *Physical Review E*, 79(6):061922, 2009.

[60] Manfred G. Kitzbichler, Marie L. Smith, Søren R. Christensen, and Ed Bullmore. Broadband criticality of human brain network synchronization. *PLOS Computational Biology*, 5(3):1–13, 03 2009.

[61] Michel Hofman. Evolution of the human brain: when bigger is better. *Frontiers in Neuroanatomy*, 8:15, 2014.

[62] Giulio Tononi. Consciousness as integrated information: a provisional manifesto. *The Biological Bulletin*, 215(3):216–242, 2008.

[63] James P. Sethna. *Statistical Mechanics: Entropy, Order Parameters and Complexity.* Oxford University Press, Great Clarendon Street, Oxford OX2 6DP, first edition edition, 2006.

[64] Glenn N. Saxe, Daniel Calderone, and Leah J. Morales. Brain entropy and human intelligence: A resting-state fmri study. *PLOS ONE*, 13(2):1–21, 02 2018.

[65] Alanna Watt and Niraj Desai. Homeostatic plasticity and stdp: keeping a neuron's cool in a fluctuating world. *Frontiers in Synaptic Neuroscience*, 2:5, 2010.

[66] Dominique Fernandes and Ana Luísa Carvalho. Mechanisms of homeostatic plasticity in the excitatory synapse. *Journal of neurochemistry*, 139(6):973–996, 2016.

[67] Daniel Kaplan and Leon Glass. *Understanding Nonlinear Dynamics.* Texts in Applied Mathematics 19. Springer-Verlag New York, 1 edition, 1995.

[68] Rodrigo P. Rocha, Loren Koçillari, Samir Suweis, Maurizio Corbetta, and Amos Maritan. Homeostatic plasticity and emergence of functional networks in a whole-brain model at criticality. *Scientific Reports*, 8(15682), 2018.

[69] J.M. Greenberg and S.P. Hastings. Spatial Patterns for Discrete Models of Diffusion in Excitable Media. *SIAM Journal on Applied Mathematics*, 34(3):515–523, 1978.

[70] Ariel Haimovici. *Hacia una mecanica estadistica de los estados cerebrales macroscopicos.* PhD thesis, Universidad de Buenos Aires, 2017.

[71] Dietrich Stauffer; Amnon Aharony. *Introduction to percolation theory.* Taylor Francis, 2nd ed edition, 1992.

[72] A. Margolina, H.J. Herrmann, and D. Stauffer. Size of largest and second largest cluster in random percolation. *Physics Letters A*, 93(2):73–75, 1982.

[73] Karl J Friston, Andrea Mechelli, Robert Turner, and Cathy J Price. Nonlinear responses in fmri: the balloon model, volterra kernels, and other hemodynamics. *NeuroImage*, 12(4):466–477, 2000.

[74] Andrew Jahn. *Andy's Brain Book.* University of Michigan, 2019.

[75] J.D. Rudie, J.A. Brown, D. Beck-Pancer, L.M. Hernandez, E.L. Dennis, P.M. Thompson, S.Y. Bookheimer, and M. Dapretto. Altered functional and structural brain network organization in autism. *NeuroImage: Clinical*, 2:79–94, 2013.

[76] Leonardo Dalla Porta and Mauro Copelli. Modeling neuronal avalanches and long-range temporal correlations at the emergence of collective oscillations: Continuously varying exponents mimic m/eeg results. *PLOS Computational Biology*, 15(4):1–26, 04 2019.

[77] Matteo Martinello, Jorge Hidalgo, Amos Maritan, Serena di Santo, Dietmar Plenz, and Miguel A. Muñoz. Neutral theory and scale-free neural dynamics. *Phys. Rev. X*, 7:041071, Dec 2017.

[78] Mahdi Zarepour, Juan I. Perotti, Orlando V. Billoni, Dante R. Chialvo, and Sergio A. Cannas. Universal and nonuniversal neural dynamics on small world connectomes: A finite-size scaling analysis. *Phys. Rev. E*, 100:052138, Nov 2019.

[79] G Tononi, O Sporns, and G M Edelman. A measure for brain complexity: relating functional segregation and integration in the nervous system. *Proceedings of the National Academy of Sciences*, 91(11):5033–5037, 1994.

[80] Miguel A Munoz. Colloquium: Criticality and dynamical scaling in living systems. *Reviews of Modern Physics*, 90(3):031001, 2018.

[81] Rodrigo P. Rocha, Loren Koçillari, Samir Suweis, Michele De Filippo De Grazia, Michel Thiebaut de Schotten, Marco Zorzi, and Maurizio Corbetta. Recovery of neural dynamics criticality in personalized whole brain models of stroke. *bioRxiv*, 2020.

[82] Sergio Gómez, Jesús Gómez-Gardeñes, Yamir Moreno, and Alex Arenas. Nonperturbative heterogeneous mean-field approach to epidemic spreading in complex networks. *Phys. Rev. E*, 84:036105, Sep 2011.

[83] Alan J McKane and Timothy J Newman. Predator-prey cycles from resonant amplification of demographic stochasticity. *Physical review letters*, 94(21):218102, 2005.

[84] M. Newman. *Networks: An Introduction*. OUP Oxford, 2010.

[85] Duncan J Watts and Steven H Strogatz. Collective dynamics of 'small-world'networks. *nature*, 393(6684):440–442, 1998.

[86] Albert-László Barabási and Réka Albert. Emergence of scaling in random networks. *science*, 286(5439):509–512, 1999.

[87] M Chaichian and A Demichev. *Path Integrals in Physics: Volume I Stochastic Processes and Quantum Mechanics*. Institute of Physics Publishing, 2001.

[88] Hiroki Sayama. Linear Stability Analysis of Nonlinear Dynamical Systems, 2020.